Stress-driven melt redistribution in partially molten rocks deformed in torsion: from pressure shadows to base-state segregation

A THESIS

SUBMITTED TO THE FACULTY OF THE GRADUATE SCHOOL

OF THE UNIVERSITY OF MINNESOTA

BY

Chao Qi

IN PARTIAL FULFILLMENT OF THE REQUIREMENTS

FOR THE DEGREE OF

DOCTOR OF PHILOSOPHY

David L. Kohlstedt

October, 2014

Acknowledgements

In the past five years at University of Minnesota, I owe many thanks to my advisor, David Kohlstedt. On my study and research, David is always willing to sacrifice his time for my questions, and providing inspirations, guidance and encouragements. I derived knowledge and wisdom from the communications with David, and established a rigorous scholarship due to his imperceptible influences. David also gave me opportunities to collaborate with other talented scientists from different places of the world, which broadened my vision and extended my relationship to others. Besides research, David showed consideration for my life in Minnesota, which gave me great support to finish my studies in a foreign land. I am so fortunate to be a student of him, who is a great example for me in my pursue of science.

I am very grateful to Mark Zimmerman for his selfless help with my experiments. Mark taught me to use every piece of equipment in the lab and fixed the equipment whenever it broke, which allowed me to finish all these experiments in five years. Mark is the key person that keeps the lab in order, and a database in a human body, which memorises all the tricks and skills that lead us to a successful experiment.

I am thankful to Shenghua Mei for his support in the past five years. Shenghua is like a family who cares me when homesick attacks in the endless white winter of Minnesota.

Lars Hansen helped me in every aspect for countless times during our overlapped years. His assiduousness, optimism and enthusiasm in research have deeply influenced me. Moreover, his precious legacy of “dart-fighting” has flourished in our lab, which brings joy and happiness to generations of lab members.

Part of my work follows the path of Dan Kind's work. His help on the methodology and experimental techniques is appreciated.

Yong-hong Zhao helped me a lot with my experiments and taught me many skills to increase my success rate of experiments. Without her, I would not produce this amount of data in my doctoral study.

I have benefitted from the cooperative atmosphere in the lab, and received a lot of help from fellow graduate students: Amanda Dillman, Yang Li, Jacob Tielke and Cameron Meyers; and from post-docs and visiting researchers: Ayako Suzuki, Marshall Sundberg, Takehiro Hiraga, Lili Xu, Miki Tasaka, Matěj Peč, Janelle Homberg, Junfeng Zhang, Guinan Zhang and Wuming Bai.

I need to thank my collaborators in my research projects: Prof. Richard Katz, Prof. Yasuko Takei, Prof. John Rudge and Dr. Laura Alisic, some of whom offered me valuable chances to visit Oxford University and Cambridge University.

I am also thankful to Ben Holtzman for stimulating discussions, to Marc Hirschmann for valuable advices on the choice of melt composition, to Paul Morin for valuable suggestions on image processing, to Anette von der Handt for help on electron microprobe analyses, to Jessica Warren for allowing me to use her electron backscattered diffraction facility at Stanford University and to Nick Seaton for running the scanning electron microscope at the characterization facility.

I appreciate the guidance and advice provided by all my committee members: David Kohlstedt, Marc Hirschmann, Peter Hudleston, Justin Revenaugh and Martin Saar.

I could not accomplish my doctoral study and research without the support from my family and friends, especially my parents Yixing Qi and Shuling Liu, and my girlfriend Ruchen Zhou. I need to thank my friend and lab mate Yang Li for being supportive in the past five years. Without each other, we would possible die from solitude in the first month in Minnesota.

At last, I want to thank all the organizations that funded me as a doctoral student. I have benefitted from NSF support through grants awarded to David Kohlstedt. Department of Earth Sciences of University of Minnesota has provided generous support in the form of fellowships. They are the Forrest Fellowship, the Richard C. Dennis Graduate Fellowship, the V. Rama Murthy

/ Janice Noruk Fellowship and the Harold Mooney Fellowship. A Doctoral Dissertation Fellowship from the University of Minnesota is greatly acknowledged for funding the final of year of my doctoral research.

Abstract

The redistribution of melt in partially molten rocks during deformation plays an important role in the evolution and dynamics of Earth's mantle. Previous studies discovered different scales of melt redistribution: melt alignment and melt segregation to form melt-enriched bands (e.g. *Zimmerman et al.*, 1999; *Holtzman et al.*, 2003a), both of which have demonstrated their importance to the deformation of the mantle. In this dissertation, two new forms of stress-driven melt redistribution in deformed partially molten rocks are produced: a formation of pressure shadows around rigid particles and a large-scale, base-state melt segregation. For pressure shadows, observations on the microstructure around the rigid particles revealed the melt distribution and solid flow field, which will provide a constraint on the bulk viscosity of the partially molten rock, if associated with theoretical studies. The presence of base-state melt segregation validated a hypothesis of viscous anisotropy, which provides explanations for melt segregation processes and will cause a significant impact to the dynamic of the mantle. Therefore, the studies of stress-driven melt redistribution in this dissertation are of great significance that will influence the future studies of Earth's mantle.

Contents

List of Tables

List of Figures

Chapter 1

Introduction

1.1 Background

The response of melt to deformation in partially molten rocks plays an important role in the dynamics of Earth's mantle. Although the origins of the lithosphere-asthenosphere boundary is under debate (*Fischer et al.*, 2010), a small amount of melt, which significantly reduces mantle viscosity (e.g., *Hirth and Kohlstedt*, 1995a,b; *Mei et al.*, 2002), could contribute to the formation of a mechanically weak layer, since studies have suggested that the asthenosphere contains a small amount of partial melt (*Anderson and Sammis*, 1970; *Hirano et al.*, 2006; *Mierdel et al.*, 2007). At mid-ocean ridges (MOR), the largest volcanic system on Earth, oceanic crust is created within a narrow neovolcanic zone due to the uprising of melt. Models have indicated that melt from a wide, low melt-percentage, partially molten zone is focused to a narrow region beneath the ridge axis (e.g., *Morgan*, 1987; *Kelemen et al.*, 1995). Beneath subduction zones, melt is generated in the"hot corner" of the mantle wedge and ascends across a region of lateral or even descending mantle flow to feed arc volcanos, which is a process involving melt extraction and migration (*Stern*, 2002). Early experimental studies focused on the rheology of partially molten mantle rocks, that is, the dependence of viscosity on the melt phase (e.g., *Cooper and Kohlstedt*, 1984; *Kohlstedt et al.*, 1996). Later on, experimental investigations emphasized the influence of deformation on

the distribution of melt. Firstly, induced by shear stress, the coherent alignment of melt at grain scale was discovered in direct shear experiments of olivine + basalt aggregates (*Zimmerman et al.*, 1999). Secondly, a stress-driven melt segregation that forms melt-enriched sheets (bands in cross section) was discovered and explored in both direct shear and torsion experiments (*Holtzman et al.*, 2003a,b; *King et al.*, 2010; *Kohlstedt et al.*, 2010). With the alignment of melt and the formation of melt-enriched bands well studied in experiments, the work presented here focuses on innovative experiments to investigate the stress-driven redistribution of melt, to constrain and understand parameters that affect the behavior of melt during deformation.

The behavior of melt during deformation, including melt segregation and extraction, is elaborated by two-phase flow theory as a compaction/decompaction process (*McKenzie*, 1984; *Stevenson*, 1989). Compaction length, δ_c, a term which depends only on the properties of the material, plays a crucial role in the compaction process. δ_c is defined as

$$\delta_c = \left[\frac{(\zeta + \frac{4}{3}\eta)k}{\mu}\right]^{1/2}, \tag{1.1}$$

where ζ and η are the bulk and shear viscosities of the matrix, μ is the viscosity of the melt and k is the permeability of the matrix. In order to better understand compaction length and compaction processes, in this dissertation, we present two types of stress-driven melt redistributions: (1) pressure shadows formed around rigid particles in partially molten rocks under shear deformation, and (2) base-state melt segregation caused by a large-scale pressure gradient induced by the alignment of melt. We examined the development of pressure shadows around single crystal beads of olivine in olivine + basalt aggregates during torsional deformation, which is a process controlled by the ratio ζ/η (Chapter 2). We tested and investigated the hypothesis of viscous anisotropy by producing base-state melt segregation during torsional deformation, whose compaction rate is strongly influenced by the compaction length (Chapters 3 and 4).

1.2 Design of torsion experiments

All experiments in this dissertation were performed in a gas-medium, high-temperature and high-pressure deformation apparatus equipped with a torsion actuator (*Paterson and Olgaard*, 2000). The common working conditions for this apparatus are a temperature of 1473 K and confining pressure of 300 MPa, while at extreme conditions, temperature was increased to 1573 K and confining pressure to 400 MPa. The gas medium used in this apparatus is Ar, which provides an inert environment for the sample assembly. The confining pressure from the gas medium is controlled within $\pm$2 MPa in the experiment. Due to the convection of the gas medium, at 1473 K and 300 MPa, a hot-zone with a temperature variance of $\pm$1 K is maintained to extend at least 35 mm, which provides a temperature gradient of $<$0.1 K/mm along the sample. With this precision control of temperature, we are able to deform samples as long as 30 mm. Torque is measured using an internal torque cell with a resolution of 0.2 N·m, and angular displacement is measured with an external rotational variable differential transducer with a resolution of 0.001 rad. Theoretically, samples can be deformed to unlimited strains; while practically, an outer-radius shear strain of $\gamma \gtrsim 5$ is common and $\gamma \gtrsim 10$ is achievable. Thus, this apparatus allows us to explore a wide range of parameter space in one experiment.

The design of sample assembly for torsion experiments is illustrated in Figure 1.1. The assembly is generally 15 mm in diameter and 185$\pm$5 mm in height (between top and bottom ZrO_2 pistons). At the middle part of the assembly, sample (or cold-pressed powder in the case of hot-pressing and torsion combined in one run) is placed in a Ni can with a inner diameter of 13.5 mm. Within this Ni can, dunite spacers are placed next to the sample, and porous Al_2O_3 spacers sit beside dunite spacers, which is like a "sandwich" (photo in Figure 1.1). Away from sample, Al_2O_3 and ZrO_2 pistons are placed sequently. Each of the top ZrO_2 and Al_2O_3 pistons has a hole of 2 mm in diameter in the center, which allows the thermo-couple to come through these pistons and to directly measure the temperature in the hot zone. The whole assembly is then jacketed in an iron tube, with geared deformation pistons on top and bottom (not included in Figure 1.1). The iron tube isolates the sample and pistons from the Ar gas, such that, at high pressure sample and

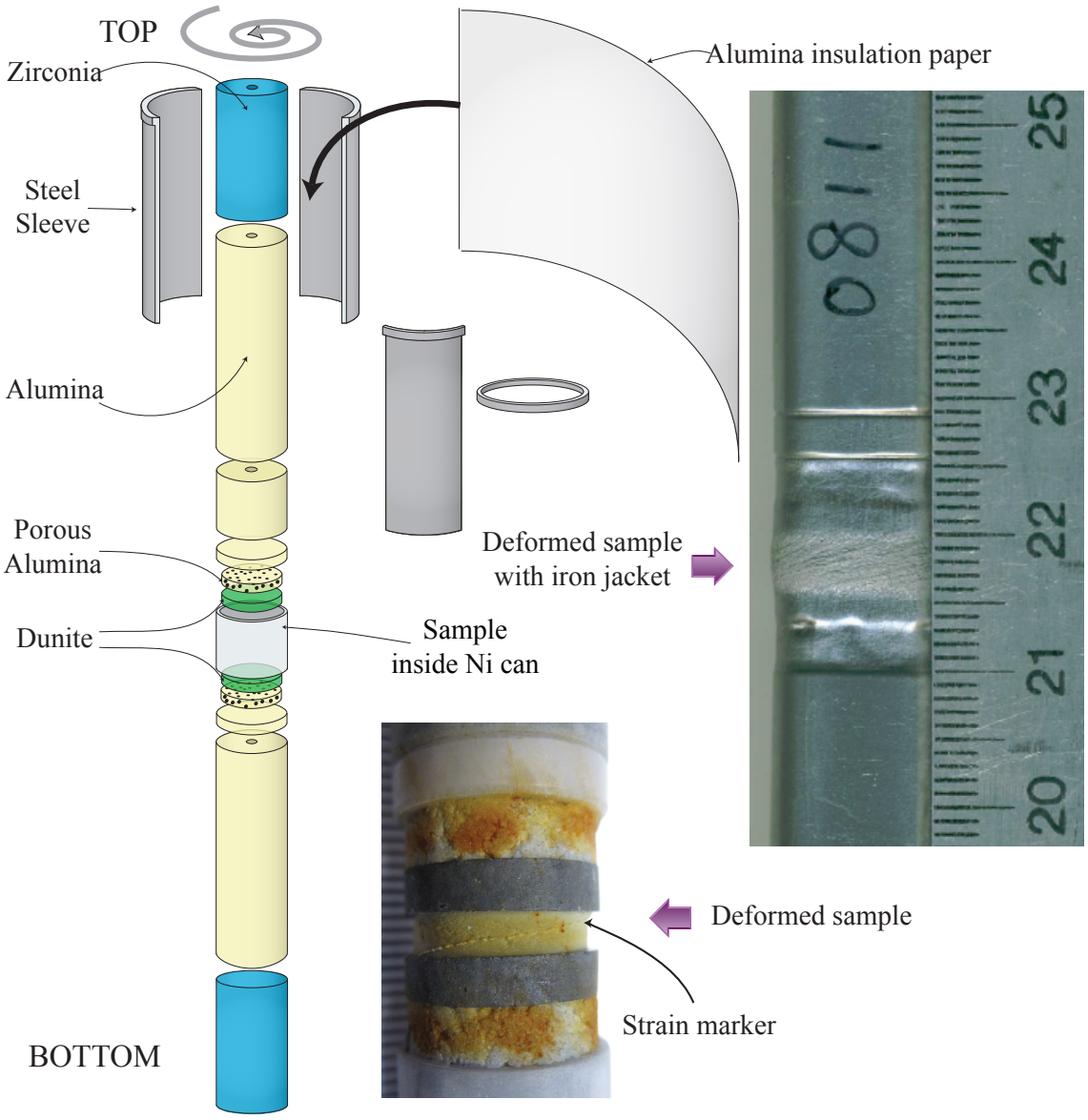

Figure 1.1: Drawing of torsion assembly. All pistons are enclosed in an iron tube, which is not shown in the figure. The drawing is not to scale. Photos for a deformed sample with and without the iron jacket are shown. Photo for the deformed sample without iron jacket reveals the "sandwich" design: sample is green, dunite spacer is dark grey, and porous Al_2O_3 is white with yellow stains from acid, used for dissolving the iron tube and Ni can. This drawing is modified from Justin Hustoft's dissertation.

pistons are held together tightly without slip between any boundaries. The top part of the iron tube is wrapped with Al_2O_3 paper, which is held by three stainless steel sleeves for insulation. Then, the jacketed assembly is loaded into the apparatus for the experiment.

1.3 Outline of work presented here

Chapter 2 is a paper that was published in 2013 on *Earth and Planetary Science Letters*. This chapter presents torsion experiments on partially molten rocks containing dispersed sub-millimeter-sized, single crystal beads of olivine, designed to study the development of melt-enriched pressure shadows induced by the pressure gradient around the olivine beads.

Chapter 3 is modified from a paper that will be submitted to *Science* co-authored with Richard Katz and Yasuko Takei. The purpose of this chapter is to test the hypothesis of viscous anisotropy, which predicts a decrease in melt fraction with increasing distance from the axial center in a cylindrical, partially molten rock deformed under torsion.

Chapter 4 is a study built upon the result of Chapter 3. With the hypothesis of viscous anisotropy tested, the compaction rate for base-state melt segregation in torsional deformation is explored experimentally. A series of torsion experiments on partially molten rocks fabricated from olivine + melts of three different compositions were performed to vary the compaction length, which is a length scale that only depends on the properties of the materials (including solid and melt) and that strongly influences the compaction process.

Chapter 5 presents a summary of results and a prospect of future directions to pursue based on the results of this work.

Chapter 2

Formation of Pressure Shadows in Partially Molten Rocks

This chapter has been published in *Earth and Planetary Science Letters*, vol. 382, page 77–84 (2013) with co-authors Yong-Hong Zhao and David L. Kohlstedt and is modified and used in this dissertation with permission from Elsevier.

As a two-phase, solid-melt material flows around rigid particles, melt-depleted and melt-enriched regions (i.e., pressure shadows) develop due to the coupled fluxes of melt and solid driven by pressure gradients around the particles. To study this compaction-decompaction process, samples composed of fine-grained San Carlos olivine plus mid-ocean ridge basalt containing dispersed sub-millimeter-sized, single crystal beads of olivine were deformed in torsion at a temperature of 1473 K and a confining pressure of 300 MPa. Indicated by melt distribution maps obtained from reflected-light optical and backscattered electron microscopy, melt-enriched and melt-depleted regions around the beads became observable at a local shear strain of $\gamma \approx 1$ in samples with an initially homogeneously distributed melt fraction of $\phi \approx 0.05$. The melt-enriched regions ($\bar{\phi}_{high} \approx$ 0.06 to 0.10) and the melt-depleted regions ($\bar{\phi}_{low} \approx 0.02$ to 0.04), extending as far as one radius of the bead, were symmetrically distributed around the bead. The flow field of the olivine matrix determined from crystallographic preferred orientations agrees with theoretical predictions based

on two-phase flow analysis. These experiments are the first to produce pressure shadows in partially molten rocks. One implication of this study is that it will be possible to constrain the ratio of bulk to shear viscosity, which is inferred from the distribution of melt using a combination of experimental observations and numerical simulations.

2.1 Introduction

Pressure shadows with two regions filled with a low-viscosity phase located around a large single crystal or hard inclusion are widely observed in metamorphic and igneous rocks. Because the single crystal or hard inclusion is more viscous than the grains in the surrounding matrix due to differences in grain size and/or mineralogy, pressure gradients form around them during deformation, which drive the low-viscosity phase to produce pressure shadows. Fibrous growths in pressure shadows have been used to track the deformation history of rocks (e.g., *Elliott*, 1972; *Durney and Ramsay*, 1973; *Ramsay and Huber*, 1983; *Spencer*, 1991). One explanation for the development of pressure shadows holds that growth takes place continuously by stress-induced solution transfer (*Vernon*, 2004). Besides fibrous solid-phase pressure shadows, melt-phase pressure shadows were also identified from the presence of an augen-shaped, fine-grained olivine + orthopyroxene mixture around a large orthopyroxene porphyroclast (*Dijkstra et al.*, 2002).

Several modelling studies have examined the formation of pressure shadows (e.g., *Etchecopar and Malavieille*, 1987; *Fisher and Brantley*, 1992; *Masuda and Mizuno*, 1995; *McKenzie and Holness*, 2000; *Berton et al.*, 2006). *Berton et al.* (2006) were the first to model the growth of fibrous solid-phase pressure shadows in terms of diffusion creep with different diffusion coefficients for interphase boundaries and grain boundaries. They found that the growth rate of fibrous pressure shadows is enhanced by decreasing the inclusion size (*Berton et al.*, 2011) and increasing the ratio of diffusion coefficients between interphase boundaries and grain boundaries. *Masuda and Mizuno* (1995) theoretically simulated the flow field of an incompressible fluid around a rigid sphere under pure shear, which led to the formation of melt-phase pressure shadows. *McKenzie and Holness* (2000) provided analytical solutions for a model of compacting flow around a rigid

stationary sphere using two-phase flow governing equations. These authors calculated matrix velocity and melt flux for pure and simple shear, from which the development of pressure shadows was predicted.

In this study, pressure shadows were produced in torsion experiments on fine-grained samples of olivine + basalt containing a few larger, spherical crystals of olivine. The melt distribution around a sphere was mapped in a tangential section by optical reflected-light or backscattered electron (BSE) microscopy. The orientation of stress field in the matrix was inferred from crystallographic preferred orientations (CPOs) obtained using electron backscattered diffraction (EBSD). The observations from the experiments were used as a test of the applicability of the theory by *McKenzie and Holness* (2000). In their theory, the properties of the deforming rock that control the development of pressure shadows, such as melt flux and matrix velocity, are simplified into the ratio of bulk to shear viscosity. In this chapter, we present the results from the first set of samples deformed to different finite strain and make a qualitative comparison of our observations with the theory.

2.2 Methods

2.2.1 Sample preparation and deformation assembly

Samples were fabricated from mixtures of fine-grained powders of olivine from San Carlos, AZ, plus 10 vol.% mid-ocean ridge basalt (MORB) from the Mid-Atlantic Ridge with an olivine tholeiite composition (*Cooper and Kohlstedt*, 1984). Olivine powders were obtained by grinding San Carlos olivine crystals in a fluid-energy mill to produce a particle size of 2 μm. Before mechanically mixing with MORB powders with a particle size of 8 μm, the olivine powders were dried at 1373 K for 10 h at an fO_2 near the Ni-NiO buffer to remove water and carbon-based impurities introduced during the grinding process.

Mixtures were then uniaxially cold-pressed into nickel capsules with dispersed sub-millimeter

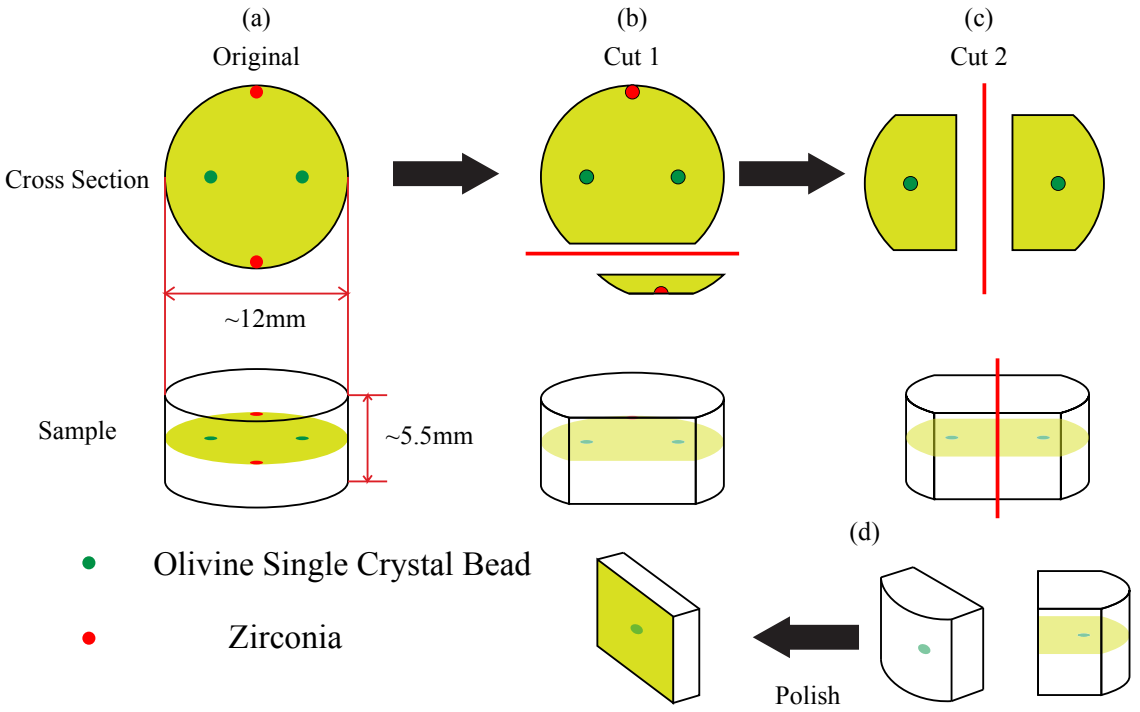

Figure 2.1: Sample design. (a) The beads are located in a horizontal layer in the pattern shown. (b) A piece of sample containing a zirconia bead is cut off (as cut 1). The cutting surface is perpendicular to the cord of the two zirconia beads. (c) The rest of the sample is cut into two pieces at the center of the sample normal to the surface of cut 1 (as cut 2). (d) A tangential section is polished to the center of an olivine bead.

beads of MgO-stabilized zirconia and San Carlos olivine in one horizontal layer with the distribution of beads illustrated in Figure 2.1(a). The relative positions of the beads did not change during torsional deformation. The beads on the outer edge of the sample were used as markers to locate the beads at half radius. A vertical groove made on the inner surface of each nickel capsule was used to produce a strain marker on the outer surface of the sample. To prevent slipping along the sample-spacer boundaries during torsional deformation, spacers cored from a coarse-grained natural dunite were cold-pressed with the powders as end caps of the nickel capsules, thus providing non-reactive, impermeable boundaries. The sample, Al_2O_3 spacers and pistons, and ZrO_2 pistons were enclosed in an iron jacket as described in *Paterson and Olgaard* (2000).

Samples were then hydrostatically hot-pressed in a gas-medium apparatus at 1473 K and 300 MPa for 3 h to densify the cold-pressed powders and mechanically and chemically bond the sample to dunite spacers. After hot-pressing, samples were $\sim$12 mm in diameter and 5 to 10 mm in height with an olivine grain size of $\sim$10 μm.

2.2.2 Experiments

Immediately after hot-pressing, samples were deformed in torsion at a confining pressure, P, of 300 MPa and a temperature, T, of 1473 K in a gas-medium deformation apparatus equipped with a torsion actuator (*Paterson and Olgaard*, 2000). Pressure and temperature were maintained constant to $\pm$2 MPa and $\pm$1 K, respectively, with temperature gradients along the sample of $<$0.1 K/mm. Torque was measured with an internal torque cell with a resolution of 0.2 N·m, and angular displacement was measured with an external rotational variable differential transformer with a resolution of 0.001 rad (*Kohlstedt et al.*, 2010).

Experiments were designed to develop stress-induced melt distributions around the beads in a series of samples deformed at approximately the same strain rate to different finite strains. Samples were deformed at constant twist rates, yielding a constant outer-radius shear strain rate of $\dot{\gamma} \approx 1\times10^{-4}$ s^{-1}, to outer-radius shear strains of $1.7 \leq \gamma \leq 10.0$. After achieving the target strain, each sample was cooled rapidly ($\sim$2 K/s) to 1300 K under the same torque as imposed at the end of the

deformation experiment to preserve the deformation-produced microstructure and then cooled to room temperature with no torque applied.

After deformation, the iron jacket and the nickel capsule were dissolved with acid, revealing the strain marker on the outer surface of the sample. The shear strain of a sample was determined precisely by measuring the angle of this strain marker relative to shear direction.

2.2.3 Microstructure and image analysis

With the iron jacket and nickel capsule dissolved, the marker beads were revealed at the outer surface of the sample. Each sample was cut into pieces as illustrated in Figure **??**, with each piece containing one bead, according to the location map of the beads. A tangential section, which is the best section to observe pressure shadows, was polished approximately to the center of each bead on a series of diamond lapping films down to 0.5 μm, followed by a final step using colloidal silica. Samples were then examined using BSE microscopy after carbon-coating to prevent charging, as well as by reflected light optical microscopy after chemically etching with diluted HF to highlight melt pockets.

A set of BSE or optical reflected-light microscopic images taken to cover the area around each bead in the tangential section were stitched together. The stitched image was processed in MATLAB with a Gaussian filter to reduce noise. A binary image was then created with melt appearing white by using an edge detection method (*Canny*, 1986; *Lim*, 1990; *Parker*, 2010). This binary image was divided into grids with a representative area (50μm $\times$ 50μm) small enough to define a point property at the macroscopic scale but large enough to contain many melt pockets at the microscopic scale. The fraction of white area (melt) was calculated for each representative area. Next, the melt fraction of each grid was plotted on a pseudo-color map to illustrate the melt distribution around the bead in order to highlight melt-enriched and melt-depleted regions.

The distribution of crystallographic preferred orientations in one sample was characterized with EBSD. A series of EBSD maps were taken and stitched into one large map. Raw orientation data were processed by HKL channel 5 software, while pole figures and orientation maps were

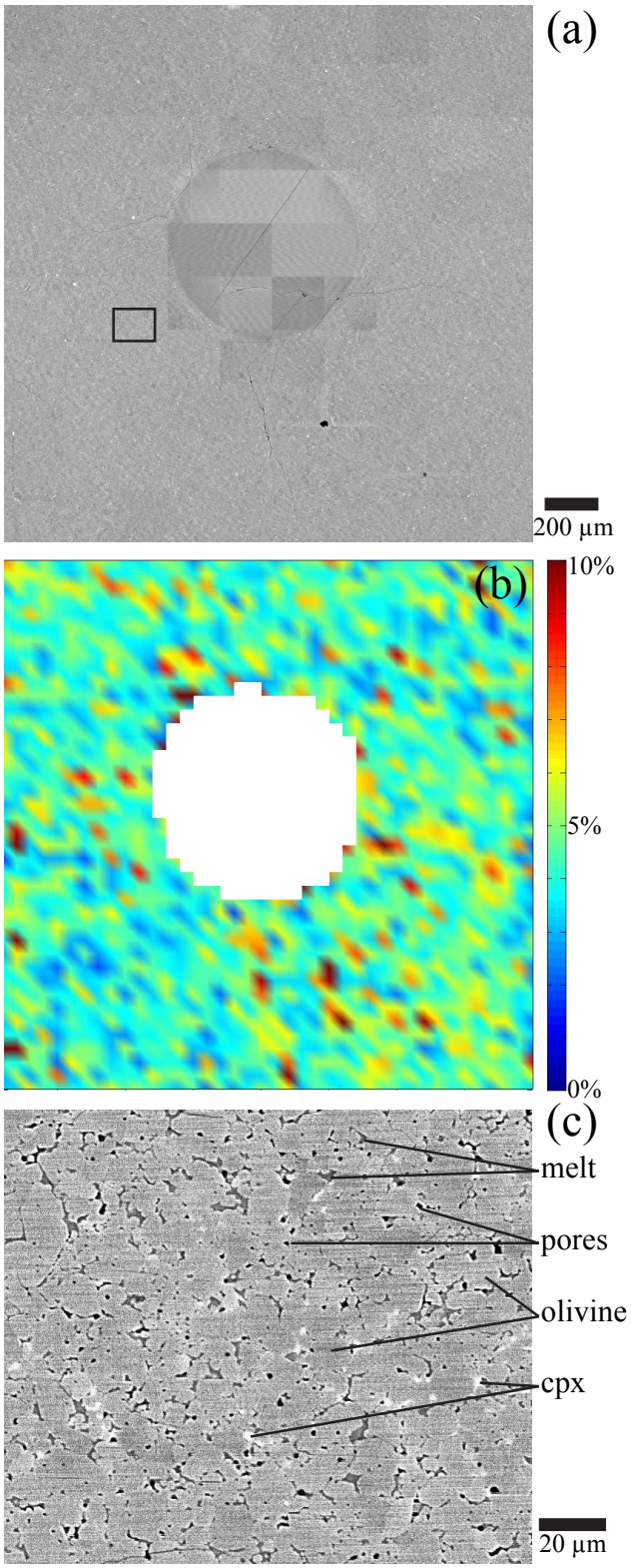

Figure 2.2: Image analysis of a hot-pressed sample. This tangential section is at the center of an olivine single crystal bead. (a) BSE image. (b) Melt distribution color map with a resolution of 50×50 μm per data point. The color bar illustrates percentage of melt. (c) Enlargement of the region outlined in (a). Olivine is light gray, cpx is white, melt pockets are dark gray, and pores (air-filled voids) are black.

generated by mtex toolbox in MATLAB (*Bachmann et al.*, 2010).

2.3 Results

2.3.1 Starting materials

Characteristic features of the microstructure of a hot-pressed sample are illustrated in Figure 2.2. A stitched BSE image is presented in Figure 2.2(a) with the associated melt distribution color map in (b). During the 3-h hot-pressing, olivine grains grew from an initial particle size of 2 μm to a final mean grain size of $\sim$15 μm. By image analysis, the area fraction of melt, $\phi \approx 0.05$, in the starting material is lower than the volume fraction (0.10) of MORB powder added, due to precipitation of clinopyroxene (cpx) from the melt during the experiments. Thus, our measured melt fraction represents the area fraction of melt at the end of an experiment.

Based on Figure 2.2, olivine and basaltic glass (quenched melt) are largely homogeneously and isotropically distributed in the hot-pressed sample. In Figure 2.2(b), except for small local variations in melt fraction, we conclude that the melt distribution is homogeneous around the olivine single crystal bead. As illustrated in Figure 2.2(c), melt pockets are observable through out the sample with sizes varying from $<$1 μm to as large as 10 μm. Most melt pockets are located at triple junctions and grain boundaries of olivine, with no melt-preferred-orientation (MPO) observed. Therefore, microstructural features such as melt segregation and MPO are not produced during hot-pressing. Our assumption that the textures we discuss in this paper are developed during deformation is well grounded.

2.3.2 Imaging accuracy

In this subsection, we test the accuracy of the imaging technique by comparing hand-traced melt maps with software-identified ones. At our experimental condition of 1473 K and 300 MPa, MORB is undersaturated with olivine. To reach a chemical equilibrium, cpx precipitated as a third phase.

As illustrated in Figure 2.1(c), olivine is light gray, melt is dark grey, cpx is white and pores (air-filled voids) are black in BSE images. Because of the high contrast, boundaries between cpx and olivine in BSE images were also recognized by our edge detection method. Therefore, images were pre-filtered by the difference in gray scale to remove cpx, so that only residual MORB was counted as the melt phase.

To test the robustness of our imaging technique, images of hand-traced and software-identified melt were compared, as presented in Figure 2.3. None of the pores were counted as melt in the computer processed image, although some pores left a ring of white pixels (yellow arrows). A small fraction of the cpx grains were still included as melt (red arrows). However, the image processing technique picked out all of the melt pockets, even tiny ones (blue arrows) that are difficult for human eyes, which was our high priority task. Considering the consistency of image processing between different samples, we trust the results of this image processing technique.

2.3.3 Melt distribution observations

Here, detailed observations of tangential sections of deformed samples are presented. Data include images highlighting the melt distribution across the imaged area as well as the size of and melt fraction in melt-enriched and melt-depleted regions. Experimental conditions are summarized in Table 2.1. Results of image analyses of the melt distribution around beads are summarized in Table 2.2. The local shear strain, γ_{local}, and local shear strain rate, $\dot{\gamma}_{local}$, at each bead were determined as a ratio of the shear strain and the shear strain rate at the outer radius from the radial position of the bead. Melt fractions were calculated by the image processing technique described in section 2.2.3.

Melt-enriched bands were observed in two samples (PI0609 and PI0665). The bands are oriented $\sim$20° to the shear plane, antithetic to the shear direction, similar to those described by *Holtzman and Kohlstedt* (2007). Melt fraction is $\sim$0.10 in the bands, with a background of 0.05 across the entire image. As in Figure 2.4, cpx grains are abundant in the bands due to the equilibration between molten MORB and olivine.

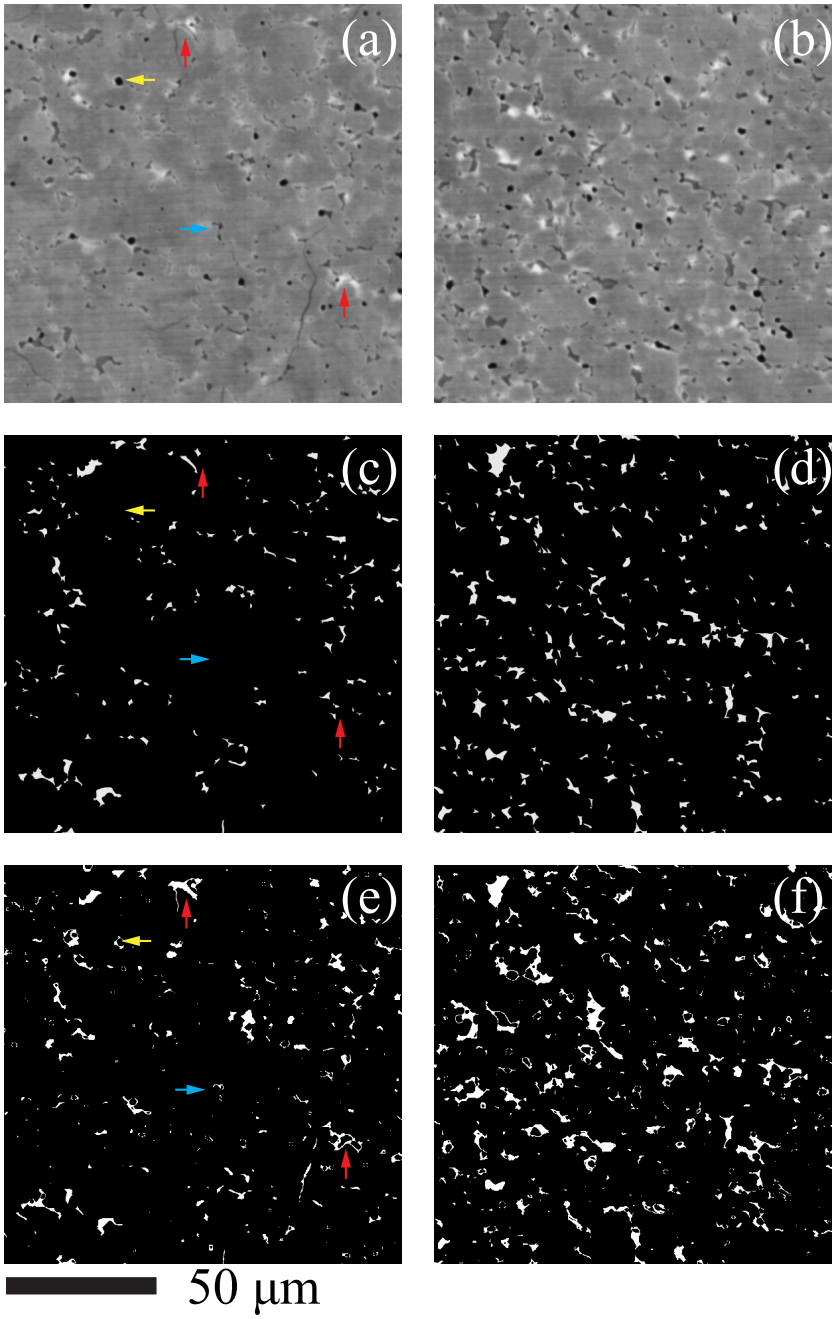

Figure 2.3: Comparison of original BSE image with binary images of hand-traced melt and software-identified melt for sample PI0665. (a), (c) and (e) are from a melt-depleted region, while (b), (d) and (f) are from a melt-enriched region. (a) and (b) are original BSE images. (c) and (d) are binary images of hand-traced melt. (e) and (f) are binary images processed by our melt-identification technique. The comparisons between (c) and (e) are highlighted by a series of arrows: the left-pointing yellow arrow marks at a pore; the right-pointing blue arrow locates a melt pocket; and the two upward-pointing red arrows highlight melt surrounded by cpx.

Table 2.1: Experiment conditions.

Experiment #	σ_{eq} (MPa)	γ	$\dot{\gamma}$ (10^{-4}s^{-1})
PI0564	188	1.5±0.1	0.75±0.05
PI0609	160	10.5±0.5	1.28±0.07
PI0665	100	4.2±0.2	1.19±0.06

Note: σ_{eq} is equivalent stress. γ and $\dot{\gamma}$ are shear strain rate and shear strain, respectively at the outer edge of the sample.

Table 2.2: Conditions of olivine beads

Experiment #	$2a$ (mm)	γ_{local}	$\dot{\gamma}_{local}$ (10^{-4}s^{-1})	$\bar{\phi}\times100$	$\bar{\phi}_{high}\times100$	$\bar{\phi}_{low}\times100$
PI0564	1.2	0.9±0.1	0.45±0.05	6.6	9.8±2.8	3.7±0.9
PI0609	0.7	5.0±0.5	0.78±0.08	5.5	7.4±1.7	3.6±1.1
PI0665	0.7	2.1±0.2	0.60±0.06	4.7	6.3±1.2	2.7±0.8

Note: a is radius of the bead. γ_{local} and $\dot{\gamma}_{local}$ are local shear strain and strain rate at the tangential section we examined. $\bar{\phi}$ is average melt fraction throughout the image taken around the bead. $\bar{\phi}_{high}$ and $\bar{\phi}_{low}$ are average melt fractions of melt-enriched and melt-depleted regions, respectively.

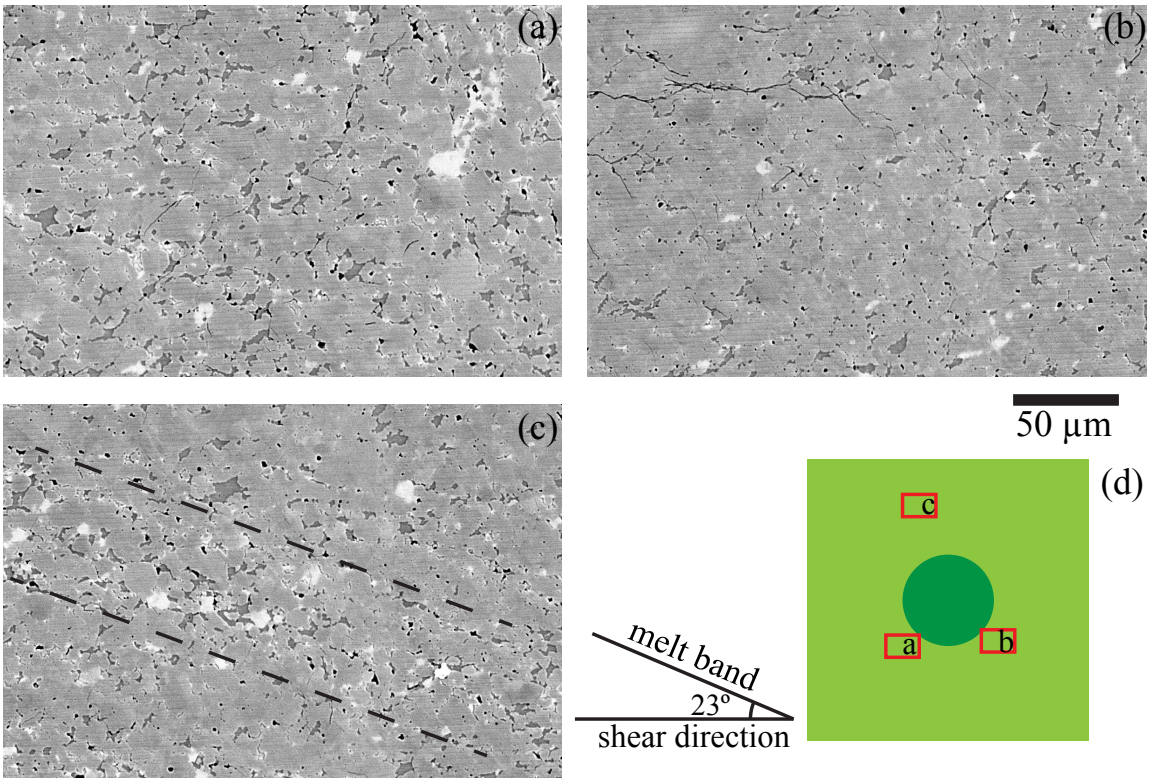

Figure 2.4: BSE images of sample PI0609. (a) A melt-enriched region. (b) A melt-depleted region. (c) A section of a melt-enriched band. The band angle is ∼23° antithetic to shear direction. (d) Sketch of the relative positions of images in (a), (b) and (c).

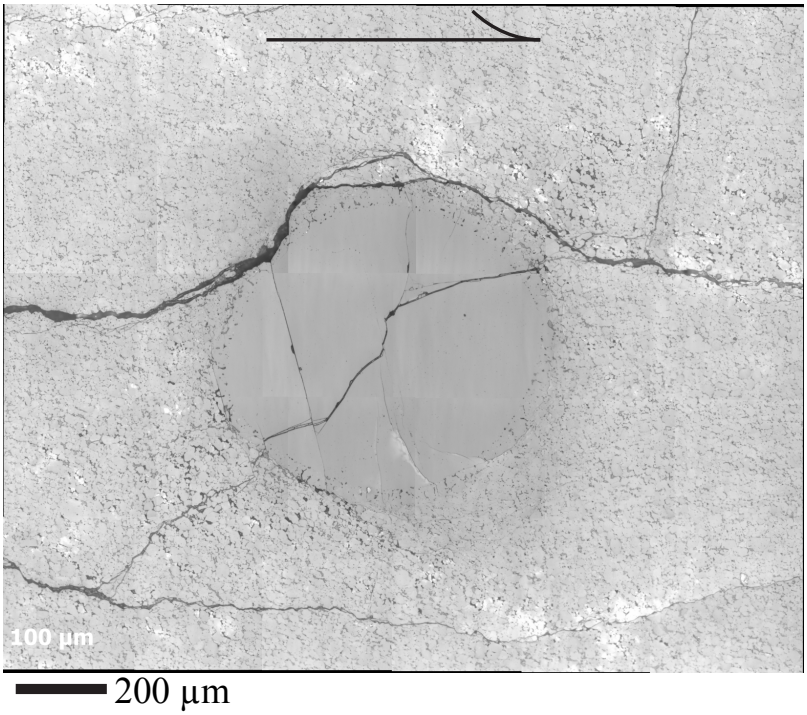

Figure 2.5: Reflected-light optical micrograph. This tangential section is at the center of an olivine single crystal bead located at a local shear strain of $\gamma_{local} \approx 0.9$. The sense of shear is top to the right. Olivine grains are light gray, while melt pockets are dark gray or black. Cracks formed during cooling and depressurizing.

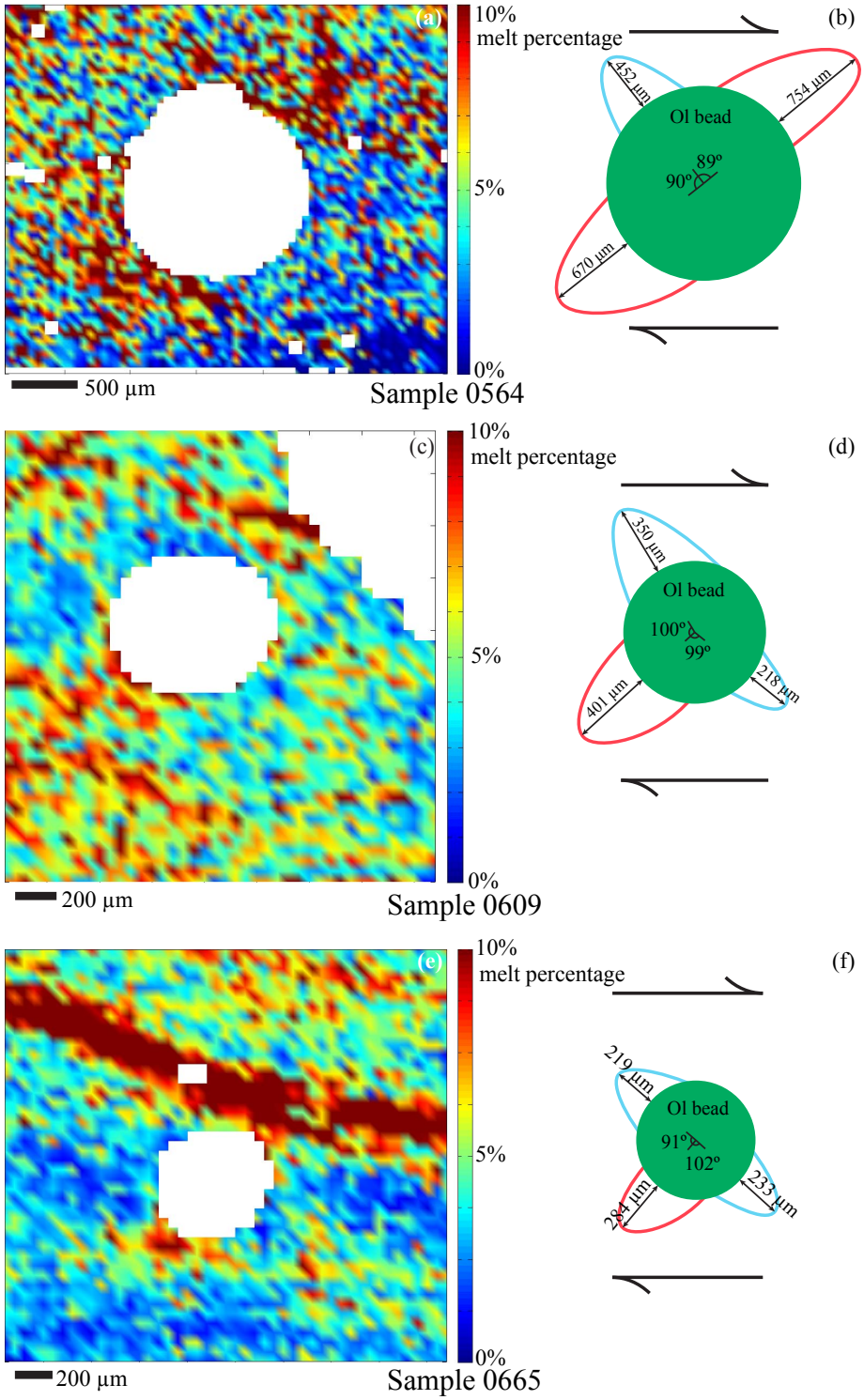

Figure 2.6: Melt distribution maps and sketches for samples PI0564, PI0609 and PI0665. The melt distribution color maps in (a), (c) and (e) have a resolution of 50×50 μm per data point. The color bar illustrates percentage of melt. The large, white circle in the center of each map is the olivine bead. The missing top-right part of the map in (c) is due to the damage of this sample during imaging. Melt-enriched and melt-depleted regions around the bead are illustrated in sketches (b), (d) and (f), respectively.

Three aspects of the melt distribution were recorded — location, shape, and concentration of melt in the melt-enriched and melt-depleted regions. As illustrated by the optical micrograph of a bead in Figure 2.5, the melt distribution around the bead is heterogeneous. Melt distribution color maps for three samples in Figure 2.6 reveal the pressure shadows around the beads. In these samples, melt-enriched regions are oriented approximately northeast-southwest relative to the beads, with melt-depleted regions approximately northwest-southeast. However, two melt-enriched and two melt-depleted regions are not observed in every sample; thus, not all of the four regions are outlined in the figures. The melt-enriched and melt-depleted regions are triangular or half-elliptical extending as far as about one radius (a in Table 2.2) away from the bead, which is 754 μm in sample PI0564, 401 μm in sample PI0609, and 284 μm in sample PI0665. The line connecting the center of a melt-enriched or melt-depleted region and the center of the bead (which is referred to as a connecting line of this region) is oriented 40° to 50° to the shear plane. The locations of melt-enriched and melt-depleted regions are approximately symmetric, as indicated by the angles between the connecting lines (Figure 2.6). The average melt fraction in a melt-enriched or a melt-depleted region is an average of the melt fractions in a grid with an area of 50×50 μm with one standard deviation as the error. The melt fraction in melt-enriched regions, $\bar{\phi}_{high}$, varies from 0.06 to 0.10, while the average melt fraction in melt-depleted regions, $\bar{\phi}_{low}$, lies between 0.02 and 0.04. The ratio of the average melt fraction in a melt-enriched region to that in a melt-depleted region, $\bar{\phi}_{high}/\bar{\phi}_{low}$, varies from 2.1 to 2.6 in these samples.

2.3.4 EBSD observations

The CPOs characterized by EBSD provide the directions of flow of the solid phase around a bead, as in Figure 2.7. Pole figures indicate moderate CPOs (multiples of uniform distribution (MUD) $<$ 5 in the pole figures), with strongly clustered vertical b-axes but weakly girdled a- and c-axes. The girdled a- and c-axes suggest a combination of a-type ((010)[100]) and b-type ((010)[001]) fabrics, but in both cases, the b-plane is the slip plane. The slip directions for olivine grains (pink lines in Figure 2.7, with lengths proportional to the strength of fabric) are generated from the traces of the

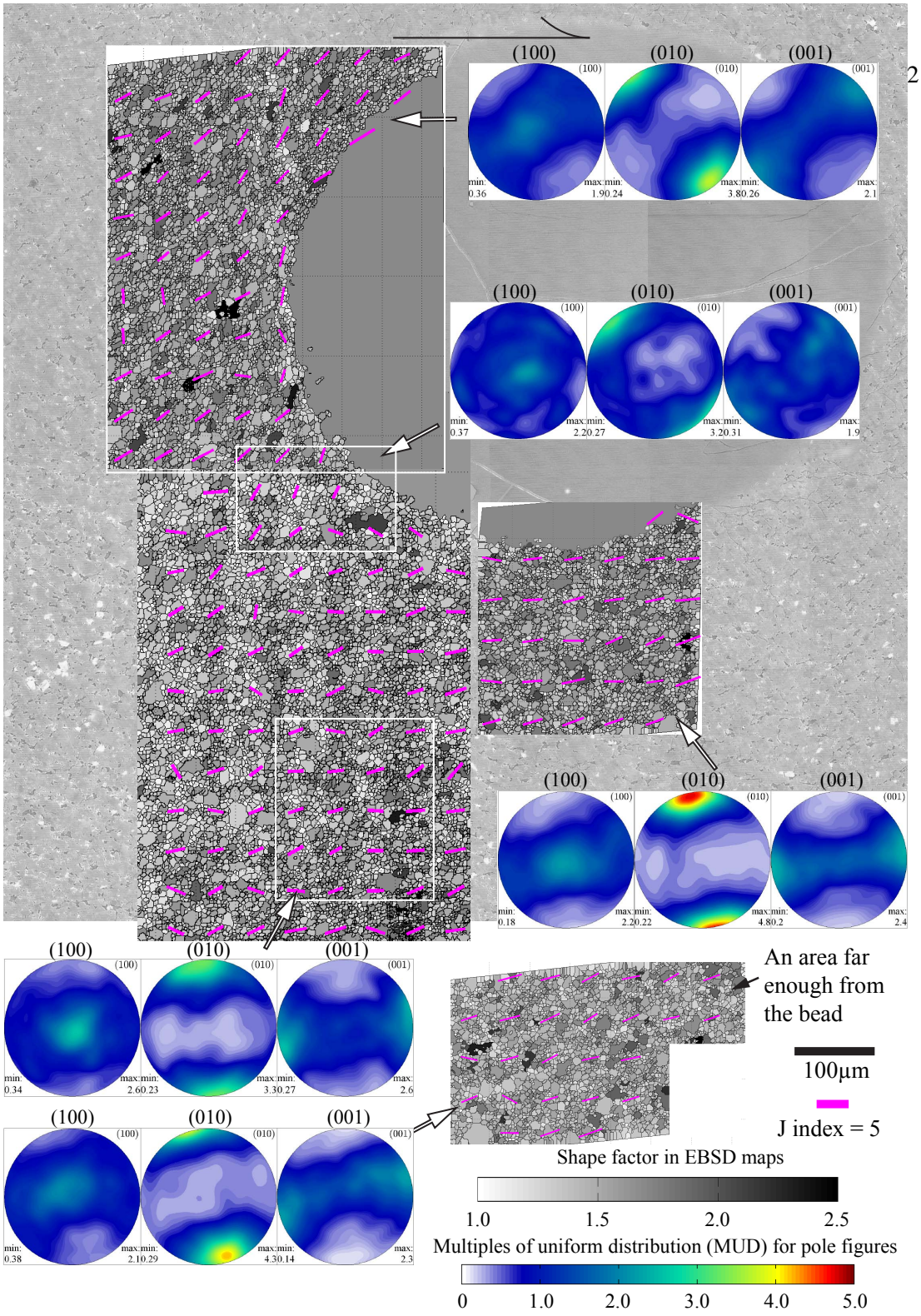

Figure 2.7: Orientation maps for sample PI0609 generated from EBSD data. A crop of the BSE image is shown as the dim background to denote the locations of orientation maps relative to the bead. The orientation maps are color coded by the shape factor of each grain. Step size is 1 μm. Data are indexed as olivine, Fo90. During the reconstruction of grains, un-indexed points (melt, cpx and pores) are removed as noise. The slip directions projected in the observed plane (pink lines) are reconstructed with respect to the directions of b-plane ((010) plane), each averaged from an area of 50×50 μm. The length of each pink line is proportional to the magnitude of the J index. Pole figures are shown for selected regions.

b-planes. Then the flow field of the solid matrix featuring only the flow directions is reconstructed.

2.4 Discussions

2.4.1 Theory of formation of pressure shadows

The tangential section through the center of a bead under torsion approximates a plane of simple shear, as needed to test the theory of pressure-shadow formation. Under simple shear top-to-the-right, the compressive deviatoric stress aligned in the NW-SE direction creates high solid pressure in the NW and SE quadrants of the bead. This stress state, in turn, implies higher liquid pressure at these locations. The same occurs for tensile deviatoric stress aligned along the SW-NE direction. The pressure gradient allows melt to migrate by porous flow, thus reducing the liquid pressure in the NW and SE and increasing the liquid pressure in the SW and NE. The resulting differences between solid and liquid pressure cause compaction (decompaction). In other words, in a stationary external reference frame, melt is "trapped" in the regions under decompaction as the two-phase material moves around the bead. As strain increases, melt accumulates in decompaction regions, NE and SW, forming pressure shadows; while in regions under compaction, NW and SE, melt concentration decreases. This behavior explains the consistency in locations of melt-enriched and melt-depleted regions in Figure 2.6. However, not all of the four regions are observed in every experimental results. The main reason for the absence of one of the four regions is that a melt-enriched band runs through the location of a melt-enriched pressure shadow, which makes it impossible to determine the shape and melt concentration of this melt-enriched region (as sample PI0609 and PI0665 in Figure 2.6(c) to (f)). Although pressure shadows are not identical from sample to sample, pressure gradients induced by the hard bead well explain the formation of pressure shadows.

To obtain a quantitative analysis on the locations and melt fractions of pressure shadows, a donut-shaped region (referred as "donut") between the outer radius of the bead (a) and twice that radius ($2a$) is subdivided into 36 subregions defined by the angle θ around the bead, such that

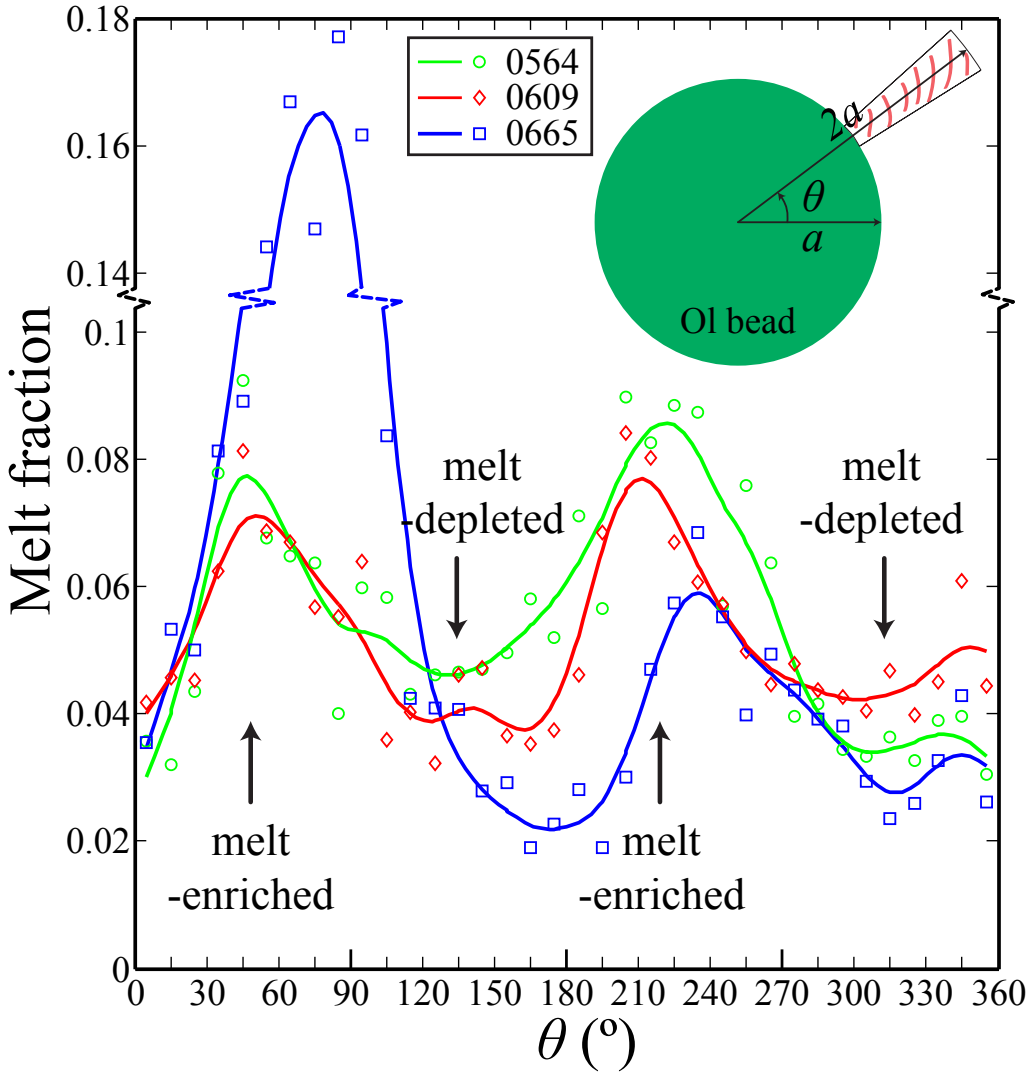

Figure 2.8: Melt distribution around the bead in an 1-D plot. θ is the polar angle that goes around the bead from 0° to 360°. Data points are symbols on the plot, while their spline fits are lines. The region with red marking in the top-right stretch represents from where the data at angle θ is obtained. a is the radius of the bead. Two melt-enriched regions are marked by arrows.

melt fraction in each subregion is plotted versus θ in Figure 2.8. The curve for melt fraction is approximately sinusoidal but with a wider trough than crest. Both curves for sample PI0654 and PI0609 have two crests, representing melt-enriched regions, at $\theta \approx 50^\circ$ and 230°, which are the decompacting NE and SW. The high crest on the curve of sample PI0665 is due to the dominating melt-enriched band running through the top-right region of the bead. Since the band is $\sim 20^\circ$ to the shear direction (as in Figure 2.6(e)), the band cuts through the "donut" between $\theta \approx 50^\circ$ and $\theta \approx 110^\circ$, which explains the shift of the crest of the curve for sample PI0665. Troughs are observed on the curves at $\theta \approx 130^\circ$ and 310°, which are the compacting NW and SE regions. It is also notable that the melt fraction curve has small rises at about 20-30° after the troughs. The small rise in melt fraction is the effect of a secondary, high-angle band, which is observable on the right of the bead in Figure 2.6(e). Except for the band-induced peak in the curve of sample PI0665, the differences in magnitudes of crests and troughs between samples are small. Because these sample were deformed at the same conditions but to different strains, we conclude that once pressure shadows are formed, the locations and melt fractions do not evolve significantly with strain.

With constant temperature, pressure and chemical composition, the growth rate of pressure shadows developed in our laboratory experiments is controlled by the material properties of the partially molten rock, specifically the ratio of bulk to shear viscosity, $R = \zeta/\eta$, based on the theory of *McKenzie and Holness* (2000). In this theory, compacting flow around a rigid sphere is used to model the local deformation of the partially molten material around a hard bead, which is similar to the process in our experiments. Matrix particle pathways around a rotating sphere under simple shear are illustrated in Figure 2.9. Compaction and decompaction are indicated by the convergence and divergence of streamlines, respectively. The locations of the compaction and decompaction regions indicated by matrix particle pathways are qualitatively the same as those in our samples. The theory predicts that the rate of decompaction at the pressure-shadow regions decreases with increasing R.

Due to the rotation of the sphere, matrix velocity and melt flux were not obtained for simple shear by *McKenzie and Holness* (2000), but are provided for pure shear as illustrated in Figure

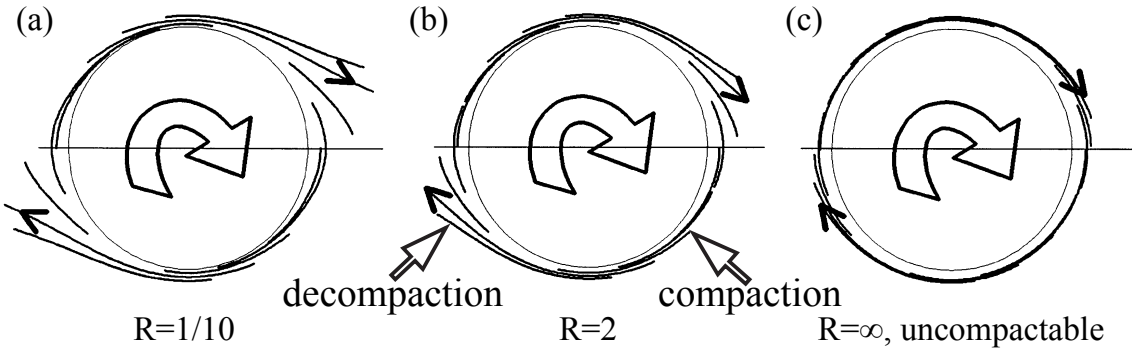

Figure 2.9: Matrix particle paths in the presence of a rigid sphere under simple shear for three values of R: (a) 1/10, (b) 2 and (c) ∞. The sense of shear is top to the right in a frame whose x-axis is fixed (horizontal solid black line in the figures). From *McKenzie and Holness* (2000).

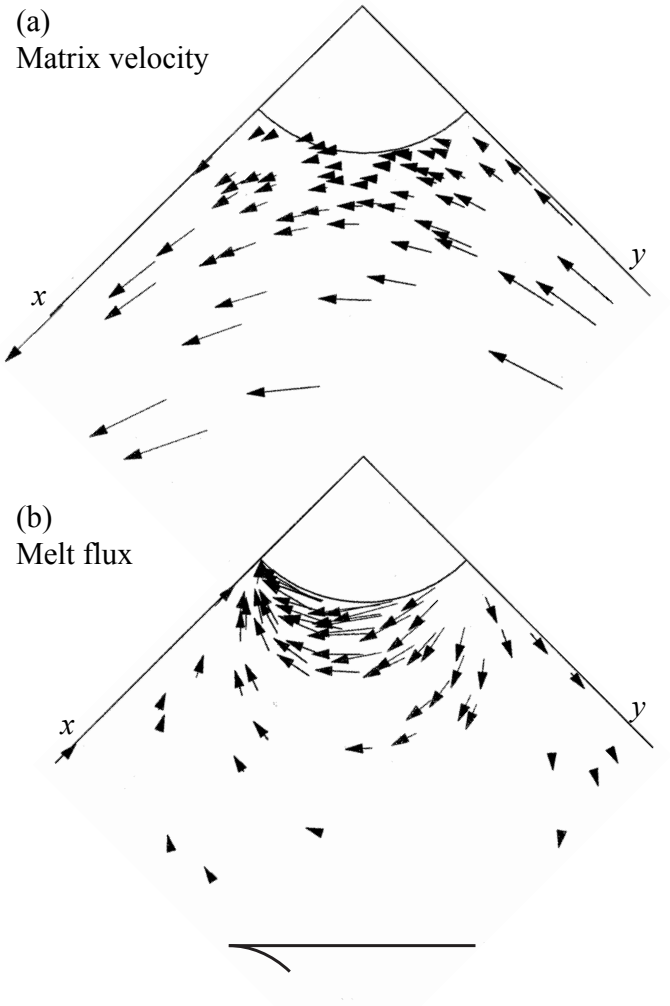

Figure 2.10: The direction and magnitude of (a) matrix velocity and (b) melt flux in one quadrant under compression along y axis. The x and y axes were rotated 135° counterclockwise to compare with experimental results. The black arrow at the bottom shows the corresponding shear direction. R=1/10. After *McKenzie and Holness* (2000).

2.10. In the quadrant shown, the deformation geometry indicated by the arrow in the figure is comparable to simple shear. The locations for melt-enriched and melt-depleted regions indicated by the melt flux in Figure 2.10(b) are the same as those in our samples, but melt flux does not provide further comparison with melt distribution (i.e., accumulation of flux) in samples deformed in the laboratory. The orientations of the flow field determined from CPOs provide a measure of the matrix velocity directions. A comparison between the pink lines in the region to the bottom of the bead in Figure 2.7 with the flow lines in Figure 2.10(a) reveals that the flow directions and the matrix velocity data have the same trend in the compaction region. However, due to the rotation of the bead in the deformation experiments, the similarity breaks down in the decompaction region. It should also be noticed that the analytical results are given for a value of R =1/10. This ratio has not been determined for our samples, but is predicted to be R =2 (*Takei and Holtzman*, 2009a). However, we emphasize that major features observed in our experiments, such as the location of the pressure shadows and the flow directions of the solid matrix, are consistent with those predicted by this theory.

2.4.2 Comparisons with melt segregation

Stress-driven segregation to form melt-enriched bands and pressure shadows have been predicted using the two-phase flow theory of *McKenzie* (1984) (*Stevenson*, 1989; *McKenzie and Holness*, 2000). Stress-driven melt segregation in partially molten rocks has been studied experimentally in both general shear (e.g., *Holtzman et al.*, 2003a) and torsional shear (e.g., *King et al.*, 2010) experiments, while our study is the first time melt-phase pressure shadows were produced in experiments. Some comparisons with previous melt segregation studies are necessary.

To make the comparison, two parameters need to be introduced. The first one is compaction length, δ_c, which is the parameter that combines the properties of the melt, the matrix and the aggregate in two-phase flow theory. The compaction length, δ_c, is given by (*McKenzie*, 1984)

$$\delta_c = \left[\frac{(\zeta + \frac{4}{3}\eta)k}{\mu}\right]^{1/2}, \tag{2.1}$$

where μ is the viscosity of the melt and k is the permeability of the matrix, which is a function of melt fraction, ϕ, and matrix grain size, d. The second parameter is the porosity-weakening (melt-weakening) factor α, which affects the shear viscosity through the relation (*Kelemen et al.*, 1997)

$$\eta(\phi) = \eta_0 \exp(-\alpha\phi), \tag{2.2}$$

where η_0 is shear viscosity for melt-free rock. In olivine + MORB system, $\alpha \approx 26$ for diffusion creep and $\alpha \approx 31$ for dislocation creep (*Mei et al.*, 2002).

Stress-driven segregation to form melt-enriched bands and pressure shadows are compared from their prerequisites and growth rates. Melt-enriched bands develop as a result of initial perturbations in melt fraction (*Stevenson*, 1989). Pressure shadows form in response to pressure gradients induced by the presence of the hard bead. The growth rate of melt-enriched band is proportional to the porosity-weakening factor α, the ratio $R = \zeta/\eta$, and the amplitude of the initial perturbation (*Katz et al.*, 2006). The spacing between segregated melt-enriched bands increase with increasing compaction length, δ_c (*Holtzman et al.*, 2003a; *Kohlstedt et al.*, 2010; *King et al.*, 2010). However, in the case of pressure shadows, the effect of changing δ_c and R has not yet been studied, although compaction rate is predicted to be inversely proportional to R (*McKenzie and Holness*, 2000). As another form of stress-driven melt segregation, pressure-shadow development has similarities with the formation of melt-enriched bands, which could lead to a more profound understanding of the controlling parameters in the development of pressure shadows.

Another purpose of this section is to compare the melt-enriched bands observed close to the beads in our samples with those formed in previous studies. In stress-driven formation of melt-enriched bands reported by *Holtzman et al.* (2003a) and *King et al.* (2010), observable melt-enriched bands occur if sample thickness is larger than or approximately equal to the compaction length. In our samples of olivine + MORB, $\delta_c \gtrsim 10$ mm (*Holtzman et al.*, 2003a), a value larger than the sample thickness, δ_{th}, suggesting that bands should not form. However, melt-enriched bands are observed in samples PI0609 and PI0665 (Figure 2.6(c) and (e)). Although these bands form an angle of $\sim 20^\circ$ to shear direction, similar to that in previous studies, the ratio of melt fraction in

bands to that in non-bands is lower than in previous studies — $\phi_{band}/\phi_{non-band} \approx 0.10/0.05 = 2$ in this study versus $\phi_{band}/\phi_{non-band} \approx 0.14/0.02 = 7$ in *Holtzman et al.* (2003a). The compaction length in our samples is significantly larger than in previous studies, which leads to a larger spacing between bands. This difference provides one possible explanation for the lower band-to-non-band melt fraction ratio, because there are fewer melt-enriched bands form in our samples than in previous studies, in which bands are so abundant that non-band areas are almost melt-depleted.

In summary, we have presented observations of pressure shadows developed in partially molten rocks deformed in torsion. The location and shape of the pressure shadows are not highly sensitive to shear strain. The experimentally observed melt distribution and flow field are consistent with theoretical predictions (*McKenzie and Holness*, 2000).

Chapter 3

Experimental test of the viscous anisotropy hypothesis for partially molten rocks

This chapter is modified from a manuscript that will be submitted to *Science*, co-authored with David L. Kohlstedt, Richard F. Katz and Yasuko Takei.

Chemical differentiation of rocky planets occurs by melt segregation away from the region of melting. The mechanics of this process, however, are complex and incompletely understood. In partially molten rocks undergoing shear deformation, melt pockets between grains align coherently in the stress field (**?***Zimmerman et al.*, 1999); it has been hypothesized that this anisotropy in microstructure creates an anisotropy in the viscosity of the aggregate (*Takei and Holtzman*, 2009a). With the inclusion of anisotropic viscosity, continuum, two-phase-flow models reproduce the emergence and angle of melt-enriched bands that form in laboratory experiments (*Takei and Holtzman*, 2009b; *Takei and Katz*, 2013). In the same theoretical context, these models also predict sample-scale melt migration due to a gradient in shear stress. Under torsional deformation, melt is expected to segregate radially inward (*Takei and Katz*, 2013; *Katz and Takei*, 2013). Here we present new

torsional deformation experiments on partially molten rocks that test this prediction. Microstructural analyses of the distribution of melt and solid reveal a radial gradient in melt fraction, with more melt toward the centre of the cylinder. The extent of this radial melt segregation grows with progressive strain, consistent with theory. The agreement between theoretical prediction and experimental observation provides a validation of this theory, which is critical to understanding the large-scale geodynamic and geochemical evolution of Earth.

3.1 Introduction

Shear deformation of partially molten rocks gives rise to melt segregation into sheets (bands in cross-section) that emerge at a low angle to the shear plane. This mode of segregation was predicted with two-phase flow theory (*Stevenson*, 1989) and subsequently discovered in experiments (*Holtzman et al.*, 2003a; *King et al.*, 2010). It has been proposed that melt-enriched bands, if present in the mantle of Earth, would permit rapid extraction of melt (*Kohlstedt and Holtzman*, 2009), produce significant anisotropy in seismic wave propagation (*Kendall*, 1994), and provide a mechanism for the seismic discontinuity that is, in some places, associated with the lithosphere–asthenosphere boundary (*Kawakatsu et al.*, 2009). The emergence (*Spiegelman*, 2003) and low angle (*Katz et al.*, 2006) of melt-enriched bands under simple-shear deformation can be reproduced using two-phase flow theory with a non-Newtonian, isotropic viscosity. This theory describes the flow of a low-viscosity liquid (melt) through a permeable and viscously deformable solid matrix (grains) (*McKenzie*, 1984). However, an unrealistically strong stress-dependence of viscosity was required to match the low angle of bands observed in experiments (*Katz et al.*, 2006). This disagreement between models and experiments found a possible resolution by the incorporation of anisotropic viscosity arising from coherent alignment of melt pockets between grains (i.e., melt-preferred orientation, MPO) in response to a deviatoric stress (*Takei and Holtzman*, 2009a,c; *Butler*, 2012; *Takei and Katz*, 2013).

Crucially, with the inclusion of viscous anisotropy, two-phase flow theory also predicts a simultaneous but distinct mode of melt segregation driven by large-scale gradients in shear stress.

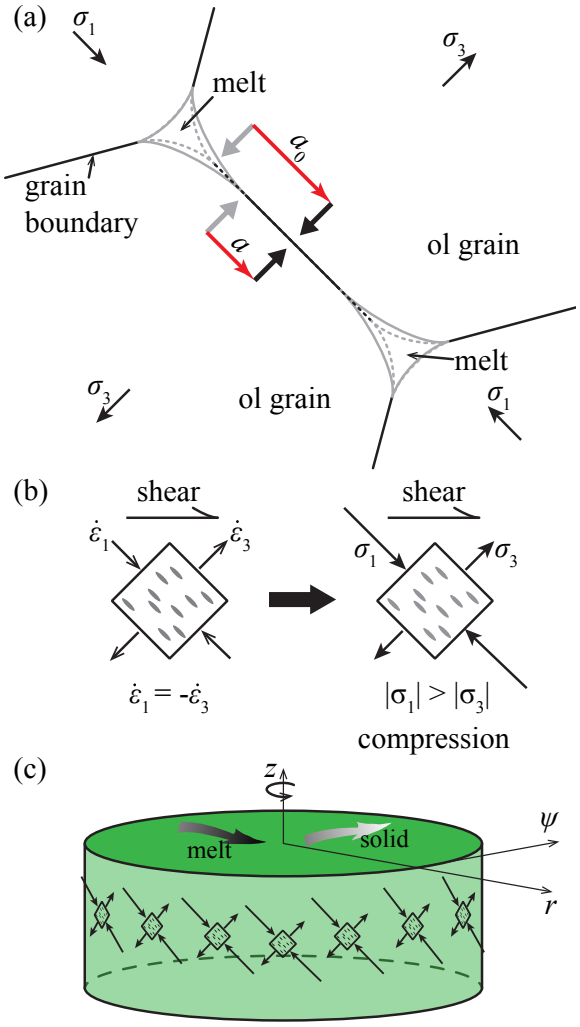

Figure 3.1: Schematic diagrams of the interactions between stress and anisotropic viscosity. (a) Stress-induced melt redistribution and its influence on diffusion pathways in 2D. The grain boundaries in contact with a neighbouring grain are in black, while the grain boundaries in contact with melt are in gray. Melt pockets under isotropic conditions are outlined with dash lines, while the redistributed melt pockets under shear deformation are outlined with solid lines. Red arrows show the lengths of diffusion pathways from the grain-melt boundary (gray arrows) to the centre of a grain boundary (black arrows). The diffusion pathway shortens from a_0 to a with applied deviatoric stress σ_3. (b) The coupling between torsional deformation with zero volumetric strain rate and stress with non-zero volumetric component associated with viscous anisotropy. The square is a REV with melt pockets (gray) aligned 45° to the shear plane, antithetic to the shear direction. Modified from previous study (*Takei and Katz*, 2013). (c) A sample-scale view of the development of the hoop stress from compressive stresses due to cylindrical geometry.

This mode is termed base-state melt segregation (*Takei and Holtzman*, 2009b; *Takei and Katz*, 2013; *Katz and Takei*, 2013). Base-state melt segregation is not predicted if viscosity is isotropic; thus, its occurrence in experiments represents a test of the hypothesis that MPO leads to anisotropy in viscosity. Below we explain base-state melt segregation in more detail; we then present new experimental results that demonstrate its occurrence.

Figure 3.1a illustrates how anisotropy in grain/melt microstructure (i.e., MPO) produces viscous anisotropy through the mechanics of diffusion creep (*Takei and Holtzman*, 2009a). For a representative grain in an aggregate subjected to a deviatoric stress, the contact area with neighbouring grains decreases for grain boundaries that are normal to the direction of the minimum principal stress σ_3 (the minimum eigenvalue of the deviatoric stress tensor; compression positive). A decrease in contact area shortens the diffusion pathway for material transport along this boundary relative to grain boundaries with different orientations. Since melt provides a fast pathway for diffusion, this change in the contiguity between neighbouring grains reduces the timescale of the diffusive response to the σ_3 component of stress. Conversely, an increase in grain–grain contact area in the direction of the maximum principal stress σ_1 lengthens the diffusion pathway on this surface and thus the timescale for diffusive response to stress in this direction.

To translate these concepts from the microscopic to the continuum scale, consider a representative element of volume (REV) that is large enough to contain many microscopic units (grains and melt pockets) and small enough to define a point property at the scale of macroscopic features of interest (Fig. 3.1b). Under deviatoric stress, melt pockets in the REV coherently align normal to the σ_3 direction and the timescale for the diffusive response to stress is reduced in this direction. If the dominant deformation mechanism of the aggregate is diffusion creep, this rapid response imparts a reduction of the continuum viscosity in the σ_3 direction (*Cooper and Kohlstedt*, 1986; *Takei and Holtzman*, 2009a). Likewise, the change in grain contiguity associated with σ_1 increases the viscosity in that direction.

Viscous anisotropy can be quantified with a highly symmetric, fourth-rank tensor (in Appendix B). The orientation of this tensor is described by three angles that rotate it with respect to the system

coordinates. This rotation is used to align anisotropy with the principle directions of deviatoric stress. As a simplifying approximation, we assume that, at each point in the domain, the plane containing σ_1 and σ_3 is parallel to the imposed shear direction and perpendicular to the imposed shear plane. This leaves only one angle to be determined, the angle Θ between the shear plane and the σ_3 direction. The magnitude of anisotropy is parameterised with two scalars: α specifies the viscosity reduction in the σ_3 direction; β specifies the viscosity increase in the σ_1 direction. When either or both α and β are non-zero at a point in the continuum, the viscosity at that point is anisotropic. The associated tensor then has non-zero off-diagonal terms that couple shear stress to normal strain rate (and vice versa). It is these terms that give rise to base-state segregation (*Takei and Holtzman*, 2009b; *Takei and Katz*, 2013).

To clarify the physical mechanism of base-state segregation, consider a cylindrical sample in a sealed chamber, deformed in torsion at a constant twist rate (Fig. 3.1c). Before any deviatoric stress is applied, the grain/melt microstructure is isotropic and the rate of (de)compaction is zero everywhere within the sample. With initiation of twisting, as a consequence of the deviatoric stress, a MPO develops and the viscosity becomes anisotropic. The imposed strain rate, aligned melt pockets, and consequent pattern of stress are shown schematically in Figure 3.1b–c. The disparity between $|\sigma_1|$ and $|\sigma_3|$ gives rise to a net compression that, because it is everywhere tangent to the cylinder, is a compressive hoop stress. This compressive hoop stress pushes the solid grains radially outward and causes a pressure gradient that drives melt radially inward (*Takei and Katz*, 2013) (details provided in Appendix B). This differential motion is the base-state melt segregation under torsional deformation.

3.2 Methods

3.2.1 Sample preparation

Samples were fabricated from mixtures of fine-grained San Carlos olivine, plus 10 vol.% alkali basalt from Hawaii (*Morgan and Liang*, 2003). Olivine powders were obtained by grinding San

Carlos olivine crystals in a fluid-energy mill to produce a particle size of 2 μm. Before mechanically mixing with alkali basalt powders with a particle size of $\sim$10 μm, the olivine powders were dried at 1373 K for 12 h at an fO_2 near the Ni-NiO buffer to remove water and carbon-based impurities introduced during the grinding process. Mixtures were uniaxially cold-pressed at 100 MPa into nickel capsules and then hydrostatically hot-pressed at 1473 K and 300 MPa for 3.5 h in a gas-medium apparatus (*Paterson and Olgaard*, 2000). After hot-pressing, samples were cut into thin cylinders with a diameter of $\sim$12 mm and a thickness of 3 to 5 mm. The cut sample was then placed into a nickel capsule with spacers cored from a coarse-grained natural dunite as end caps, thus providing non-reactive, impermeable boundaries during deformation (*Qi et al.*, 2013). The sample, Al_2O_3 spacers and pistons, and ZrO_2 pistons were enclosed in an iron jacket for deformation.

3.2.2 Experiments

Torsion experiments were conducted at a constant shear strain rate of $10^{-3.5}$ s^{-1}, a temperature of 1473 K, and a confining pressure of 300 MPa in a gas-medium apparatus fitted with a torsion actuator (*Paterson and Olgaard*, 2000). After achieving the target strain, each sample was cooled rapidly ($\sim$2 K/s) to 1300 K under the same torque as imposed at the end of the deformation experiment to preserve the deformation-produced microstructure and then cooled to room temperature with no torque applied. After deformation, with the iron jacket and the nickel capsule dissolved by acid, the deformed sample was cut in half perpendicular to torsional axis, leaving two transverse sections for examinations. Each transverse section was polished on a series of diamond lapping films down to 0.5 μm, followed by a final step using colloidal silica. The section was then examined by reflected-light optical microscopy after chemically etching with diluted HF to highlight melt pockets.

3.2.3 Image analysis

To map the whole transverse section with an area of $\sim$113 mm^2, a mosaic image consisting of 2209 high-resolution (0.3 μm per pixel) optical micrographs was used. A binary image with melt

Table 3.1: Experiments Summary.

Sample	$\gamma(R)$	$\dot{\varepsilon}_{eq}$ (s^{-1})	σ_{eq} (MPa)	ϕ_{max}/ϕ_{min}
PI0767	11.1	2.29×10^{-4}	187	1.6
PI0811	5.6	1.84×10^{-4}	237	1.2
PI0812	5.8	1.84×10^{-4}	163	1.4
PI0817	5.0	2.35×10^{-4}	197	1.3
PI0839	7.3	1.84×10^{-4}	237	1.7
PI0891	14.3	2.04×10^{-4}	179	2.0

Note: $\gamma(R)$ is the outer-radius shear strain. σ_{eq} and $\dot{\varepsilon}_{eq}$ are equivalent stress and strain rate. ϕ_{max}/ϕ_{min} is the ratio of maximum to minimum melt fraction.

appearing white was created from this mosaic image using using a combined image segmentation method, which includes edge detection (*Canny*, 1986; *Lim*, 1990; *Parker*, 2010) and a threshold of grayscale. Then a profile of melt fraction was calculated from the area fraction of the white pixels.

3.3 Results and Discussions

To test this prediction and hence the hypothesis that viscosity is anisotropic, we imposed a constant twist-rate on cylindrical samples of partially molten rock that initially had uniform melt fraction (Table 3.1). In tangential sections of quenched samples that were deformed in torsion (Fig. 3.2), we observe aligned melt pockets and low angle, melt-enriched bands. Melt-enriched bands are also evident in transverse sections (Fig. 3.3). More importantly, analyses of optical micrographs of transverse sections reveal a gradient in melt fraction in the radial direction, with melt concentrated toward the axis of the cylinder. This gradient in melt fraction corresponds to the base-state melt segregation predicted if viscosity is anisotropic. Our observations of MPO, melt-enriched bands, and radial melt segregation are detailed in subsequent paragraphs.

The rose diagram in Figure 3.2b demonstrates that at a local shear strain of $\gamma = 4.6$, melt pockets are aligned at $\sim$29° to the shear plane, antithetic to shear direction. In contrast, the expected σ_3 direction, based on cylindrical simple shear flow with isotropic viscosity, is 45° to the shear plane. The observed low angle of melt alignment means that, at this shear strain, either melt pockets are not normal to the σ_3 direction (*Zimmerman et al.*, 1999) or σ_3 has rotated counter-clockwise. The reason for this alignment is unknown; it might be due to the emergence of chains of melt pockets (*Holtzman and Kohlstedt*, 2007) (Fig. 3.2c) or to the anisotropic viscosity itself. In the theory of two-phase flow with viscous anisotropy, elaborated in the Supplementary Material, it is generally assumed that melt pockets align perpendicular to σ_3, as suggested by deformation experiments on an analogue material at small strains ($\gamma < 0.2$) (*Takei*, 2010). The observed MPO, therefore, may represent a subtle but important discrepancy between observation and theory that we return to below. Despite this possible discrepancy, the observed, strong MPO demonstrates the microstructural anisotropy that hypothetically causes viscous anisotropy.

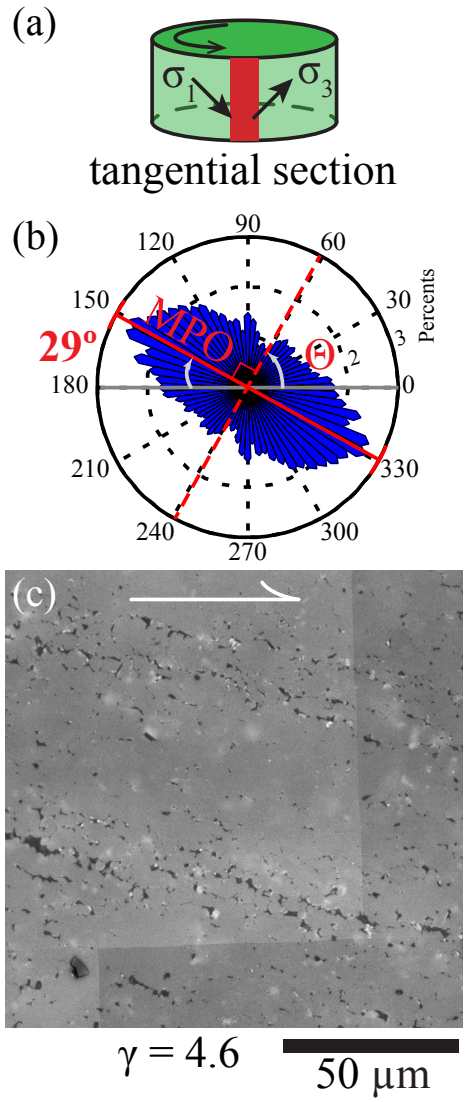

Figure 3.2: MPO in a sample deformed to a shear strain of 4.6. (a) A sketch illustrating a deformed cylindrical sample with its tangential section marked in red. Arrows in this sketch illustrate the expected directions of deviatoric stresses σ_1 and σ_3 in tangential section. (b) A rose diagram generated from optical micrographs of the tangential section at a local shear strain of $\gamma = 4.6$ (PI0817). The rose diagram was constructed from more than 1000 melt pockets with areas larger than 2 μm^2. The length of each petal represents the ratio of melt pockets with this certain orientation, scaled by percentage. Θ is anisotropy angle, which the angle between red, dashed lines and 0°. (c) Optical micrograph from the tangential section of the sample. Olivine grains are light gray; melt is dark gray; internal reflections or residual polishing material are white. The sense of shear is marked by the arrow on top.

Two-phase flow theory with anisotropic viscosity (*Takei and Katz*, 2013) also predicts the emergence of sheets of high melt fraction that appear as bands in two-dimensional sections (*King et al.*, 2010). In Figure 3.3, these features appear as radial lines of high melt fraction where sheets cross the transverse section. For the sample deformed to an outer-radius shear strain of $\gamma(R) = 5.0$ (Fig. 3.3a, c), the melt-enriched bands are distributed uniformly around the cylinder, whereas at a larger strain of $\gamma(R) = 14.3$ (Fig. 3.3b, d), the azimuthal distribution of melt-enriched bands is inhomogeneous, dominated by several extraordinarily large bands. Because the total strain decreases toward the centre of the cylinder, the region close to axial centre exhibits less banding. More significantly, however, Figures 3.3c and d demonstrate a general increase in melt fraction toward the centre of the cylinder, consistent with the predicted base-state migration of melt radially inward.

Radial profiles of the azimuthally averaged, normalized melt fraction are presented in Figure 3.4a for seven experiments, each with a different final strain. The melt fraction in an experiment with no deformation (grey line) varies by less than 10% along a radius. In all deformed samples, the melt fraction increases toward the centre of the cylinder — evidence for base-state segregation. For the three samples deformed to an outer-radius shear strain of $\gamma(R) = 5.5 \pm 0.5$, each radial profile of melt concentration reaches its peak at a radius of $r^{\text{peak}} \approx 1$ mm, corresponding to a shear strain of $\gamma(r^{\text{peak}}) \approx 1$. Melt fraction decreases from that point toward the axis of the cylinder; this behavior is expected because the low-stress/low-strain region at small radius has little or no MPO and hence has essentially isotropic viscosity ($\alpha = \beta = 0$). For samples deformed to higher outer-radius shear strains ($\gamma(R) = 7.3$, 11.1, and 14.3), peaks in melt fraction occur at a radius of $r^{\text{peak}} < 0.2$ mm. The sample with the highest outer-radius shear strain ($\gamma(R) = 14.3$) exhibits the largest ratio of maximum to minimum melt fraction $\phi_{\text{max}}/\phi_{\text{min}}$ (Table 3.1), a measure of the strength of base-state melt segregation. Except for the samples sheared to outer-radius shear strains of $\gamma(R) = 5.0$ and 7.3, the maximum in melt fraction increases with increasing shear strain. In summary, the results presented in Figure 3.4a demonstrate that, with increasing strain, the pressure gradient induced by anisotropic viscosity drives melt inward, increasing the maximum value of the azimuthally averaged melt fraction and decreasing the radius at which this maximum occurs.

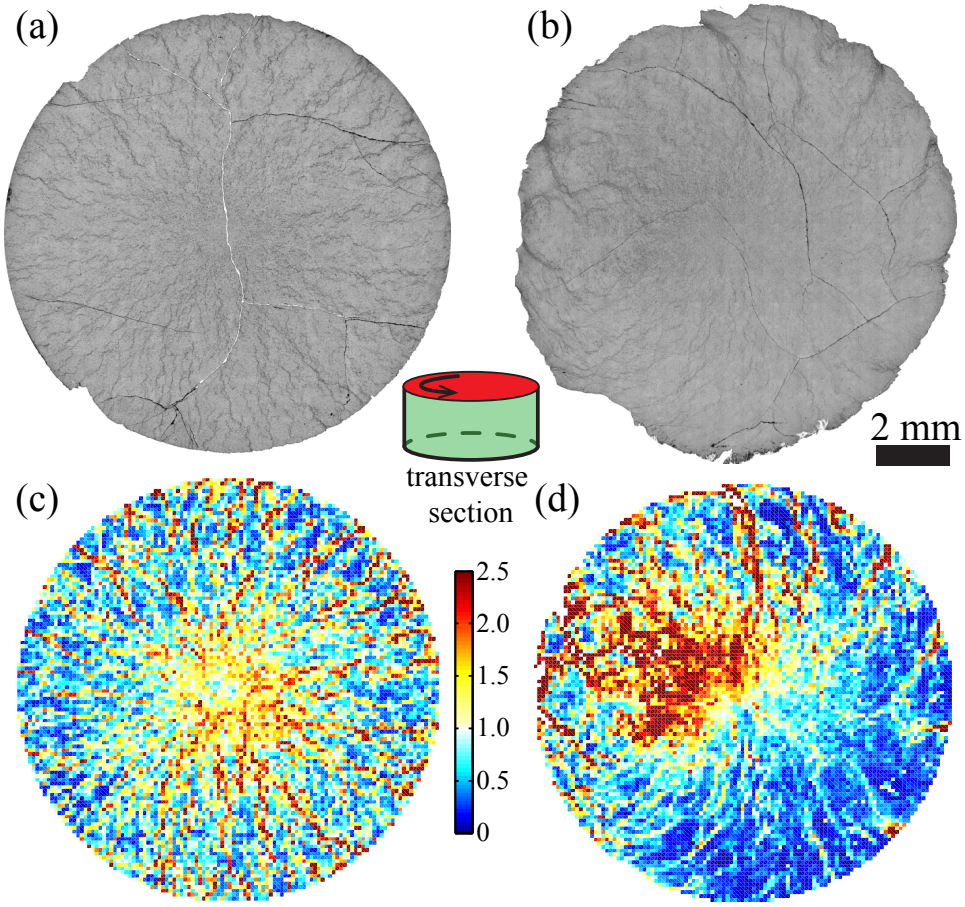

Figure 3.3: Optical micrographs and processed images demonstrating base-state melt segregation. (a) and (b), Optical micrographs of transverse sections from samples sheared to $\gamma(R) = 5.0$ (PI0817) and 14.3 (PI0891), respectively. Olivine is light gray and melt is dark gray. The sketch located between (a) and (b) is a deformed cylindrical sample with its transverse section marked in red. (c) and (d), Melt distribution maps generated from (a) and (b), respectively. The grid size is 100×100 μm. Color bar indicates melt fraction normalized to the average melt fraction in the image. Due to its high strain, sample PI0891 sheared off-axis so that the torsional axis is to the northwest of the centre of the image.

Figure 3.4b compares the azimuthally averaged profiles of normalized melt fraction from three samples deformed to $\gamma(R) = 5.5 \pm 0.5$ with those derived from numerical simulations. The data points in 3.4b, which are the mean values of the of the azimuthal averages at each radius, reach a maximum normalized melt fraction of $\sim$1.15 at $r^{\text{peak}} \approx 1$ mm and a minimum of $\sim$0.95 at $r \approx 4$ mm. For comparison, radial profiles of melt fraction from numerical simulations of samples deformed to $\gamma(R) = 5.5$ at an initial compaction length of $\delta_c = 0.1R$ and a bulk-to-shear viscosity ratio of $r_\xi = 10$. In the simulations, two conditions are used for the angle of viscous anisotropy: (1) $\Theta = 45°$, suggested by previous experiments (*Takei*, 2010), and (2) $\Theta = 60°$, suggested by Figure 3.2. The other variable in the simulations is the magnitude of viscous anisotropy. In all four simulations, α increases from zero at the centre of the cylinder to $\alpha_{\text{max}} = 2$ at $r \approx 1$ mm and then remains constant at larger radii. In two of the simulations, β mimics the behavior of α. In the other two simulations, β is zero at all radii. In the decompaction region (i.e. at small radii), profiles with $\Theta = 45°$ exhibit higher melt fractions than those with $\Theta = 60°$, while profiles with $\alpha_{\text{max}} = \beta_{\text{max}} = 2$ exhibit higher melt fractions than those with $\alpha_{\text{max}} = 2$ and $\beta = 0$. The profile with $\Theta = 60°$ and $\alpha_{\text{max}} = \beta_{\text{max}} = 2$ is in the most consistent with the experimental results. However, some clear differences exist between the simulated and the experimental profiles. First, for $2.6 < r < 4.4$ mm the simulated profiles lie above experimentally measured profile. Second, the abrupt decrease in the simulated profiles at $r > 4.4$ mm was not observed experimentally. Despite these quantitative discrepancies, all simulated porosity profiles are in good qualitative agreement with those from experiments, in terms of both the amplitude and the radial position of the porosity maximum.

3.4 Conclusions

In this paper we presented experimental observations of the radial distribution of melt in partially molten rocks deformed in torsion to large strain. For this deformation geometry, the theory of melt segregation with anisotropic viscosity predict a radial distribution of melt fraction. The inclusion

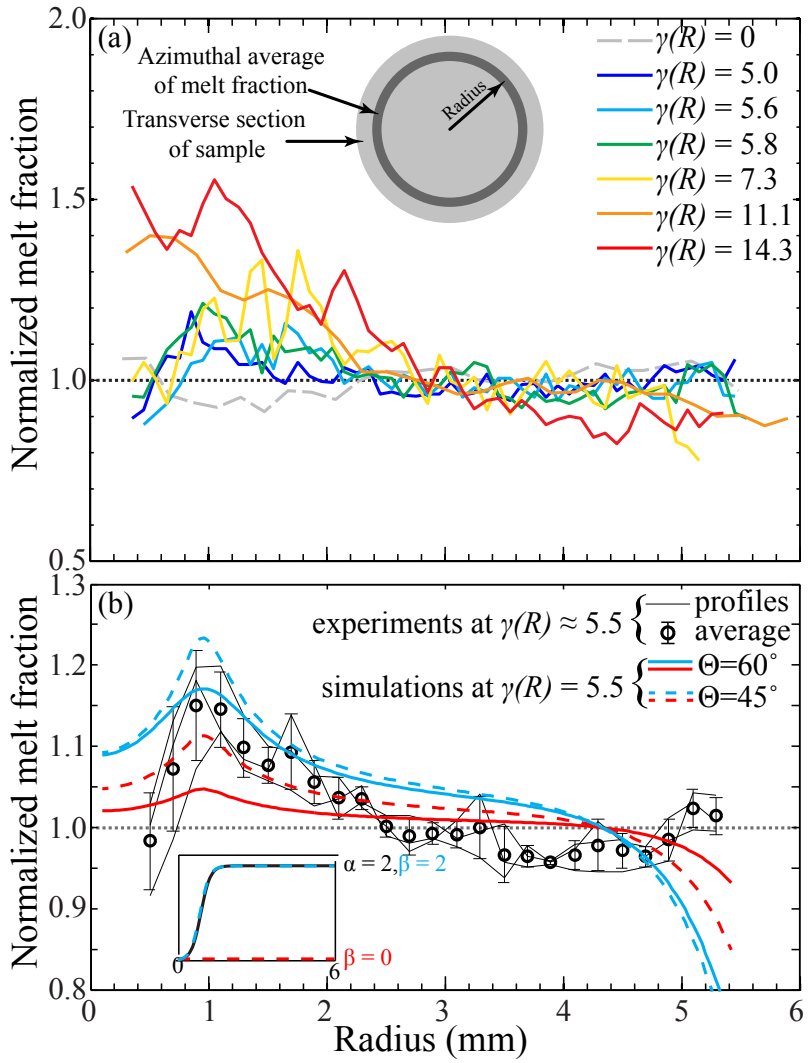

Figure 3.4: Azimuthally averaged, normalized melt fraction versus radius. (a) Plot of azimuthally averaged, normalized melt fraction versus radius for starting material and six deformed samples. In the legend, the outer-radius strain of each sample is noted. Melt fraction is normalized by the average value of the transverse section of each sample. The black dotted line corresponds to a normalized melt fraction of 1.0. The sketch shows how an azimuthal average of melt fraction is obtained for a given radius. (b) Reproducibility test for three samples sheared to $\gamma(R) = 5.5 \pm 0.5$ and its comparison with the results from numerical simulations. Simulations were conducted with an initial compaction length of $\delta_c = 0.1R$, a bulk-to-shear viscosity ratio of $r_\xi = 10$, anisotropy angles of $\Theta = 60°$ and $45°$, and anisotropy magnitudes $\alpha(r)$ and $\beta(r)$ shown in the inset panel. Blue lines are for the case with $\alpha_{\max} = 2$ and $\beta_{\max} = 2$, while red lines are for the case with $\alpha_{\max} = 2$ and $\beta = 0$. There was no initial porosity perturbation and hence no band formation.

of viscous anisotropy in the theory is a necessary and sufficient condition for the development of radially inward, base-state melt segregation. Our experiments test this prediction, and the results reported here are in general agreement with theory, validating the viscous-anisotropy hypothesis. This experimental validation of MPO-induced viscous anisotropy represents a significant advance in our understanding of the relationship between microstructure and continuum mechanics of partially molten rocks, and it also exposes details of the linkage between deformation, MPO and viscosity that are not captured by present models. In Earth, partially melting largely occurs in regions of active deformation — places where melt-preferred orientation will occur. Inclusion of viscous anisotropy in models of the dynamics of the partial molten mantle will likely predict shear-induced melt migration that profoundly influences melt segregation, mantle dynamics, and chemical evolution of our planet.

Chapter 4

Influence of compaction length on compaction rate in base-state melt segregation

The redistribution of melt in partially molten rocks during deformation plays an important role in the evolution and dynamics of Earth's mantle. The redistribution of melt observed in experiments, including melt alignment (*Zimmerman et al.*, 1999) and formation of melt-enriched bands (*Holtzman et al.*, 2003a; *King et al.*, 2010), results in a significant anisotropy in microstructure. A recent hypothesis incorporates the anisotropy in microstructure with the anisotropy in the viscosity of the two-phase aggregates (*Takei and Holtzman*, 2009a). Including anisotropic viscosity, two-phase flow theory not only reproduces the low-angle melt-enriched bands formed in laboratory experiments, but also predicts a sample-scale melt migration induced by a gradient in shear stress, namely base-state melt segregation (*Takei and Katz*, 2013). The existence of base-state melt segregation has been tested by an observed decrease in melt fraction with increasing radius in a series of torsion experiments, which validates the hypothesis of viscous anisotropy (Chapter 3).

Here, we present new torsion experiments to investigate the compaction rate in base-state melt segregation. Using samples consisting of three different melts, a large variant in compaction length is achieved. Microstructural analyses of experimental products for the distribution of melt and solid reveal the influence of compaction length on compaction rate. This experimental result will provide inspirations for theoreticians and modelers to improve the two-phase flow theory with anisotropic viscosity, as part of contributing to a deeper understanding of Earth's dynamics and evolution.

4.1 Introduction

Segregation of melt at places under intense deformation in the mantle influences the large-scale dynamic behavior of the Earth's deep interior. As a response to shear deformation, stress-driven melt segregation into low-angle, melt-enriched sheets (bands in cross section) occurs in laboratory experiments of partially molten mantle rocks (*Holtzman et al.*, 2003a; *King et al.*, 2010; *Kohlstedt et al.*, 2010). Evidences from field observations of melt residues and frozen melt-rich structures support the existence of melt-enriched bands in the mantle (*Kelemen et al.*, 1997; *Le Roux et al.*, 2008; *Kaczmarek and Müntener*, 2008). If present in the mantle, such melt-enriched channels would permit rapid extraction of melt (*Kohlstedt and Holtzman*, 2009), produce significant anisotropy in seismic wave propagation (*Kendall*, 1994), and provide a mechanism for lubricating the lithosphere-asthenosphere boundary (*Holtzman and Kendall*, 2010). Thus, modeling this process is of great interest to both geodynamicists and geochemists. (e.g., *Spiegelman*, 2003; *Katz et al.*, 2006; *Takei and Holtzman*, 2009a; *Butler*, 2012).

Although stress-driven melt segregation to form melt-enriched sheets was predicted over two decades ago (*Stevenson*, 1989), an important advance in accurately modeling the emergence and melt-enriched bands at a low angle to the shear plane occurred only a few years ago. Based on the two-phase flow theory, in which a low-viscosity liquid (melt) flows through a permeable and viscously deformable solid matrix (grains) (*McKenzie*, 1984), numerical simulations reproduced the low-angle, melt-enriched bands observed in simple shear experiments (*Katz et al.*, 2006). However, their simulations invoked an unrealistically strong dependence of strain rate on stress in order

to match the low angle observed in experiments for the melt-enriched bands. This situation was recently resolved by incorporating a hypothesis that an anisotropy in viscosity is induced by the coherent alignment of melt pockets at the grain scale in response to a deviatoric stress (*Takei and Holtzman*, 2009a,c). Based on two-phase flow theory incorporating viscous anisotropy, simulations reproduced not only the emergence but also the low angle of melt-enriched bands (*Takei and Holtzman*, 2009b; *Takei and Katz*, 2013). If valid, viscous anisotropy in two-phase flow theory could significantly advance our understanding of the relationship between microstructure and macrostructure of partially molten rocks.

Recent analysis of the melt distribution in partially molten rocks deformed in torsion experiments provided a test of the importance of viscous anisotropy (Chapter 3). In that test, the observed decrease in melt fraction with increasing radial distance from the axial center of samples corresponded to the behavior predicted for base-state melt segregation. Driven by large-scale gradients in shear stress, base-state melt segregation moves melt radially inward in partially molten rocks deformed under torsion (*Takei and Katz*, 2013; *Katz and Takei*, 2013). The process of the base-state melt segregation, elaborated mathematically by *Takei and Katz* (2013) and described physically by in Chapter 3, can be summarized as following: (*i*) deviatoric stresses induce grain-scale alignment of melt normal to the direction of minimum principal stress σ_3 (the minimum eigenvalue of the deviatoric stress tensor with compression positive), (*ii*) this anisotropy in melt distribution causes an anisotropy in viscosity by shortening (or lengthening) the diffusion pathway on the surface normal to σ_3 (or the maximum principal stress σ_1), (*iii*) in a cylindrical sample deformed in torsion at a constant twist rate, anisotropic viscosity gives rise to a disparity between $|\sigma_1|$ and $|\sigma_3|$ (for isotropic condition, $\sigma_1 = -\sigma_3$, for anisotropic condition $|\sigma_1| > |\sigma_3|$), which results in a compressive hoop stress, and (*iv*) this compressive hoop stress pushes the solid grains radially outward, causing a pressure gradient that drives melt radially inward. In step (*i*), the angle of viscous anisotropy is defined as the angle Θ between the shear plane and the σ_3 direction; while the magnitude of viscous anisotropy due to the melt-preferred orientation (MPO) is parameterised with two scalars: α specifies the viscosity reduction in the σ_3 direction, and β specifies the viscosity increase in the

σ_1 direction (see Appendix B). Because step (*i*) results in a measurable MPO and step (*iv*) causes a measurable radial redistribution of melt, this process can be quantified. Thus, not predicted by theories with isotropic viscosity, this distinct type of melt segregation allows not only validation of the hypothesis but also facilitates improvement of two-phase flow theory by incorporating viscous anisotropy.

To investigate two-phase flow theory with anisotropic viscosity, we controlled the rate of base-state melt segregation in laboratory experiments. As noted by *Takei and Katz* (2013), the rate of base-state melt segregation depends strongly on the compaction length relative to the domain size, δ_c/H, where H is the height of the domain, that is, the sample from the view point of an experimentalist. The compaction length, δ_c, a fundamental length scale over which the compaction rate decrease by a factor e, is defined by *McKenzie* (1984) as

$$\delta_c = \left[\frac{(\zeta + \frac{4}{3}\eta)k}{\mu}\right]^{1/2}, \tag{4.1}$$

where ζ and η are the bulk and shear viscosities of the matrix, μ is the viscosity of the melt and k is the permeability of the matrix. Therefore, by varying the compaction length, this base-state melt segregation process can be controlled in experiments.

Here we present new experimental results on the influences of compaction length on the rate of base-state melt segregation. To vary the compaction length, samples were fabricated from olivine plus melt of three different compositions, selected to provide a large variation in the melt viscosity. Constant-temperature, constant-pressure torsion experiments were designed to deform samples with a controlled melt fraction at a fixed strain rate to achieve a predetermined finite shear strain for all melt compositions. Each melt fraction profile was scaled by the time spent in each experiment to compute a compaction rate, $\mathscr{C}$. With all other variables combined into the normalized compaction length, δ_c/H, the relationship between $\mathscr{C}$ and δ_c/H illustrates the influences of compaction length on compaction rate. This result is compared with numerical simulations based on two-phase flow theory including viscous anisotropy to test theory against experiment. With this theory, it becomes possible to advance our understanding of earth dynamics and evolutions.

4.2 Methods

4.2.1 Sample preparation and deformation assembly

Samples were fabricated from mixtures of fine-grained San Carlos olivine plus ∼10 vol.% of powdered albite, alkali basalt from Hawaii (*Morgan and Liang*, 2003), or a 2:1 mixture of Li-metasilicate (Li_2SiO_3) and quartz powders (*Renner et al.*, 2003). Olivine powders were obtained by grinding San Carlos olivine crystals in a fluid-energy mill to produce a particle size of 2 μm. Before mechanically mixing with powders of the second phase, the olivine powders were dried at 1373 K for 12 h at an fO_2 near the Ni-NiO buffer to remove water and carbon-based impurities introduced during the grinding process.

Mixtures were uniaxially cold-pressed at 100 MPa into nickel capsules and then hydrostatically hot-pressed at 1473 K and 300 MPa for 3.5 h in a gas-medium apparatus (*Paterson and Olgaard*, 2000). A vertical groove made on the inner surface of each nickel capsule was used to produce a strain marker on the outer surface of the sample. After hot-pressing, the starting material was cut into cylindrical samples ∼12 mm in diameter and 3 to 5 mm in height. A sample was then placed into a nickel capsule with spacers cored from a coarse-grained natural dunite as end caps, thus providing non-reactive, impermeable boundaries during deformation. The sample, dunite spacers, porous Al_2O_3 spacers, solid Al_2O_3 spacers and pistons, and ZrO_2 pistons were enclosed in an iron jacket for deformation (e.g., *King et al.*, 2010; *Paterson and Olgaard*, 2000) (as described in Chapter 1).

4.2.2 Experiments

Torsion experiments were conducted at a temperature of 1473 K and confining pressure of 300 MPa in a gas-medium apparatus fitted with a torsion actuator (*Paterson and Olgaard*, 2000). Experiments were designed to induce base-state melt segregation in a series of samples deformed at approximately the same strain rate to different finite strains. Samples were deformed at constant twist rates, yielding a constant outer-radius shear strain rate of $\dot{\gamma} \approx 10^{-3.5}$ s^{-1}, to outer-radius

shear strains of $5.0 \leq \gamma \leq 14.3$. After achieving the target strain, each sample was cooled rapidly ($\sim$2 K/s) to 1300 K under the same torque as imposed at the end of the deformation experiment to preserve the deformation-produced microstructure and then cooled to room temperature with no torque applied.

After deformation, the iron jacket and the nickel capsule were dissolved with acid, revealing the strain marker on the outer surface of the sample. The shear strain of a sample was determined precisely by measuring the angle of this strain marker relative to shear direction. Then the deformed sample was cut perpendicular to the torsional axis, leaving a transverse section for examination. Each transverse section was polished on a series of diamond lapping films down to 0.5 μm, followed by a final step using colloidal silica. The section was then examined by reflected-light optical microscopy after chemically etching with diluted HF to highlight melt pockets.

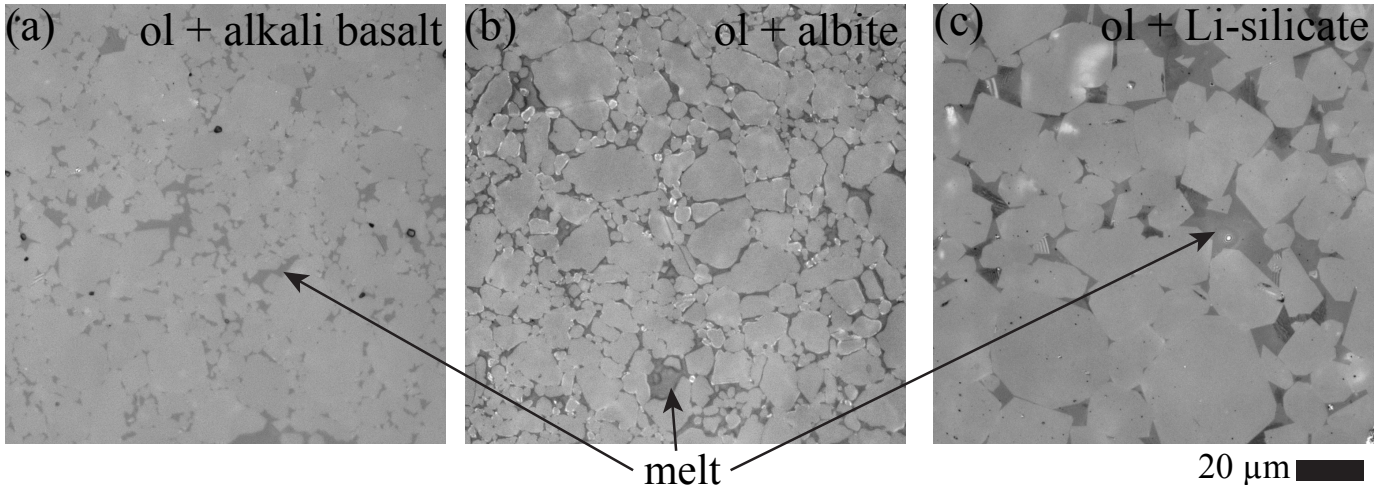

Figure 4.1: Reflected-light, optical micrographs of hot-pressed samples. Olivine grains are light gray, melt is dark gray, and air pores in (a) are black. (a) Hot-pressed sample of olivine + alkali basalt. (b) Hot-pressed sample of olivine + albite. (c) Hot-pressed sample of olivine + Li-silicate.

4.2.3 Image analysis

With an optical microscope, each transverse section was mapped with a mosaic image consisting of as many as 2409 reflected-light, high-resolution (0.3 μm per pixel) micrographs. A binary image with melt appearing white was created from each single micrograph using a combined image segmentation method, which includes edge detection (*Canny*, 1986; *Lim*, 1990; *Parker*, 2010) and a threshold of grayscale. The segmented binary images were stitched back together for the calculation of radial distribution of melt. The stitched image was then divided into a continuous series of 0.1-mm-wide rings as a function of radius from the center of the transverse section. For each ring, the area fraction of white pixels was obtained and used as the azimuthally averaged melt fraction at this certain radius. Thus, a radial profile of melt distribution was created. After examining the transverse sections, optical micrographs were also taken on tangential sections, which were polished with the same procedure as introduced above.

4.3 Results

4.3.1 Starting material

After isostatic hot-pressing, melt in our samples occupies all triple junctions, some two grain interfaces, and a few larger pockets, as illustrated in Figure 4.1. During the 3.5-h hot-pressing, olivine grains grew from an initial particle size of 2 μm to a final mean grain size, d, of $d_{\text{basalt}} \approx 9$ μm for olivine + alkali basalt samples, $d_{\text{albite}} \approx 7$ μm for olivine + albite samples, and $d_{\text{Li-sil}} \approx 16$ μm for olivine + Li-silicate samples. The average melt fraction of a hot-pressed sample, $\bar{\phi}_0$, is approximately 0.07 for samples composed of olivine + alkali basalt and olivine + albite, and 0.10 for samples of olivine + Li-silicate. The decrease in melt fraction in the olivine + alkali basalt and olivine + albite samples results from re-equilibration between melt and olivine. Melt pockets occur through out the samples with sizes varying from <1 μm to $\sim$15 μm in olivine + alkali basalt and olivine + albite samples (Figure 4.1(a) and (b)), and up to $\sim$ 30 μm in olivine + Li-silicate samples (Figure 4.1(c)). In terms of dihedral angle, the microstructures of olivine + albite and olivine

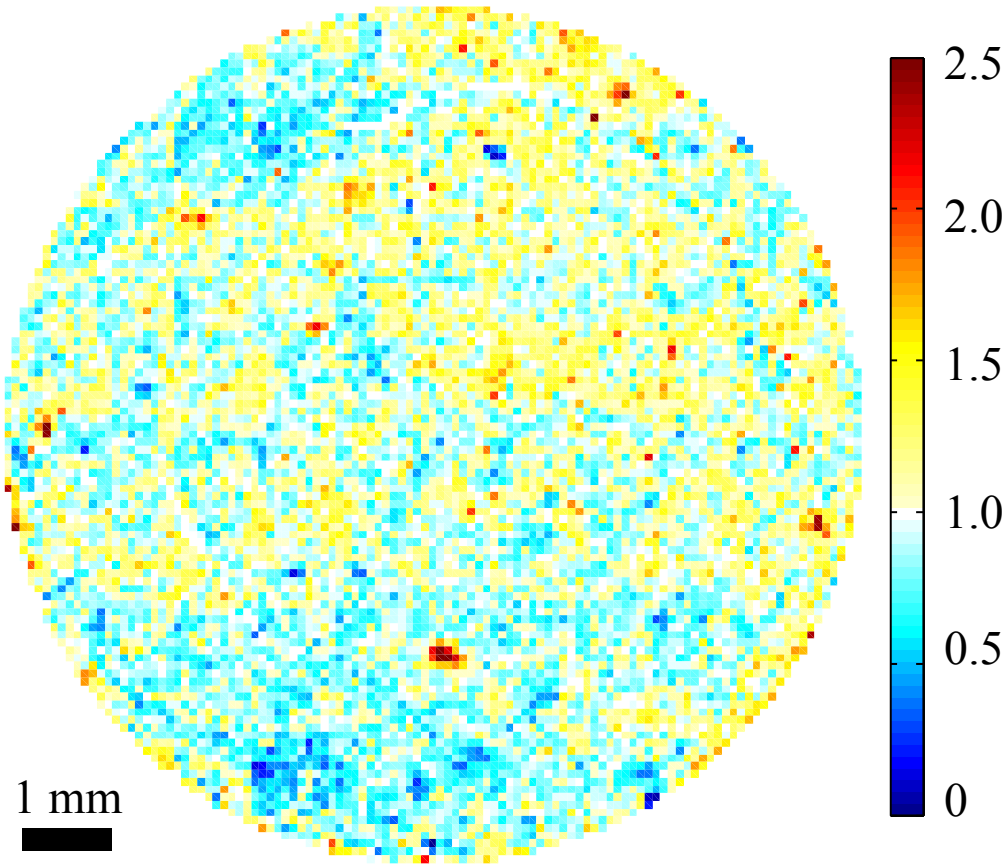

Figure 4.2: Color map of melt distribution of a hot-pressed sample of olivine + albite with a resolution of 100×100 μm per pixel. Color bar illustrates melt fraction normalized by the average value.

+ Li-silicate samples are similar to those of olivine + alkali basalt samples and partially molten olivine aggregates in previous studies (e.g., *Waff and Bulau*, 1979; *von Bargen and Waff*, 1986; *Cooper and Kohlstedt*, 1986; **?**; *Qi et al.*, 2013). Most of the melt occupies triple junctions and grain boundaries of olivine, with no MPO. The distribution of melt viewed in a transverse section of a hot-pressed sample in Figure 4.2 is largely homogeneously.

4.3.2 Melt viscosity

Melt viscosities were calculated based on electron microprobe analyses of quenched melt pockets in hot-pressed samples, as summarized in Table 4.1. The viscosities of alkali basalt and albite melt were calculated using a silicate melt viscosity calculator (*Giordano et al.*, 2008). Since Li_2O is not included in this viscosity calculator, the viscosity of Li-silicate was estimated from the model by *Shaw* (1972). These three systems cover 4 orders of magnitude in melt viscosity, yielding a factor of 100 range in compaction length.

The presence of FeO and MgO in the albite and Li-silicate and the low FeO content in alkali basalt in Table 4.1, indicate that all three melts reacted with olivine. Although samples with Li-silicate melt were fabricated using the method of *Renner et al.* (2003), the SiO_2 content in the Li-silicate melt is higher in our samples (73.3 vs. 67.5 wt.%).

Table 4.1: Melt compositions and calculated viscosities

composition of glass (wt.%)	albite	alkali basalt	Li-silicate
SiO_2	70.5±2.3	49.5±0.4	73.3±1.9
TiO_2		2.9±0.03	
Al_2O_3	20.7±1.2	18.2±0.2	0.5±0.003
FeO	1.3±0.5	6.5±0.2	9.3±1.0
MgO	2.0±0.2	5.5±0.4	8.7±1.9
CaO	0.7±0.1	12.4±0.2	1.1±0.2
Li_2O			6.6±0.9
Na_2O	6.4±0.3	3.6±0.06	
K_2O		1.0±0.03	
melt viscosity at 1473 K (Pa·s)	3.5×10^4	1.6×10^2	3

Note: The weight percentage of Li_2O was calculated by difference.

Table 4.2: Experiments summary

Sample #	Composition	$\gamma(R)$	t_{total} (10^4·s)	$\dot{\varepsilon}_{eq}$ (10^{-4}·s^{-1})	σ_{eq} (MPa)	$\bar{\phi}$ (%)	ϕ_{max}/ϕ_{min}
PI0767	ol + alkali basalt	11.1	2.80	2.29	187	-	1.6
PI0811	ol + alkali basalt	5.6	1.76	1.84	237	3.3	1.2
PI0812	ol + alkali basalt	5.8	1.82	1.84	163	4.6	1.4
PI0817	ol + alkali basalt	5.0	1.23	2.35	197	3.3	1.3
PI0839	ol + alkali basalt	7.3	2.29	1.84	237	3.7	1.7
PI0858	ol + alkali basalt	2.1	2.09	0.58	229	3.2	1.4
PI0862	ol + albite	5.4	1.48	2.10	238	5.6	1.5
PI0867	ol + albite	11.3	2.82	2.31	183	4.9	2.2
PI0891	ol + alkali basalt	14.3	4.05	2.04	179	4.0	2.0
PI0895	ol + albite	3.2	2.89	0.64	259	6.1	-
PI0909	ol + Li-silicate	4.9	1.30	2.18	148	3.9	2.2

Note1: $\gamma(R)$ is shear strain at the outer radius. t_{total} is the time spent for an experiment. $\dot{\varepsilon}_{eq}$ is equivalent strain rate. σ_{eq} is equivalent stress. $\bar{\phi}$ is the average melt fraction of the observed section. ϕ_{max}/ϕ_{min} is the ratio of maximum over minimum melt fraction.
Note2: The average melt fraction of sample PI0767 was not obtained.
Note3: No base-state melt segregation was observed in sample PI0895.

4.3.3 Strain series: alkali basalt

In this subsection, two aspects of the melt distribution in olivine + alkali basalt samples deformed in torsion to outer-radius shear strains of $2.1 \leqslant \gamma \leqslant 14.3$ are described: (1) MPO in tangential sections, which corresponds to step (*i*) in the process of base-state melt segregation, and (2) melt distribution in transverse sections, which corresponds to step (*iv*) in the process of base-state melt segregation. The conditions of each experiment are summarized in Table 4.2.

The rose diagrams in Figure 4.3 demonstrate that melt pockets align at 37° to 40° to the shear plane, antithetic to shear direction, at low ($\gamma = 2.5$) and medium ($\gamma = 5.3$) strains. At a high strain ($\gamma = 8.5$), the observed MPO rotates to 28° to the shear plane, antithetic to shear direction. In all samples illustrated, the existence of a strong MPO is well established.

As illustrated in Figure 4.4, the melt fraction is higher close to the axial center than close to the outer edge of a sample deformed in torsion, providing strong evidence for the base-state segregation. Close to the axial center, large melt pockets are roughly homogeneously distributed. Close to the edge, a melt-enriched band contains significantly more melt than the neighboring melt-depleted region. Moreover, melt pockets in the micrograph close to the edge are much smaller than those close to the center. The decrease in the size of melt pocket with increasing radius reflects a decrease in grain size with increasing radius, associated with the increase in shear stress with increasing radius.

In Figure 4.5, the color maps of melt distribution in transverse sections demonstrate a higher melt fraction in the axial center than on the outer edge, which is the result of base-state melt segregation. In Figure 4.5(a), at a strain of $\gamma = 2.1$, base-state melt segregation is obvious, but no melt-enriched bands are observed. In samples deformed to a strain of $\gamma \geqslant 5.0$, melt-enriched bands are apparent. As strain increases, the azimuthal distribution of melt-enriched bands in the transverse section evolves from roughly homogeneous (e.g., $\gamma = 5.0$ in Figure 4.5(b)) to very inhomogeneous (e.g., $\gamma = 11.1$ in Figure 4.5(f)). At the largest strains ($\gamma = 11.1$ and $\gamma = 14.3$ in Figure 4.5(f) and (g)), the azimuthal distribution of melt-enriched bands is dominated by several extraordinarily large bands. Bands nucleate at the outer radius of the samples, and, as they propagate toward the

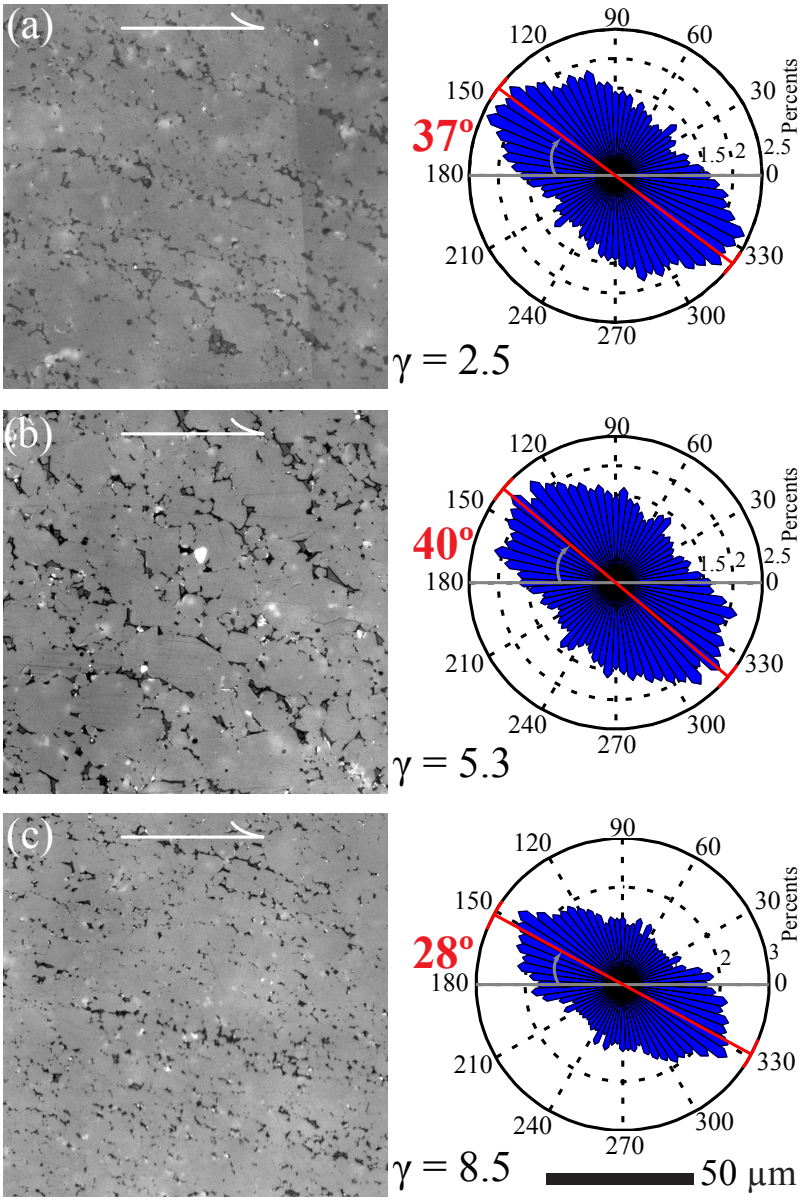

Figure 4.3: MPO in olivine + alkali basalt samples deformed to three different shear strains. In each panel, a reflected-light, optical micrograph from a tangential section is on the left and a rose diagram generated from optical micrographs of this tangential section is on the right. In the micrographs, olivine grains are light gray, melt is dark gray, and internal reflections or residual polishing material are white. The sense of shear is marked by the arrow on top. Each rose diagram was constructed from more than 1000 melt pockets with areas larger than 2 μm^2. The shear strain of each tangential section is displayed at the bottom of each panel. These tangential sections were taken at $r \lesssim R$.

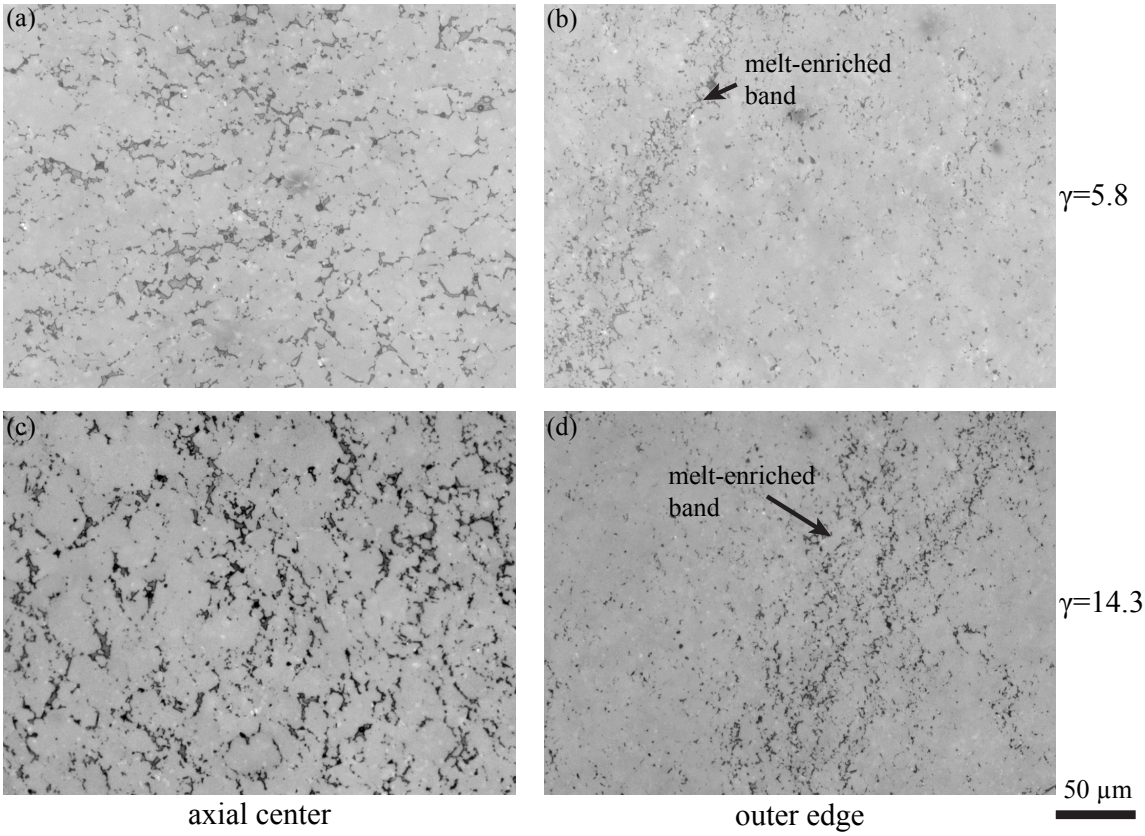

Figure 4.4: Reflected-light, optical micrographs of areas close to the axial center and close to the outer edge of transverse sections from two olivine + alkali basalt samples. (a) and (b) are from areas close to center and close to edge, respectively, of a sample deformed to a shear strain of $\gamma = 5.8$ (PI0812). (c) and (d) are from areas close to center and close to edge, respectively, of a sample deformed to a shear strain of $\gamma = 14.3$ (PI0891). Melt-enriched bands are noted by arrows in (b) and (d).

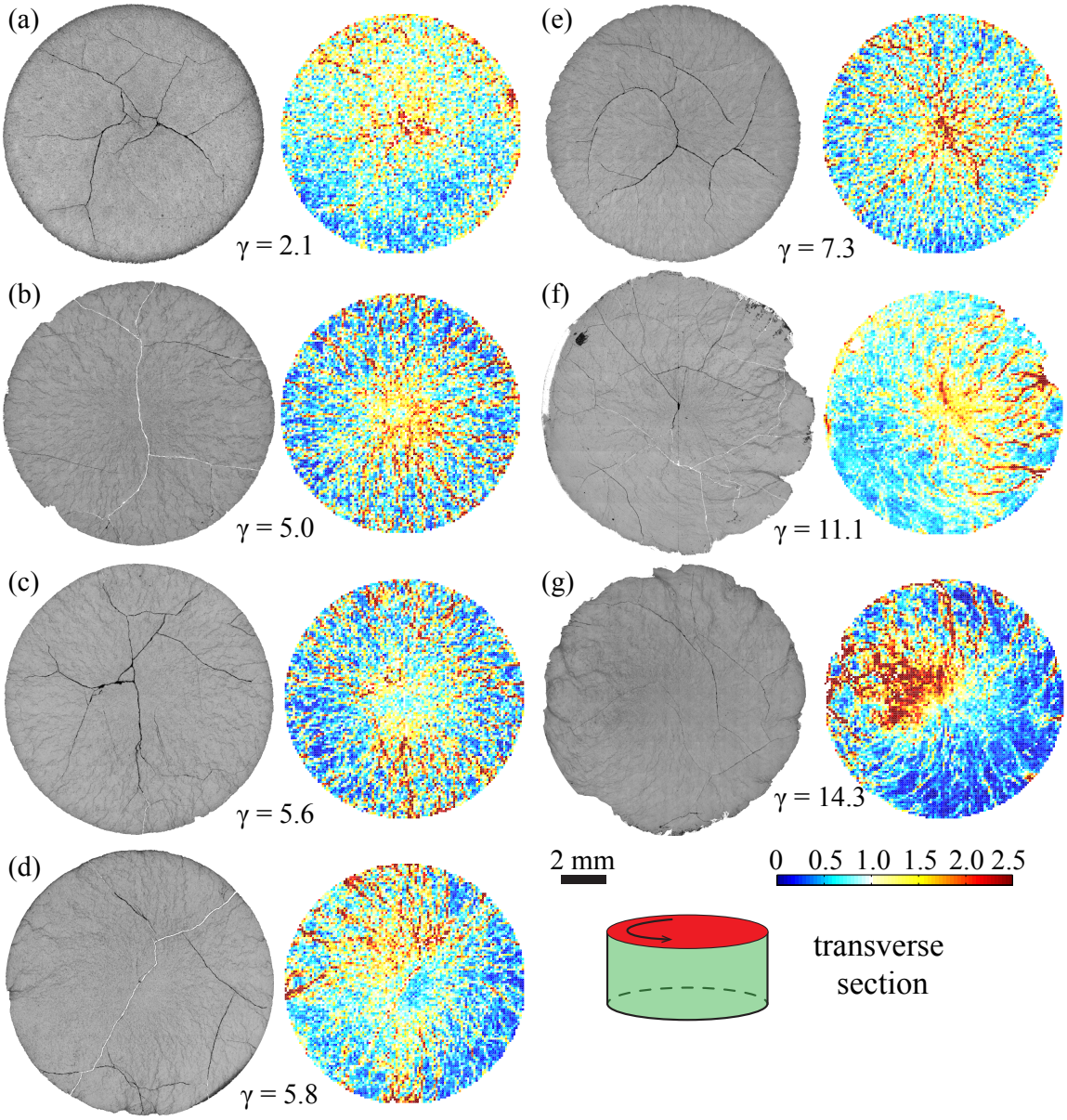

Figure 4.5: Melt distribution in transverse sections of seven olivine + alkali basalt samples deformed to outer-radius shear strains of $2.1 \leqslant \gamma \leqslant 14.3$. In each panel, a reflected-light, optical micrograph of the entire transverse section is on the left, with olivine in light gray and melt in dark gray; and the corresponding color map of melt distribution is on the right with a grid size of 100×100 μm. Shear strain at the outer radius increases from 2.1 in (a) to 14.3 in (g). Color bar indicates melt fraction normalized by the average value in each map. The sketch at bottom-right is a deformed cylindrical sample with its transverse section marked in red.

center, bands converge. The bands terminate at a radius corresponding to $\gamma \approx 1$, consistent with previous study (*King et al.*, 2010). It is notable that the color maps in Figure 4.5 are generated from low-resolution (1 pixel = 1.29 μm) optical micrographs, which produce an incorrectly high melt fraction in melt-enriched bands due to artifacts in image processing (in Chapter 3).

As illustrated in Figure 4.6 in a plot of melt fraction versus sample radius, base-state melt segregation occurs in all of our deformed samples of olivine + alkali basalt.. The radial distribution of melt evolves with shear strain: as strain increases, the peak of melt fraction generally increases, and the position of the peak propagates inward. We note that the profiles of melt fraction as a function of radius are calculated from higher resolution (1 pixel = 0.32 μm) optical micrographs, a significant advance over our earlier study in Chapter 3.

4.3.4 Strain series: albite

Similarly to the experiments described in the previous subsection, two important features of olivine + albite samples deformed to outer-radius shear strains of $3.2 \leqslant \gamma \leqslant 11.3$ are described: (1) MPO in tangential sections and (2) melt distribution in transverse sections. The conditions of each experiment are summarized in Table 4.2.

As illustrated in the optical micrographs and rose diagrams of Figure 4.7, a preferred alignment of melt is observed in deformed olivine + albite samples. The MPO is $\sim 38^\circ$ to the shear plane, antithetic to the shear direction, at a shear strain of $\gamma = 5.1$, and rotates to $\sim 30^\circ$ at a shear strain of $\gamma = 10.2$.

Figure 4.8 reveals the disparity in melt fraction between areas close to the axial center and close to the outer edge in the transverse section of samples deformed to different shear strains. Close to the center, large melt pockets are roughly homogeneously distributed. At a shear strain of $\gamma = 5.4$, in the micrograph close to the edge, small melt pockets align. While at a shear strain of $\gamma = 11.3$, melt-enriched bands form close to the edge. Compared to olivine + alkali basalt samples, melt-enriched bands in olivine + albite samples first appear at a higher shear strain, which suggests a slower rate of stress-driven melt segregation and band formation in the olivine + albite samples.

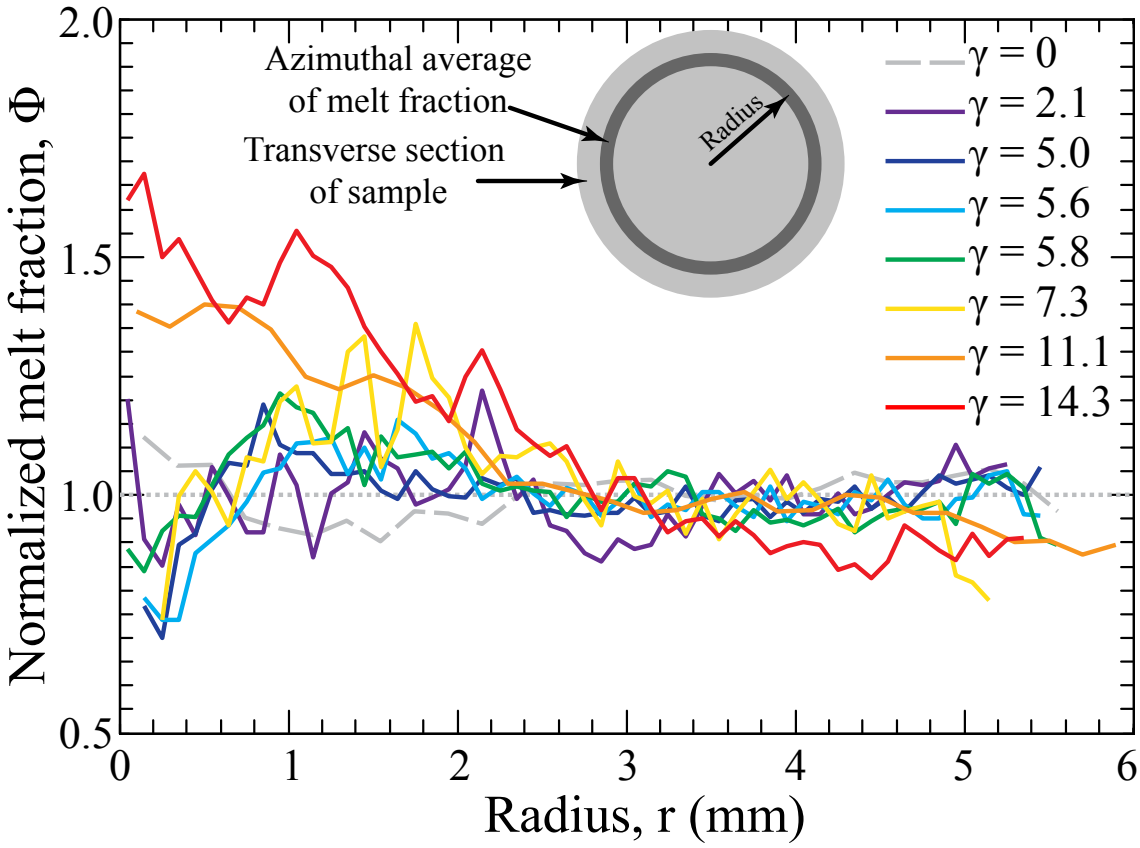

Figure 4.6: Plot of azimuthally averaged, normalized melt fraction versus radius for starting material and seven deformed samples made from olivine + alkali basalt. In the legend, the outer-radius strain of each sample is noted. Melt fraction is normalized to the average for the whole transverse section of each sample. The gray dotted line corresponds to a normalized melt fraction of 1.0. The sketch shows how an azimuthal average of melt fraction is obtained for a given radius.

The melt distribution resulting from base-state melt segregation is displayed by color maps in Figure 4.9. At a shear strain of $\gamma \leqslant 5.4$, only a few melt-enriched bands are formed. As shear strain increases to $\gamma = 11.3$, melt-enriched bands are widely observed. Melt fraction increases from the outer edge toward the axial center of a transverse section in two samples deformed to a shear strain of $\gamma \geqslant 5.4$. As shear strain increases, the contrast in melt fraction between the axial center and the outer edge becomes higher.

In Figure 4.10, profiles of azimuthally averaged melt fraction versus radius reveal the redistribution due to base-state melt segregation. Any radial segregation of melt is below the resolution of our measurements for the sample deformed to a shear strain of $\gamma = 3.2$. However, base-state melt segregation is clearly observed in olivine + albite samples deformed to shear strains of $\gamma = 5.4$ and $\gamma = 11.3$.

4.3.5 Melt composition series

In this subsection, observations from the olivine + Li-silicate sample (PI0909) is introduced in the first paragraph. Then, in the following paragraph, base-state melt segregation in samples with melts of different compositions, all deformed to similar shear strains, are compared.

Micrographs taken close to the axial center and close to the outer edge of the olivine + Li-silicate sample in Figure 4.11 illustrate the variations in melt fraction. As a consequence of the low-viscosity of this melt, many melt pockets including the neighbouring olivine grains are plucked out during polishing (in Figure 4.11(a)). Comparing the number of melt pockets in Figure 4.11(a) and (b), it is clear that more melt exists in the center than the close to the edge.

Three samples, on of each melt composition, all deformed to similar shear strains of $\gamma \approx 5.0$ (PI0817, PI0862 and PI0909) at similar equivalent strain rates of $\dot{\varepsilon}_{eq} \approx 2\times10^{-4}$, exhibit different levels of band formation and base-state melt segregation. As illustrated in Figure 4.12, among the three samples, the distribution of melt in the olivine + albite sample is the most homogeneous, while that in the olivine + Li-silicate sample is the most heterogeneous. In Figure 4.12(a), many melt-enriched bands in the sample with albite melt exist at large radius, but their contrast with the

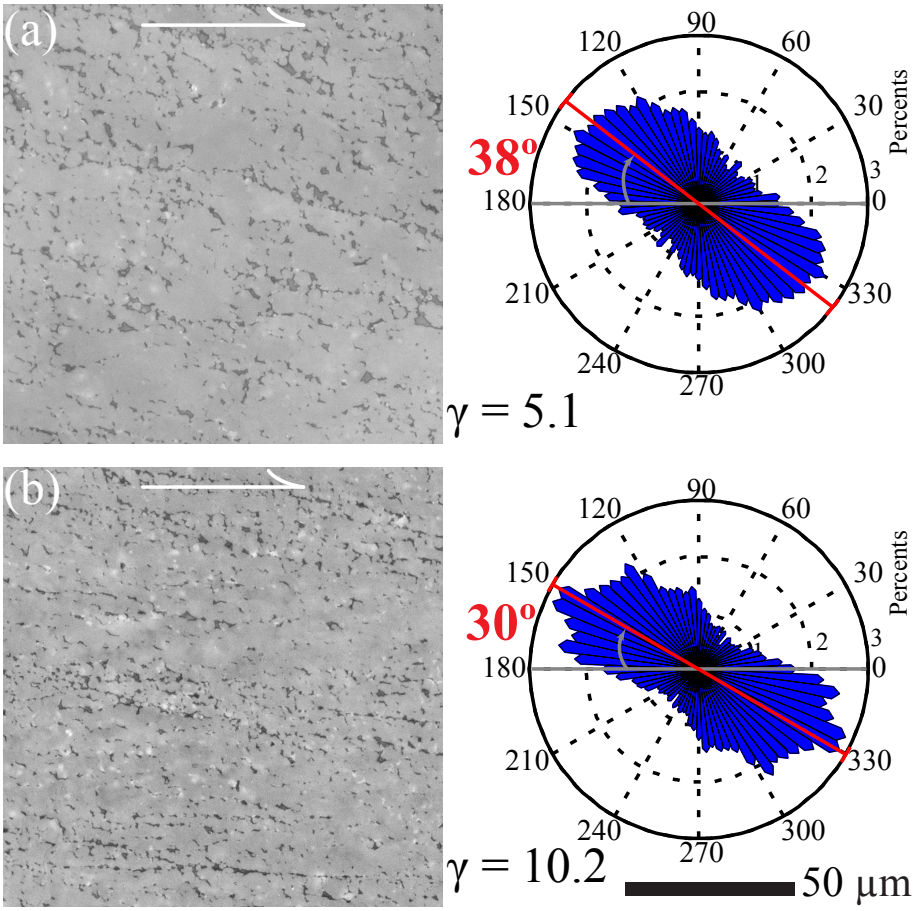

Figure 4.7: MPO in two olivine + albite samples deformed to different shear strains. In each panel, a reflected-light, optical micrograph from a tangential section is on the left and a rose diagram generated from optical micrographs of this tangential section is on the right. In the micrographs, olivine grains are light gray, melt is dark gray, and internal reflections or residual polishing material are white. The sense of shear is marked by the arrow on top. Each rose diagram was constructed from more than 1000 melt pockets with areas larger than 2 μm^2. The shear strain of each tangential section is displayed at the bottom of each panel.

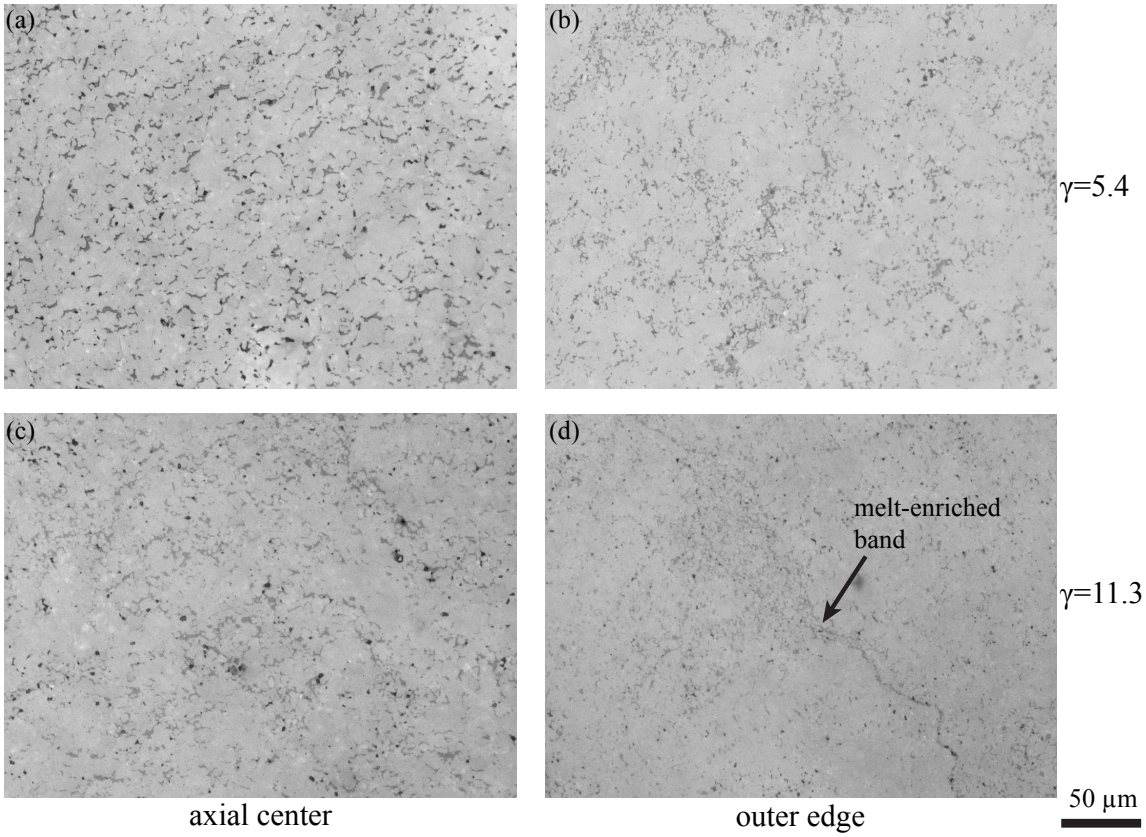

Figure 4.8: Reflected-light, optical micrographs of areas close to the axial center and close to the outer edge of transverse sections from two olivine + albite samples. (a) and (b) are from areas close to center and close to edge, respectively, of a sample deformed to a shear strain of $\gamma = 5.4$ (PI0862). (c) and (d) are from areas close to center and close to edge, respectively, of a sample deformed to a shear strain of $\gamma = 11.3$ (PI0867). A melt-enriched band is noted in (d).

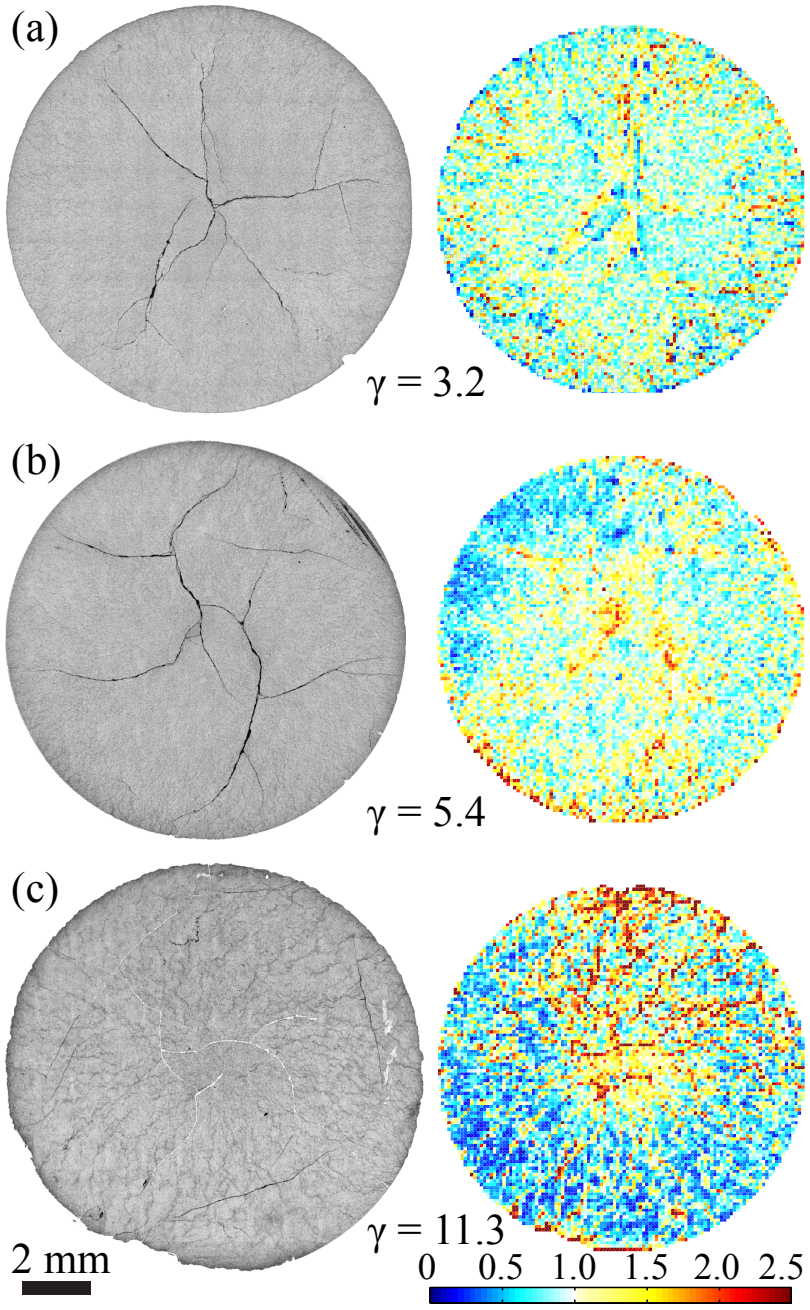

Figure 4.9: Melt distribution in transverse sections of three olivine + albite samples deformed to an outer-radius shear strain of $3.2 \leqslant \gamma \leqslant 11.3$. In each panel, a reflected-light, optical micrograph of the entire transverse section is on the left, with olivine in light gray and melt in dark gray. The corresponding color map of melt distribution is on the right with a grid size of 100×100 μm. Color bar indicates melt fraction normalized by the average value in each map.

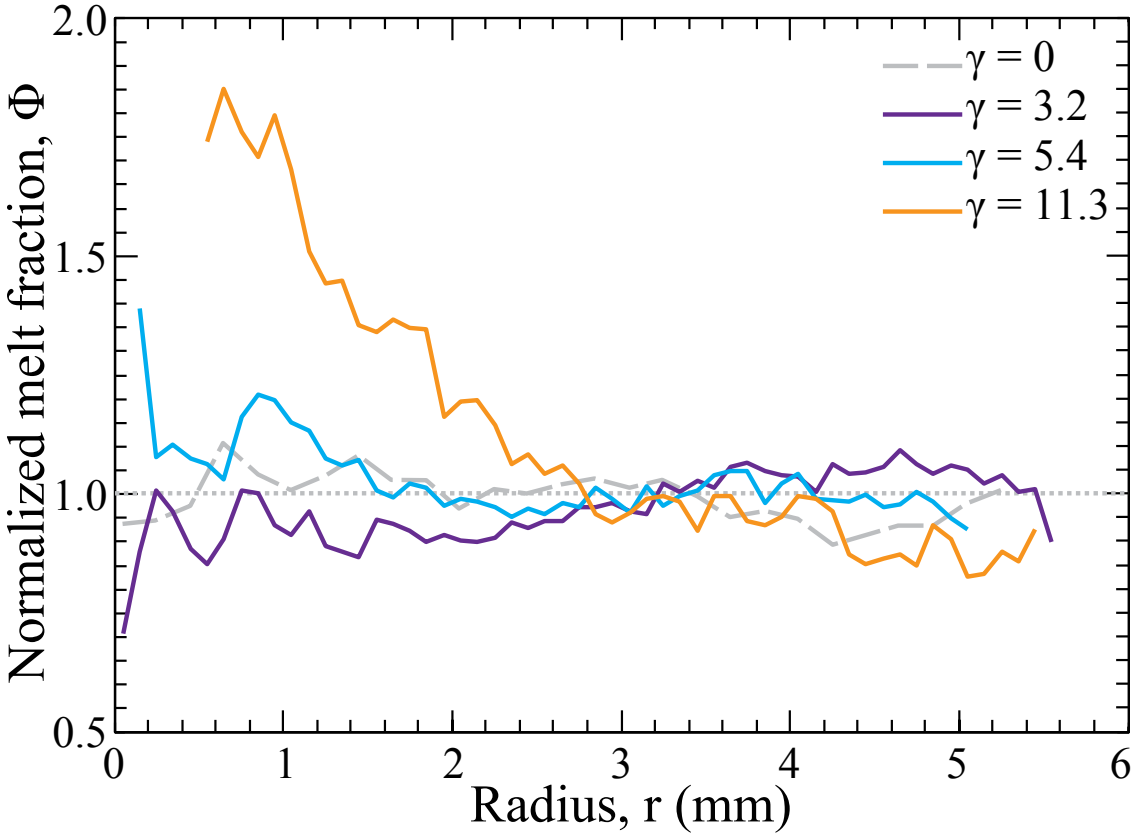

Figure 4.10: Plot of azimuthally averaged, normalized melt fraction versus radius for starting material and three deformed samples of olivine + albite. In the legend, the outer-radius strain of each sample is noted. Melt fraction is normalized to the average for the whole transverse section of each sample. The gray dotted line corresponds to a normalized melt fraction of 1.0.

background is low. In Figure 4.12(b), the azimuthally uniformly distributed bands in the sample with alkali basalt extend very close to the center, while the band-to-non-band contrast in melt fraction is high. In Figure 4.12(c), the melt structure in the sample with a Li-rich melt is dominated by several extraordinary melt-enriched bands with high melt fraction. The color maps in Figure 4.12 demonstrate that base-state melt segregation occurs in all three samples. Quantitative comparisons are given as radial distribution profiles of melt fraction in Figure 4.13. Despite the large differences in melt composition, the profiles of melt distribution for olivine + alkali basalt and olivine + albite samples are quite similar in that the peak in melt fraction occurs at the same radius and the maximum melt fractions are similar. The melt distribution of olivine + Li-silicate sample exhibits much stronger melt segregation than the other two samples with a higher maximum melt fraction at smaller radius.

4.4 Discussion

Our experimental results demonstrate that base-state melt segregation occurs during torsional deformation of partially molten rocks, as predicted by two-phase flow theory incorporating viscous anisotropy. The resulting melt distribution evolves with increasing strain and is influenced by melt composition, which directly affects compaction length. Comparisons between samples of the same composition but deformed to different shear strains provide an estimate of the compaction rate in base-state melt segregation, which reflects the evolution of melt distribution with strain. According to *Takei and Katz* (2013), compaction rate depends most strongly on the normalized compaction length, δ_c/H. In order to calculate the compaction rate and compaction length for each sample, several approximations are made in this section: (1) by assuming that sample viscosity, grain size and permeability are independent of radius and time, compaction length becomes a constant in each sample; (2) by assuming that compaction rate does not change with time, compaction rate becomes a function of radius; (3) the influence of increasing strain on the magnitude of viscous anisotropy is neglected. Thus, we determined the influence of compaction length on compaction rate in base-state melt segregation in torsional deformation in order to compare our results with

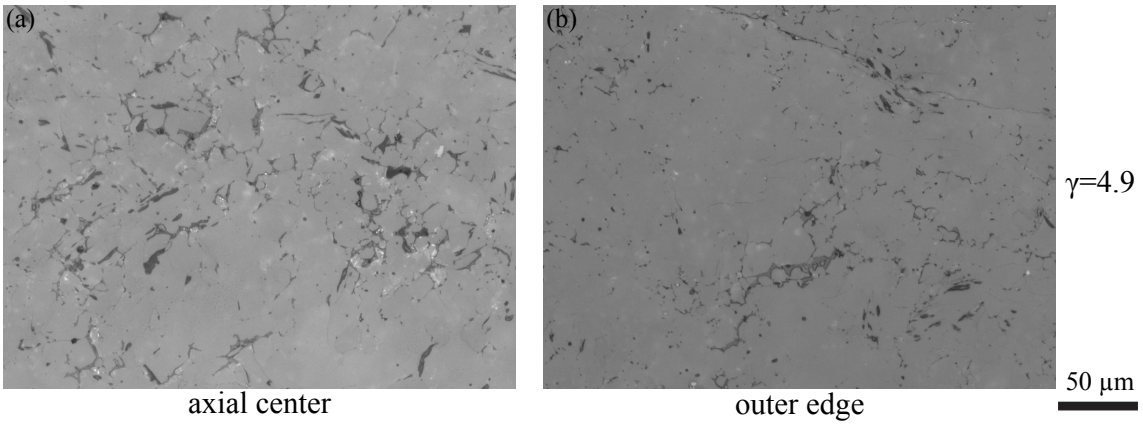

Figure 4.11: Reflected-light, optical micrographs of areas (a) close to the axial center and (b) close to the outer edge of the transverse section from olivine + Li-silicate sample (PI0909). Olivine is light gray, melt is dark gray, and pluck-outs introduced during polishing are black.

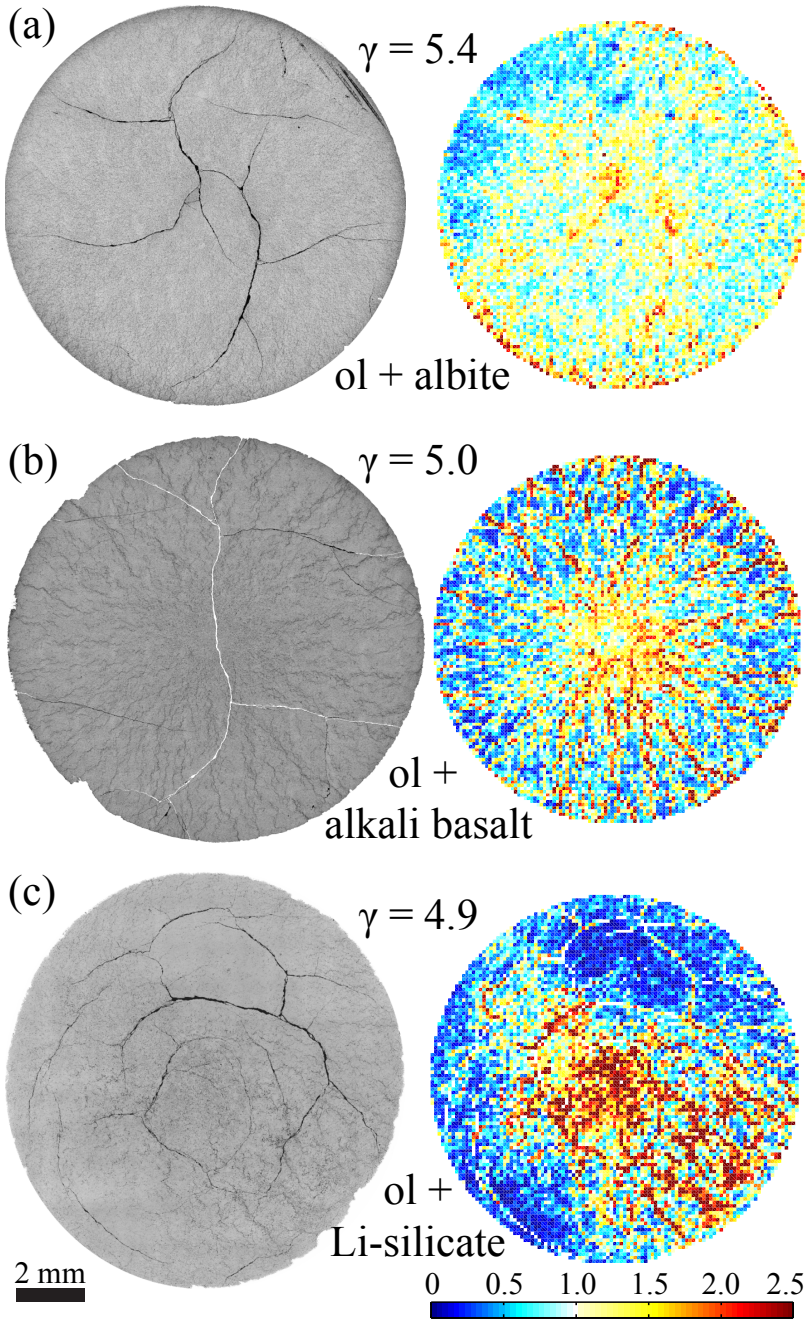

Figure 4.12: Melt distribution in transverse sections of three samples deformed to similar shear strains but with different melt compositions. In each panel, a reflected-light, optical micrograph of the entire transverse section is on the left, with olivine in light gray and melt in dark gray, and the corresponding color map of melt distribution is on the right, with a grid size of 100×100 μm. Color bar indicates melt fraction normalized by the average value in each map. (a) Olivine + albite sample deformed to $\gamma = 5.4$ (PI0862). (b) Olivine + alkali basalt sample deformed to $\gamma = 5.0$ (PI0817). (c) Olivine + Li-silicate sample deformed to $\gamma = 4.9$ (PI0909).

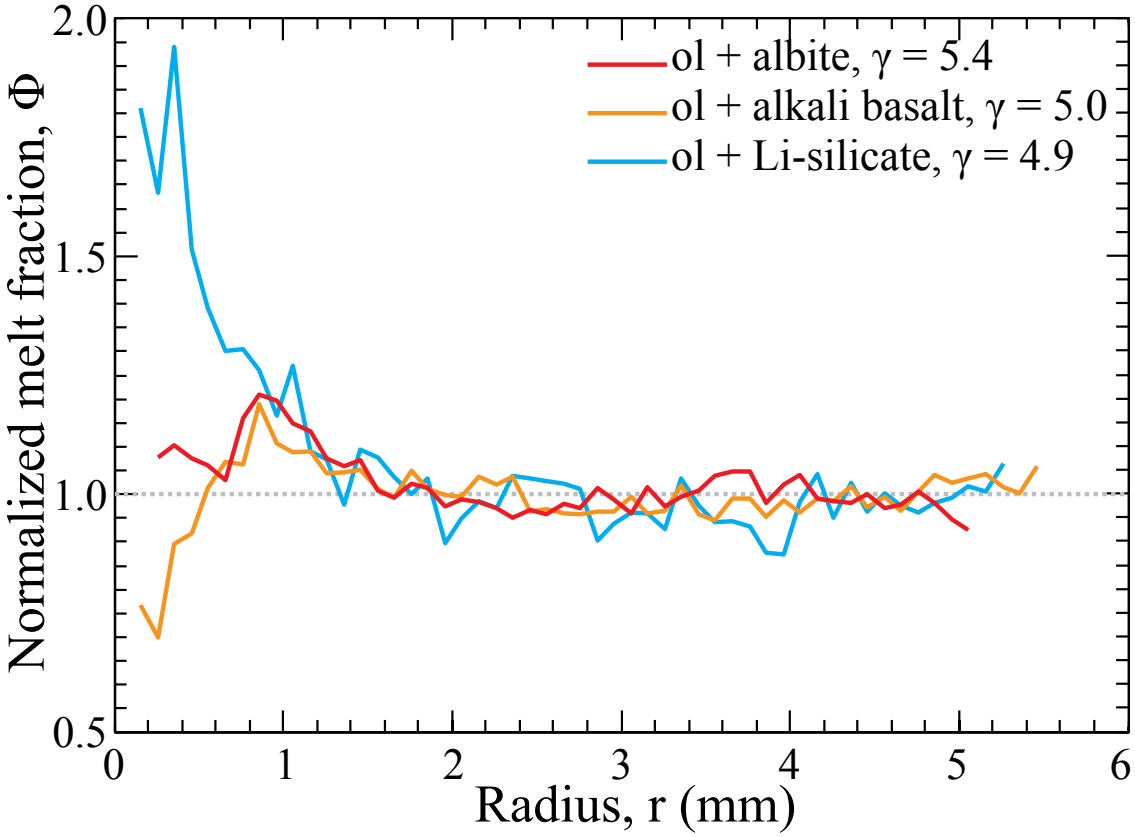

Figure 4.13: Plot of azimuthally averaged, normalized melt fraction versus radius for three samples deformed to similar shear strains but with different melt compositions. The outer-radius shear strain is 5.4 for olivine + albite sample (PI0862), 5.0 for olivine + alkali basalt sample (PI0817), and 4.9 for olivine + Li-silicate sample (PI0909). Melt fraction is normalized to the average for the whole transverse section of each sample. The gray dotted line corresponds to a normalized melt fraction of 1.0.

predictions of the model.

4.4.1 MPO: observation vs. assumption

To calculate the angle of viscous anisotropy in two-phase flow theory under simple shear condition, σ_3 is taken to be at 45° to the shear plane, synthetic to shear direction, and melt is assumed to align perpendicular to σ_3, as suggested by experiments on an analogue material (*Takei*, 2010). Thus, an assumption is made that the MPO is 45° to the shear plane, antithetic to shear direction (*Takei and Katz*, 2013). In olivine + alkali basalt samples deformed to shear strains of $\gamma \leqslant 5.3$ (Figure 4.3(a) and (b)) and olivine + albite samples deformed to a shear strain of $\gamma = 5.1$ (Figure 4.7(a)), the observed MPO is 5-8° away from the assumed value, indicating reasonable consistency between hypothesis and observation. Divergence between assumption and observation occurs at higher shear strain (Figure 4.3(c) and 4.7(b)), that is, the angle of MPO rotates to 28-30° to the shear plane, antithetic to shear direction. This change in MPO indicates either that melt no longer lies normal to σ_3 at large strain or that the stress field rotates with increasing strain. The observed decrease in the angle of the MPO with increasing strain in samples with either alkali basalt or albite has yet to be incorporated into the models of melt segregation during shear deformation.

4.4.2 Grain size and its effects

In our torsion experiments, dynamic recrystallization results in a grain size reduction. As a result, the grain size decreases from the axial center to the outer edge of a torsion sample, due to the increase of shear stress with increasing radius. This grain size distribution can be qualitatively inferred by comparing the size of melt pockets close to the outer edge with those close to the axial center (Figure 4.4 and 4.8). A quantitative comparison can be obtained from the electron-backscattered diffraction (EBSD) maps, such as those in Figure 4.14 for a sample of olivine + alkali basalt deformed to $\gamma = 11.1$, which revealed a larger grain size ($\sim$6 μm) in the center than at the edge ($\sim$3 μm).

In a two-phase aggregate consisting of coarse- and fine-grained domains, as a consequence

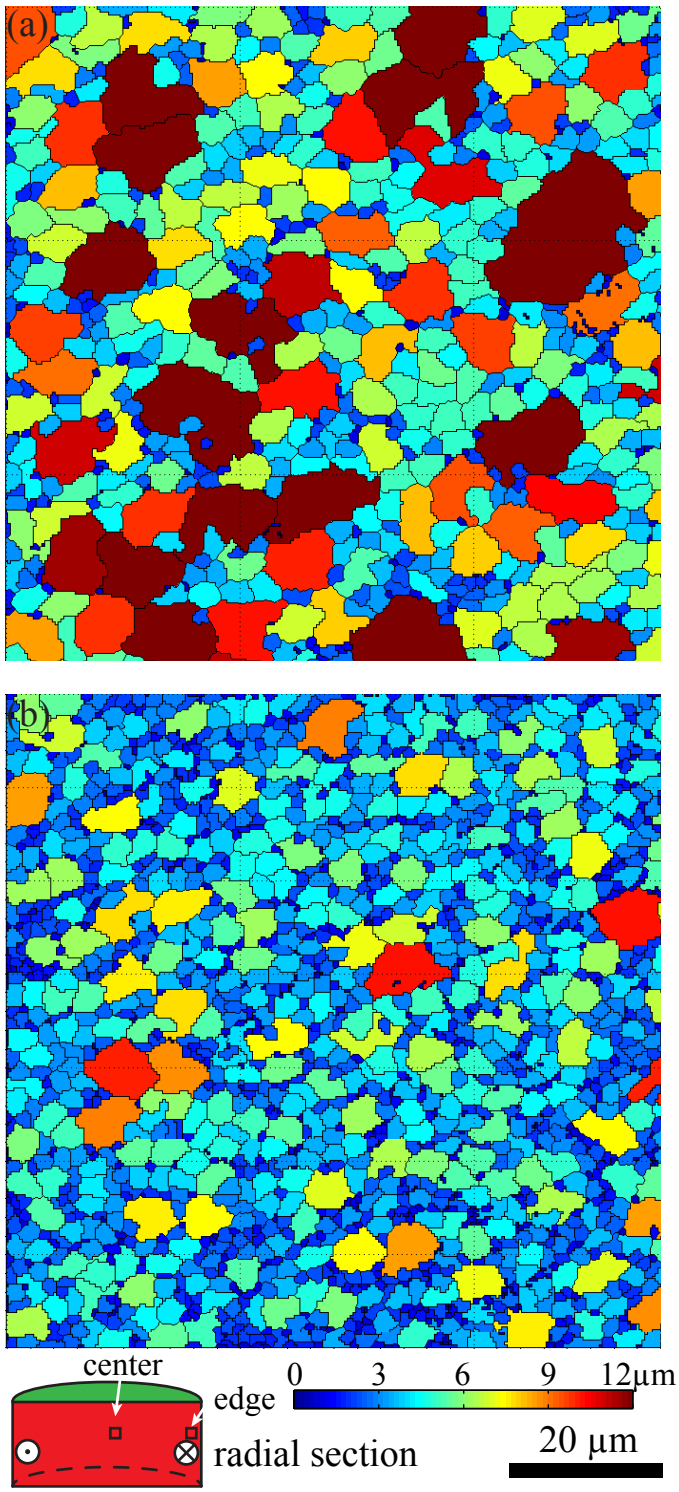

Figure 4.14: EBSD maps from a radial section of an olivine + alkali basalt sample deformed to $\gamma = 11.1$. The sketch at the bottom of the figure illustrates the locations at which data were collected for the center section (a) and the edge section (b). Step size is 0.6 μm. Map is colored by grain size, as illustrated in the color bar (unit is μm). Indexing rate for both maps is above 90 %. Un-indexed points, representing melt, are eliminated by a noise reduction process. The map is processed using a MTEX toolbox in MATLAB (**?**). The sense of shear is into and out of the surface of the paper as indicated in the sketch.

of the balance of interfacial energy, the equalization of melt-grain boundary curvature across the system results in a larger melt fraction in the fine-grained domain (*Wark and Watson*, 2000). Since grain size is smaller at large radius than at small radius in torsion samples, the gradient in interfacial energy drives melt toward the edge, that is, in the opposite direction of base-state melt segregation. Here this pressure gradient induced by interfacial energy is estimated for samples of olivine + alkali basalt. According to Young–Laplace equation, the relationship between boundary curvature and pressure is expressed as

$$\Delta P_L = 2\gamma_s \kappa, \tag{4.2}$$

where γ_s is interfacial energy and κ is the curvature of the interface. The Laplace pressure ΔP_L is pressure difference between the inside and the outside of the curved surface (*Butt et al.*, 2006), that is, $\Delta P_L = P^{solid} - P^{liquid}$ in this study. For an olivine + basalt aggregate, the interfacial energy between liquid and solid phases $\gamma_{SL} = 0.50 \pm 0.20$ J/m^2 (*Cooper and Kohlstedt*, 1982). The curvature of the interface is related to melt fraction and the liquid-solid dihedral angle, θ, as (*Raj*, 1981)

$$\phi = \frac{8}{\pi d^2 \kappa^2} \left[2\cos^2\theta \sin\frac{\pi}{3} - \frac{\pi}{2} + 3(\theta - \frac{\sin 2\theta}{2}) \right]. \tag{4.3}$$

Given that $\theta \approx 29^\circ$ in olivine + basalt aggregates (*Holness*, 2006), Eq. 4.3 is simplified as

$$\phi \approx \frac{0.004}{\pi d^2 \kappa^2}. \tag{4.4}$$

Assuming $\phi = \bar{\phi}_0 = 0.07$, independent of radius, at the outer radius, $d_{outer} \approx 3$ μm results in $\kappa_{outer} \approx 4{\times}10^4$ m^{-1}, and at the axial center, $d_{center} \approx 6$ μm results in $\kappa_{center} \approx 2{\times}10^4$ m^{-1}. Thus, the pressure gradient, $\nabla P^l_{\gamma_{SL}}$, is calculated as

$$\nabla P^l_{\gamma_{SL}} = \frac{P^l_{outer} - P^l_{center}}{R} = \frac{-\Delta P_{L,outer} + \Delta P_{L,center}}{R} = \frac{2\gamma_{SL}(\kappa_{center} - \kappa_{outer})}{R}, \tag{4.5}$$

where R is the radius of the sample, $R \approx 6$ mm. Using the values discussed previously, the pressure gradient resulting from interfacial energy is estimated as

$$\nabla P^l_{\gamma_{SL}} = \frac{2\gamma_{SL}(\kappa_{center} - \kappa_{outer})}{R} \approx -3 \text{ MPa/m}. \tag{4.6}$$

To understand the influence of $\nabla P^l_{\gamma_{SL}}$, a comparison with the pressure gradient in base-state melt segregation caused by stress, ∇P^l_σ, is necessary. It is very difficult to quantify ∇P^l_σ from two-phase flow theory. However, ∇P^l_σ can be estimated as

$$\nabla P^l_\sigma = \frac{\partial P^l}{\partial r} \approx \frac{|\sigma_1| - |\sigma_3|}{R}, \tag{4.7}$$

which is on the an order of 100 MPa/m. Although, compared with the driving force that leads to base-state melt segregation, the driving force caused by the balance of interfacial energy is small, this counteracting driving force may contribute to two issues. First, in the profiles of melt fraction in Figure 4.6, 4.10 and 4.13, the absence of the decrease in melt faction at the outer radius that is predicted by stimulations (Chapter 3) may be a consequence of this outward flow of melt. Second, the concentration of melt at large radius in the olivine + albite sample deformed to a shear strain of $\gamma = 3.2$ (PI0895) could be an evidence that the driving force induced by interfacial energy overcomes the pressure gradient in base-state melt segregation. Therefore, incorporating this driving force for melt migration in the model with viscous anisotropy may reconcile the simulation results with the experimental observations.

4.4.3 Compaction length

To calculate compaction length, each term in Eq. 4.1 is evaluated in this subsection. As elaborated in Eq. 4.1, compaction length is a function of bulk and shear viscosities of the matrix, permeability and melt viscosity. In this study, the compaction length for a sample is taken to be a constant, independent of time or radius. Therefore, every term that is used to determine the compaction length has to be a constant. The viscosity of each melt is calculated from melt compositions listed in Table 4.1. The calculation of bulk and shear viscosities and permeability is discussed in the following three paragraphs.

The shear viscosity of our partially molten samples is calculated from measured values of equivalent stress, σ_{eq}, and equivalent strain rate, $\dot{\varepsilon}_{eq}$, (Table 4.2) as follows:

$$\eta = \frac{\sigma_{eq}}{\dot{\varepsilon}_{eq}}. \tag{4.8}$$

In a sample deformed at constant strain rate, shear stress initially increases and then decreases with increasing strain, due to dynamic recrystallization, development of microstructural fabric and formation of melt-enriched bands (*Hansen et al.*, 2012; *Holtzman et al.*, 2003b). To minimize the influence of melt-enriched bands in our analysis, we used the maximum value of σ_{eq} to calculate η. The calculated values of shear viscosities for individual samples are listed in Table 4.3.

Bulk viscosity is obtained from theory, since values for ζ have not been well constrained experimentally (*Renner et al.*, 2003; *Qi et al.*, 2013). A two-scale homogenization model for a partially molten system yielded a expression for bulk viscosity of the form

$$\zeta = C_\zeta \eta \phi^{-1}, \tag{4.9}$$

where C_ζ is a constant (*Simpson et al.*, 2010). A contiguity model predicted quite a different form,

$$\zeta = 5/3\ \eta, \tag{4.10}$$

for $\phi > 0.01$ (*Takei and Holtzman*, 2009a,c). Since anisotropic viscosity is derived base on the contiguity model, we use Eq. 4.10 to compute bulk viscosity in this study.

The permeability of a two-phase system is expressed as (*Bear*, 1972)

$$k = \frac{\phi^r d^2}{C}, \tag{4.11}$$

where ϕ is melt fraction, d is grain size, and C is a constant that quantifies the tortuosity of the paths on which melt migrates. The melt fraction exponent, r, depends on the microstructure of the aggregate (*Bernabé et al.*, 2003). For an anisotropic medium, that is, the partially molten samples in this study, a permeability tensor is needed. A previous study on melt-enriched bands used $r = 3$ for melt migrating in the plane of melt-enriched sheets (bands in 2D), and $r = 2$ for melt migrating in tubes normal to the melt-enriched sheets or for the case that no sheets are formed (*Holtzman et al.*, 2003a). Base-state melt segregation requires the migration of melt toward the axial center of a sample. In samples without melt-enriched sheets, melt pathways are tubes, and thus a value of $r = 2$ is used. In samples with melt-enriched sheets, melt migrates toward the axial center along the sheets, and thus $r = 3$ is used. The geometry factor has a value of $C = 1000$ for $r = 2$ and

$C = 25$ for $r = 3$ (*Holtzman et al.*, 2003a). With r and C determined, let us focus on values of ϕ and d. As discussed in the previous subsection, grain size varies with radius in deformed samples. However, for our assumption that compaction length is independent of radius, the evolution of grain size is neglected, and the grain size is taken as that in the starting material ($d_{\text{basalt}} \approx 9$ μm, $d_{\text{albite}} \approx 7$ μm, and $d_{\text{Li-sil}} \approx 16$ μm). Moreover, the average melt fraction in the starting material is used ($\bar{\phi}_{\text{basalt}} = \bar{\phi}_{\text{albite}} = 0.07$, $\bar{\phi}_{\text{Li-sil}} = 0.10$). With these values for d and ϕ, the values calculated for k are listed in Table 4.3.

With Eq. 4.10 for ζ, the compaction length can be expressed as

$$\delta_c = \left[\frac{3\eta k}{\mu}\right]^{1/2}. \tag{4.12}$$

The calculated values for compaction length, normalized by the sample height, are listed in Table 4.3. For the range of melt composition in this study, compaction length covers a range of more than two orders of magnitude, and the normalized values for compaction length extends over three orders of magnitude.

4.4.4 Evolution of melt distribution with strain

The evolution of melt distribution with increasing strain due to base-state melt segregation includes (1) an inward movement of the location of the maximum melt fraction and (2) an increase in the ratio of maximum-to-minimum melt fraction (Figures 4.6 and 4.10). To explain the former, it was assumed that the magnitude of viscous anisotropy (α and β) due to MPO increases from 0 at $\gamma(r = 0) = 0$ to a maximum value with increasing strain. The maximum value is reached at a radius r' at which $\gamma(r') = 1$. For $r > r'$, viscous anisotropy maintains its maximum value (Chapter 3). For $r < r'$, the driving force for base-state melt segregation is relatively small, because viscous anisotropy is weak. Thus, melt fraction is maximum at a radius corresponding to $\gamma(r) \approx 1$. As outer radius strain increases, the region with weak viscous anisotropy shrinks, and the radius with the highest concentration of melt moves inward. To more completely elucidate this process, a study of the development of MPO with shear stress and strain is necessary.

Table 4.3: Calculation of normalized compaction length

Sample #	μ (Pa·s)	η (Pa·s)	k (m^2)	δ_c (m)	H (mm)	δ_c/H
PI0767	1.6×10^2	8.17×10^{11}	1×10^{-15}	3.9×10^{-3}	3.0	1
PI0811	1.6×10^2	1.29×10^{12}	1×10^{-15}	4.9×10^{-3}	2.6	2
PI0812	1.6×10^2	8.86×10^{11}	1×10^{-15}	4.1×10^{-3}	2.6	2
PI0817	1.6×10^2	8.38×10^{11}	1×10^{-15}	4.0×10^{-3}	3.1	1
PI0839	1.6×10^2	1.29×10^{12}	1×10^{-15}	4.9×10^{-3}	3.6	1
PI0858	1.6×10^2	3.95×10^{12}	4×10^{-16}	5.4×10^{-3}	3.0	2
PI0862	3.5×10^4	1.12×10^{12}	7×10^{-16}	2.6×10^{-4}	3.1	8×10^{-2}
PI0867	3.5×10^4	7.88×10^{11}	7×10^{-16}	2.2×10^{-4}	2.9	7×10^{-2}
PI0891	1.6×10^2	8.77×10^{11}	1×10^{-15}	4.1×10^{-3}	6.6	1
PI0895	3.5×10^4	4.05×10^{12}	2×10^{-16}	2.6×10^{-4}	12.9	2×10^{-2}
PI0909	3	6.83×10^{11}	1×10^{-14}	8.3×10^{-2}	3.5	2×10^{1}

Note: Due to the presence of very limited melt-enriched bands, permeability of PI0858 and PI0895 is $k = \phi^2 d^2/1000$. The permeability of all other samples is $k = \phi^3 d^2/25$

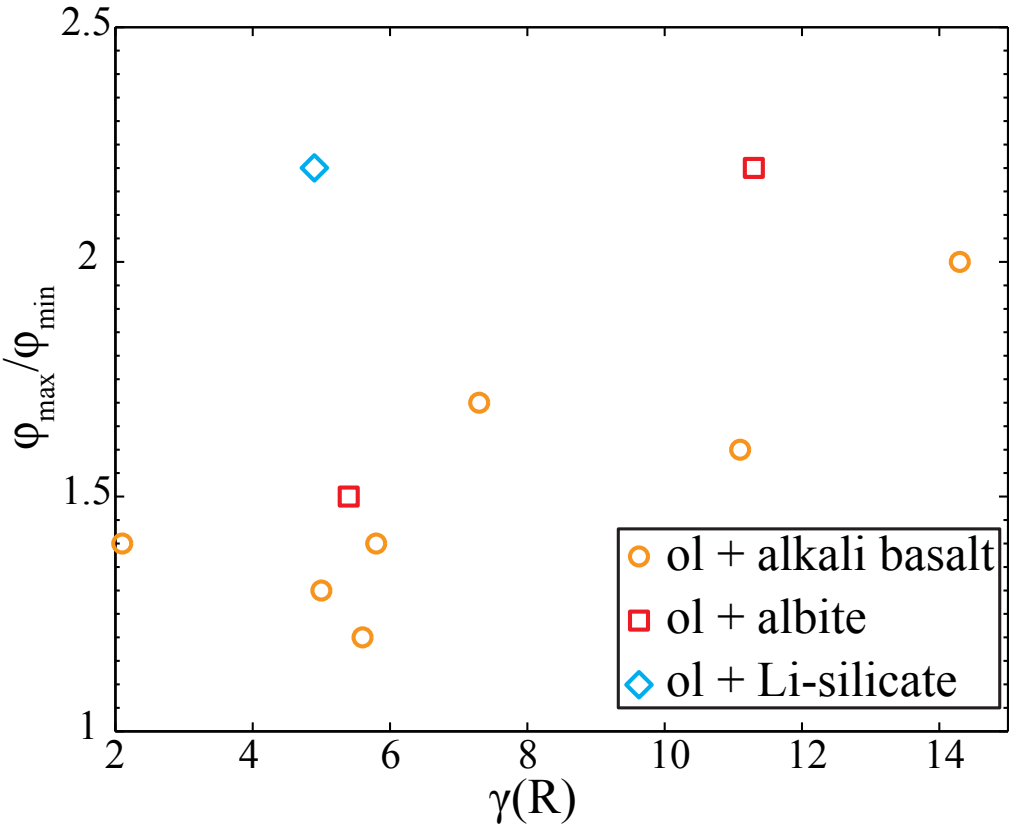

Figure 4.15: Plot of ϕ_{max}/ϕ_{min} versus outer-radius shear strain $\gamma(R)$. Sample PI0895 is not included in this plot because its radial melt distribution does not show base-state melt segregation.

The relationship between the ratio of maximum-to-minimum melt fraction, ϕ_{max}/ϕ_{min}, and outer-radius shear strain, $\gamma(R)$, is plotted in Figure 4.15. For olivine + alkali basalt and olivine + albite samples, ϕ_{max}/ϕ_{min} increases with increasing outer-radius shear strain. At the same outer-radius shear strain, ϕ_{max}/ϕ_{min} is larger for olivine + albite samples than for olivine + alkali basalt samples.

4.4.5 Calculation of compaction rate at given compaction length

Here, we present the procedure of calculating compaction rate for each sample and a description of a plot of compaction rate versus radius at a given compaction length. To calculate compaction rate, $\mathscr{C}$, an assumption is necessary that the compaction rate for a sample is a function of only radius, and is independent of time. Here, $\mathscr{C}(r)$ is calculated as

$$\mathscr{C}(r) = (1 - \Phi(r))/t_{total}, \tag{4.13}$$

where t_{total} is the total time spent in an experiment. $\Phi(r)$ is azimuthally averaged, normalized melt fraction, such that $\mathscr{C}(r)$ represents a normalized compaction rate (still referred as compaction rate for simplification). If $\mathscr{C}(r) < 0$, decompaction occurs, causing an increase in melt fraction, and vice versa. Figure 4.16(a) presents radial profiles of compaction rate for seven olivine + alkali basalt samples ($\delta_c/H = 1$ to 2) and their average. The lowest compaction rate (the highest decompaction rate), that is, the fastest accumulation rate of melt, occurs at $r \approx 1$ mm. The profiles for individual samples rest very close to each other at large radius, $r \geqslant 3$ mm, but diverge at small radius, $r \leqslant 2$ mm. Analogous to the radial distribution of melt, the location of the maximum in radial distribution of compaction rate moves inward as strain increases, as explained in the previous subsection. This change of peak position with strain in the profiles of compaction rate causes the divergence of the profiles at small radius.

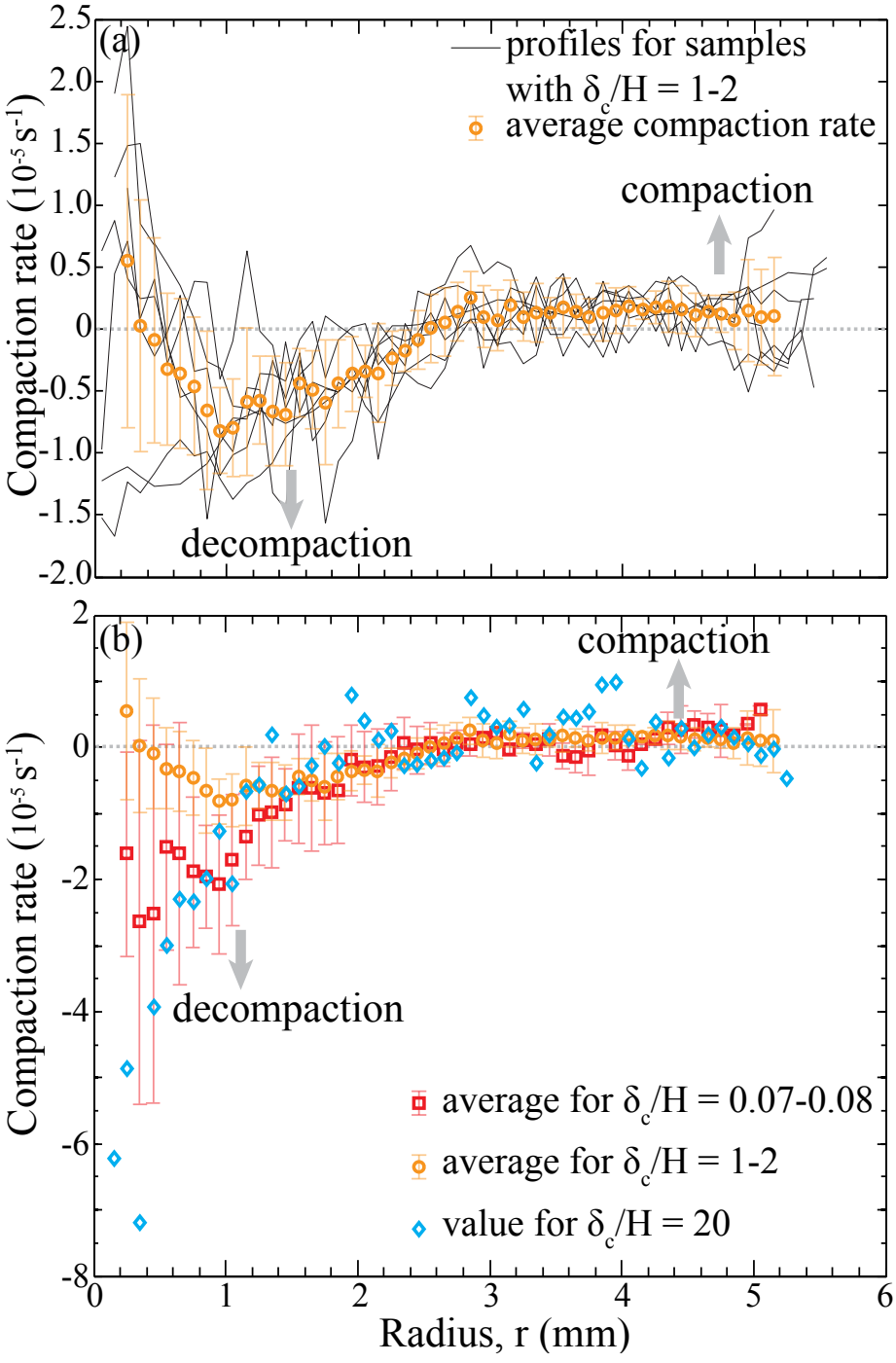

Figure 4.16: Plot of compaction rate, $\mathscr{C}(r)$, as a function of radius. Error bar is one standard deviation of the average compaction rate. (a) Profiles of compaction rate for samples with a normalized compaction length of, δ_c/H =1-2. (b) Compaction rates at different compaction lengths.

4.4.6 Influences of compaction length on compaction rate

In Table 4.3, the calculated values for normalized compaction lengths, δ_c/H, settle into three groups based on melt composition: $\delta_c/H = 20$ for the olivine + Li-silicate sample, $\delta_c/H =$ 1–2 for olivine + alkali basalt samples, and $\delta_c/H =$ 0.07–0.08 for olivine + albite samples (Sample PI0895 with $\delta_c/H = 0.02$ shows no base-state melt segregation and is thus not considered in this part.). The method used in the previous subsection to average the compaction rate data for the olivine + alkali basalt samples with $\delta_c/H =$ 1–2 is used here to average the compaction rate data for the olivine + albite samples with $\delta_c/H =$ 0.07–0.08. The compaction rate for $\delta_c/H = 20$ is calculated from one sample. A comparison of compaction rates at different compaction lengths is provided in Figure 4.16(b). In the region under compaction ($r \geqslant 3$ mm), compaction rates do not differ much between different compaction lengths, although the compaction rate for $\delta_c/H = 20$ (based on a single sample) is slightly higher than that for the other two. Moreover, the compaction rate in the region under compaction, $\mathscr{C}(r) \approx 0.2\times10^{-5}$ s^{-1}, is much lower than that in the region under decompaction ($r < 3$ mm), where the decompaction rate, $-\mathscr{C}(r)$, is as large as 6×10^{-5} s^{-1}. Base on this analyses, the rate of base-state melt segregation increases as compaction length increases, that is, $|\mathscr{C}(r)|$ increases with increasing δ_c/H, consistent with the model of *Takei and Katz* (2013). The sample with the longest normalized compaction length, $\delta_c/H = 20$, exhibits the highest decompaction rate in the region under decompaction, in agreement with the prediction.

However, the decompaction rate for samples with $\delta_c/H =$ 1–2 (olivine + alkali basalt samples) is smaller than that for samples with $\delta_c/H =$ 0.07–0.08 (olivine + albite samples) at small radius ($r < 2$ mm), which is not in agreement with prediction. Several issues could cause this disagreement with prediction. First, the neglected grain size evolution with shear stress and time may be different for samples with different melt compositions. If the grain size at the outer radius of olivine + alkali basalt samples is much finer than that of olivine + albite samples, the actual compaction length of olivine + alkali basalt samples could be even lower than that of olivine + albite samples. However, high-resolution optical micrographs (in Figures 4.3, 4.4, 4.7 and 4.8) do not suggest a large difference in grain size between these samples at similar shear strains. Second,

interactions between base-state melt segregation and the formation of melt-enriched bands is not well understood. The abundance of melt-enriched bands in olivine + alkali basalt samples may effect the compaction rate for base-state melt segregation.

4.5 Conclusions

In this study, torsion experiments were preformed on samples of olivine + melts of three different compositions to vary the compaction length. A qualitative analysis of melt distribution is provided by color maps of melt distribution on transverse sections, while a quantitative analysis is obtained from radial profiles of the azimuthally averaged melt fraction. The observed increase in melt fraction along the radius from the outer edge toward the axial center occurs in most samples, a experimental demonstration of base-state melt segregation during torsional deformation.

To study the influences of compaction length on compaction rate, we made the following approximations and assumptions: (1) compaction length is a constant for each sample, independent of radius and time; (2) compaction rate for a given sample is only a function of radius, independent of time; (3) the effects of strain on the magnitude of viscous anisotropy is neglected. With these approximations and assumptions, we plotted base-state compaction rate as a function of radius for different compaction lengths to allow comparison to theoretical results.

In this comparison between experiments and model, consistences and contradictions both exist: (1) the sample with the longest compaction length exhibits the highest compaction/decompaction rate, as expected; (2) compaction rate in the region under compaction is lower than that in the region under decompaction, as expected; (3) compaction rate in the region under compaction does not change much with compaction length, contrary to model predictions; 4) the samples with the intermediate compaction length exhibit the lowest compaction/decompaction rate, while the samples with the shortest compaction length exhibit an intermediate compaction/decompaction rate, not as expected based on the theoretical model. As a contribution to a deeper understanding of Earth's dynamics and evolution, our observations will provide inspirations and constraints for theoreticians and modelers to improve two-phase flow theory with anisotropic viscosity.

Chapter 5

Conclusions

5.1 Summary of results

In this dissertation, two types of stress-driven redistribution of melt, development of pressure shadows and base-state melt segregation, were produced for the first time in partially molten rock under torsional deformation. A summary of some conclusions is presented here:

Chapter 2: Obtained from high-resolution micrographs from tangential sections of deformed partially molten samples, melt distribution around olivine beads revealed symmetrically distributed pressure shadows. Determined from crystallographic preferred orientations, the flow field of the olivine grains around the olivine bead agrees with the predictions using two-phase flow theory (*McKenzie and Holness*, 2000). These experiments are the first to produce pressure shadows in partially molten rocks.

Chapter3: Microstructural analyses of deformed samples for the distribution of melt reveal a radial gradient in melt fraction, increasing radially inward, which indicates the presence of base-state melt segregation. This agreement between theoretical prediction and experimental observation provides a validation of the hypothesis of viscous anisotropy.

Chapter 4: Based on the experimentally observed melt distribution, the influence of compaction length on compaction rate was discussed. The investigation on samples with three different

groups of compaction lengths demonstrates that (1) the sample with the largest compaction length exhibits the highest compaction/decompaction rate, and (2) the samples with the intermediate compaction length demonstrate the lowest compaction/decompaction rate, while the samples with the shortest compaction length show an intermediate compaction/decompaction rate. This observation with both agreements and disagreements with theoretical predictions will help to advance the hypothesis of viscous anisotropy.

5.2 Implications and Future directions

5.2.1 Constraining bulk viscosity

The experimental results presented in Chapter 2, if combined with refinements of the model by *McKenzie and Holness* (2000), will allow a measurement of bulk viscosity for partially molten rocks. With a well determined bulk viscosity, the compaction length can be more accurately constrained, which will advance our understanding of many compaction processes, including the formation of melt-enriched bands, in which compaction length affects the spacing between bands, and base-state melt segregation, in which compaction length controls the compaction rate. Scaling to the Earth, this constraint on compaction length could improve our knowledge of the influence of stress-driven melt segregation in the mantle.

A recent study by our collaborator *Rudge* (2014) presented a series of analytical solutions for viscous compacting flow past a rigid impermeable sphere to model the process of the development of pressure shadows described in Chapter 2. Although these analytical solutions both agree and disagree with our experimental observations, future collaboration on the measurement of bulk viscosity is promising.

5.2.2 Viscous anisotropy

Built on two-phase flow theory, viscous anisotropy takes the anisotropy in microstructure into account and calculates the effects of this microstructural anisotropy at the macro scale. Validated by

our experiments presented in Chapter 3, the theory viscous anisotropy can now be incorporated into models of compaction processes that involves the alignment of melt. From experiments presented in Chapter 4, new insights are introduced for viscous anisotropy by, (1) incorporating the evolution of grain size into the theory, (2) varying the angle of viscous anisotropy due to the rotating of MPO angle with increasing strain. The studies in Chapters 3 and 4 strength and improve the fundamentals of two-phase flow theory incorporating viscous anisotropy, upon which progress in our understanding of the evolution and dynamics of the Earth will be established.

References

Anderson, D. L., and C. Sammis (1970), Partial melting in the upper mantle, *Physics of the Earth and Planetary Interiors*, *3*, 41–50.

Bachmann, F., R. Hielscher, and H. Schaeben (2010), Texture analysis with mtex–free and open source software toolbox, *Solid State Phenomena*, *160*, 63–68.

Bear, J. (1972), *Dynamics of fluid in porous media*, American Elsevier, New York.

Bernabé, Y., U. Mok, and B. Evans (2003), Permeability-porosity relationships in rocks subjected to various evolution processes, *Pure and Applied Geophysics*, *160*(5), 937–960.

Berton, J., D. Durney, J. Wheeler, and J. Ford (2006), Diffusion-creep modelling of fibrous pressure-shadows, *Tectonophysics*, *425*(1), 191–205.

Berton, J., D. Durney, and J. Wheeler (2011), Diffusion-creep modelling of fibrous pressure shadows ii: influence of inclusion size and interface roughness, *Geological Society, London, Special Publications*, *360*(1), 319–328.

Butler, S. (2012), Numerical models of shear-induced melt band formation with anisotropic matrix viscosity, *Physics of the Earth and Planetary Interiors*, *200*, 28–36.

Butt, H.-J., K. Graf, and M. Kappl (2006), *Physics and chemistry of interfaces*, John Wiley & Sons.

Canny, J. (1986), A computational approach to edge detection, *Pattern Analysis and Machine Intelligence, IEEE Transactions on*, *PAMI-8*(6), 679–698.

Cooper, R., and D. Kohlstedt (1982), Interfacial energies in the olivine-basalt system, *Adv. Earth Planet. Sci*, *12*, 217–228.

Cooper, R. F., and D. L. Kohlstedt (1984), Solution-precipitation enhanced diffusional creep of partially molten olivine-basalt aggregates during hot-pressing, *Tectonophysics*, *107*(3-4), 207–233.

Cooper, R. F., and D. L. Kohlstedt (1986), Rheology and structure of olivine-basalt partial melts, *Journal of Geophysical Research*, *91*(B9), 9315–9323.

Dijkstra, A. H., M. R. Drury, R. L. Vissers, and J. Newman (2002), On the role of melt-rock reaction in mantle shear zone formation in the othris peridotite massif (greece), *Journal of Structural Geology*, *24*(9), 1431–1450.

Durney, D., and J. Ramsay (1973), Incremental strains measured by syntectonic crystal growths, *Gravity and tectonics*, *67*, 96.

Elliott, D. (1972), Deformation paths in structural geology, *Geological Society of America Bulletin*, *83*(9), 2621–2638.

Etchecopar, A., and J. Malavieille (1987), Computer models of pressure shadows: a method for strain measurement and shear-sense determination, *Journal of Structural Geology*, *9*(5), 667–677.

Fischer, K. M., H. A. Ford, D. L. Abt, and C. A. Rychert (2010), The lithosphere-asthenosphere boundary, *Annual Review of Earth and Planetary Sciences*, *38*, 551–575.

Fisher, D., and S. Brantley (1992), Models of quartz overgrowth and vein formation- deformation and episodic fluid flow in an ancient subduction zone, *Journal of Geophysical Research*, *97*(B13), 20,043–20,061.

Giordano, D., J. K. Russell, and D. B. Dingwell (2008), Viscosity of magmatic liquids: a model, *Earth and Planetary Science Letters*, *271*(1), 123–134.

Hansen, L., M. Zimmerman, and D. Kohlstedt (2012), The influence of microstructure on deformation of olivine in the grain-boundary sliding regime, *Journal of Geophysical Research: Solid Earth (1978–2012)*, *117*(B9).

Hirano, N., E. Takahashi, J. Yamamoto, N. Abe, S. P. Ingle, I. Kaneoka, T. Hirata, J.-I. Kimura, T. Ishii, Y. Ogawa, et al. (2006), Volcanism in response to plate flexure, *Science*, *313*(5792), 1426–1428.

Hirth, G., and D. L. Kohlstedt (1995a), Experimental constraints on the dynamics of the partially molten upper mantle: Deformation in the diffusion creep regime, *Journal of Geophysical Research*, *100*(B2), 1981–2001.

Hirth, G., and D. L. Kohlstedt (1995b), Experimental constraints on the dynamics of the partially molten upper mantle: 2. deformation in the dislocation creep regime, *Journal of Geophysical Research: Solid Earth (1978–2012)*, *100*(B8), 15,441–15,449.

Holness, M. (2006), Melt–solid dihedral angles of common minerals in natural rocks, *Journal of Petrology*, *47*(4), 791–800.

Holtzman, B., and D. Kohlstedt (2007), Stress-driven melt segregation and strain partitioning in partially molten rocks: Effects of stress and strain, *Journal of Petrology*.

Holtzman, B., N. Groebner, M. Zimmerman, S. Ginsberg, and D. Kohlstedt (2003a), Stress-driven melt segregation in partially molten rocks, *Geochemistry Geophysics Geosystems*, *4*(5), 8607.

Holtzman, B., D. Kohlstedt, M. Zimmerman, F. Heidelbach, T. Hiraga, and J. Hustoft (2003b), Melt segregation and strain partitioning: implications for seismic anisotropy and mantle flow, *Science*, *301*(5637), 1227.

Holtzman, B. K., and J.-M. Kendall (2010), Organized melt, seismic anisotropy, and plate boundary lubrication, *Geochemistry, Geophysics, Geosystems*, *11*(12), doi:10.1029/2010GC003296.

Kaczmarek, M.-A., and O. Müntener (2008), Juxtaposition of melt impregnation and high-temperature shear zones in the upper mantle; field and petrological constraints from the lanzo peridotite (northern italy), *Journal of Petrology*, *49*(12), 2187–2220.

Katz, R. F., and Y. Takei (2013), Consequences of viscous anisotropy in a deforming, two-phase aggregate. part 2. numerical solutions of the full equations, *J. Fluid Mech*, *734*, 456–485.

Katz, R. F., M. Spiegelman, and B. Holtzman (2006), The dynamics of melt and shear localization in partially molten aggregates, *Nature*, *442*(7103), 676–679.

Kawakatsu, H., P. Kumar, Y. Takei, M. Shinohara, T. Kanazawa, E. Araki, and K. Suyehiro (2009), Seismic evidence for sharp lithosphere-asthenosphere boundaries of oceanic plates, *Science*, *324*(5926), 499.

Kelemen, P., N. Shimizu, and V. Salters (1995), Extraction of mid-ocean-ridge basalt from the upwelling mantle by focused flow of melt in dunite channels, *Nature*, *375*, 747–753.

Kelemen, P., G. Hirth, N. Shimizu, M. Spiegelman, and H. Dick (1997), A review of melt migration processes in the adiabatically upwelling mantle beneath oceanic spreading ridges, *Philosophical Transactions of the Royal Society of London. Series A: Mathematical, Physical and Engineering Sciences*, *355*(1723), 283–318.

Kendall, J.-M. (1994), Teleseismic arrivals at a mid-ocean ridge: Effects of mantle melt and anisotropy, *Geophysical Research Letters*, *21*(4), 301–304.

King, D., M. Zimmerman, and D. Kohlstedt (2010), Stress-driven melt segregation in partially molten olivine-rich rocks deformed in torsion, *Journal of Petrology*, *51*(1-2), 21.

Kohlstedt, D., and B. Holtzman (2009), Shearing melt out of the earth: An experimentalist's perspective on the influence of deformation on melt extraction, *Annual Review of Earth and Planetary Sciences*, *37*(1), 561.

Kohlstedt, D., H. Keppler, and D. Rubie (1996), Solubility of water in the α, β and γ phases of (Mg, Fe) 2 SiO 4, *Contributions to Mineralogy and Petrology*, *123*(4), 345–357.

Kohlstedt, D., M. Zimmerman, and S. Mackwell (2010), Stress-driven melt segregation in partially molten feldspathic rocks, *Journal of Petrology*, *51*(1-2), 9–19.

Le Roux, V., A. Tommasi, and A. Vauchez (2008), Feedback between melt percolation and deformation in an exhumed lithosphere–asthenosphere boundary, *Earth and Planetary Science Letters*, *274*(3), 401–413.

Lim, J. (1990), Two-dimensional signal and image processing, *Englewood Cliffs, NJ, Prentice Hall, 1990, 710 p.*, *1*.

Masuda, T., and N. Mizuno (1995), Deflection of pure shear viscous flow around a rigid spherical body, *Journal of Structural Geology*, *17*(11), 1615–1620.

McKenzie, D. (1984), The generation and compaction of partially molten rock, *Journal of Petrology*, *25*(3), 713.

McKenzie, D., and M. Holness (2000), Local deformation in compacting flows: Development of pressure shadows, *Earth and Planetary Science Letters*, *180*(1-2), 169–184.

Mei, S., W. Bai, T. Hiraga, and D. Kohlstedt (2002), Influence of melt on the creep behavior of olivine–basalt aggregates under hydrous conditions, *Earth and Planetary Science Letters*, *201*(3), 491–507.

Mierdel, K., H. Keppler, J. R. Smyth, and F. Langenhorst (2007), Water solubility in aluminous orthopyroxene and the origin of earth's asthenosphere, *Science*, *315*(5810), 364–368.

Morgan, J. P. (1987), Melt migration beneath mid-ocean spreading centers, *Geophysical Research Letters*, *14*(12), 1238–1241.

Morgan, Z., and Y. Liang (2003), An experimental and numerical study of the kinetics of harzburgite reactive dissolution with applications to dunite dike formation, *Earth and Planetary Science Letters*, *214*(1), 59–74.

Parker, J. (2010), *Algorithms for image processing and computer vision*, Wiley Publishing.

Paterson, M., and D. Olgaard (2000), Rock deformation tests to large shear strains in torsion, *Journal of Structural Geology*, *22*(9), 1341–1358.

Qi, C., Y.-H. Zhao, and D. L. Kohlstedt (2013), An experimental study of pressure shadows in partially molten rocks, *Earth and Planetary Science Letters*, *382*, 77–84.

Raj, R. (1981), Morphology and stability of the glass phase in glass ceramic systems, *Journal of the American Ceramic Society*, *64*(5), 245–248.

Ramsay, J., and M. Huber (1983), *The techniques of modern structural geology*, vol. 1, Academic press.

Renner, J., K. Viskupic, G. Hirth, and B. Evans (2003), Melt extraction from partially molten peridotites, *Geochemistry Geophysics Geosystems*, *4*(5), 8606.

Rudge, J. F. (2014), Analytical solutions of compacting flow past a sphere, *Journal of Fluid Mechanics*, *746*, 466–497.

Shaw, H. (1972), Viscosities of magmatic silicate liquids; an empirical method of prediction, *American Journal of Science*, *272*(9), 870–893.

Simpson, G., M. Spiegelman, and M. I. Weinstein (2010), A multiscale model of partial melts: 1. effective equations, *Journal of Geophysical Research: Solid Earth (1978–2012)*, *115*(B4).

Spencer, S. (1991), The use of syntectonic fibres to determine strain estimates and deformation paths: an appraisal, *Tectonophysics*, *194*(1), 13–34.

Spiegelman, M. (2003), Linear analysis of melt band formation by simple shear, *Geochemistry, Geophysics, Geosystems*, *4*(9).

Stern, R. (2002), Subduction zones, *Reviews of Geophysics*, *40*(4), 1012.

Stevenson, D. (1989), Spontaneous small-scale melt segregation in partial melts undergoing deformation, *Geophysical Research Letters*, *16*(9), 1067–1070.

Takei, Y. (2010), Stress-induced anisotropy of partially molten rock analogue deformed under quasi-static loading test, *Journal of Geophysical Research: Solid Earth (1978–2012)*, *115*(B3).

Takei, Y., and B. Holtzman (2009a), Viscous constitutive relations of solid-liquid composites in terms of grain boundary contiguity: 1. Grain boundary diffusion control model, *Journal of Geophysical Research*, *114*(B6), B06,205.

Takei, Y., and B. Holtzman (2009b), Viscous constitutive relations of solid-liquid composites in terms of grain boundary contiguity: 3. Causes and consequences of viscous anisotropy, *Journal of Geophysical Research*, *114*(B6), B06,207.

Takei, Y., and B. Holtzman (2009c), Viscous constitutive relations of solid-liquid composites in terms of grain boundary contiguity: 2. Compositional model for small melt fractions, *Journal of Geophysical Research*, *114*(B6), B06,206.

Takei, Y., and R. F. Katz (2013), Consequences of viscous anisotropy in a deforming, two-phase aggregate. part 1. governing equations and linearized analysis, *J. Fluid Mech*, *734*, 424–455.

Vernon, R. (2004), *A practical guide to rock microstructure*, Cambridge University Press.

von Bargen, N., and H. Waff (1986), Permeabilities, interfacial areas and curvatures of partially molten systems: results of numerical computations of equilibrium microstructures, *Journal of Geophysical Research*, *91*(B9), 9261–9276.

Waff, H., and J. Bulau (1979), Equilibrium fluid distribution in an ultramafic partial melt under hydrostatic stress conditions, *Journal of Geophysical Research: Solid Earth (1978–2012)*, *84*(B11), 6109–6114.

Wark, D. A., and E. B. Watson (2000), Effect of grain size on the distribution and transport of deep-seated fluids and melts, *Geophysical Research Letters*, *27*(14), 2029–2032.

Zimmerman, M. E., S. Zhang, D. L. Kohlstedt, and S.-i. Karato (1999), Melt distribution in mantle rocks deformed in shear, *Geophysical Research Letters*, *26*(10), 1505–1508.

Appendix A

Image processing techniques

In this chapter, the image processing techniques used in Chapter 4 are presented. The procedure of processing the high-resolution micrographs into binary images, the method on stitching the processed binary back into a mosaic image, and the technique to generate a radial profile on the distribution of melt are introduced in the following sections. The softwares used in image processing are MATLAB, Microsoft Excel, Adobe Photoshop and (Fiji Is Just) ImageJ. The processes in MATLAB are exhibited in the form of MATLAB codes.

A.1 Making binary images

In this section, the processing of micrographs from sample PI0891 is used as a tutorial. The MATLAB m-files introduced in the following are placed in a folder containing two folders: "TIF" and "BW", as illustrated in Figure A.1. Folder "TIF" holds the original micrographs as .tif files obtained from our optical microscope. Folder "BW" holds the processed binary images, and is empty before running the code. The name of the micrographs is "0891 transverse 1 HD_p*iiii*.TIF", where *iiii* is a number from 0001 to 2209.

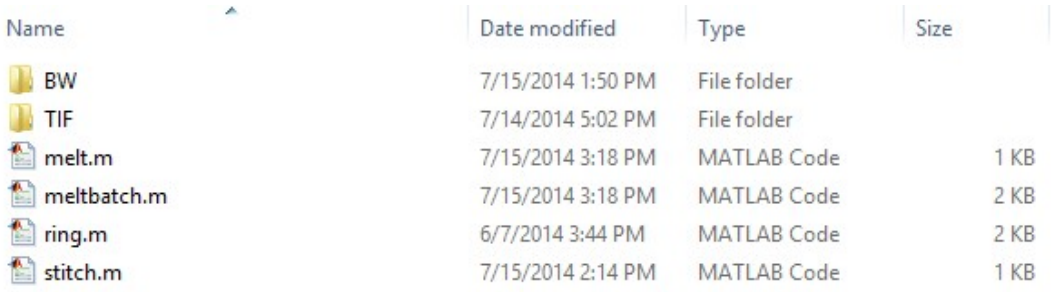

Figure A.1: Screenshot before the image processing.

meltbatch.m

```
clear all; close all;
% Define folders of the images.
directory1 = 'C:\Research\Experiments\2014 HP+Tor 31-1 PI-0891\0891
transverse 1 HD\TIF\';
directory2 = 'C:\Research\Experiments\2014 HP+Tor 31-1 PI-0891\0891
transverse 1 HD\BW\';
% m is the variable in the file name varying from 1 to the total number
% of .tif files, that is, 2304 for sample PI0891.
for m=1:9
        X=[directory1 '0891 transverse 1 HD_p000' num2str(m) '.tif'];
        Y=[directory2 '0891 transverse BW ' num2str(m) '.tif'];
        % Read the original micrographs.
        [I,map]=imread(X);
        info=imfinfo(X);
        % The default color space for micrographs is not indexed.
        It is  changed to grayscale.
        if strcmp(info.ColorType,'indexed')==1
            Igray=ind2gray(I,map);
            imwrite(Igray,X);
        end
        % Call to the function melt(X), which is elaborated in the
        % following. BW is the generated binary image.
        [BW,ave(m)]=melt(X);
        % Write BW into a file in folder "BW".
        imwrite(BW,Y);
end
```

```
% Repeat the process for different m.
for m=10:99
        X=[directory1 '0891 transverse 1 HD_p00' num2str(m) '.tif'];
        Y=[directory2 '0891 transverse BW ' num2str(m) '.tif'];
        [I,map]=imread(X);
        info=imfinfo(X);
        if strcmp(info.ColorType,'indexed')==1
            Igray=ind2gray(I,map);
            imwrite(Igray,X);
        end
        [BW,ave(m)]=melt(X);
        imwrite(BW,Y);
end

for m=100:999
        X=[directory1 '0891 transverse 1 HD_p0' num2str(m) '.tif'];
        Y=[directory2 '0891 transverse BW ' num2str(m) '.tif'];
        [I,map]=imread(X);
        info=imfinfo(X);
        if strcmp(info.ColorType,'indexed')==1
            Igray=ind2gray(I,map);
            imwrite(Igray,X);
        end
        [BW,ave(m)]=melt(X);
        imwrite(BW,Y);
end
```

```
for m=1000:2209
        X=[directory1 '0891 transverse 1 HD_p' num2str(m) '.tif'];
        Y=[directory2 '0891 transverse BW ' num2str(m) '.tif'];
        [I,map]=imread(X);
        info=imfinfo(X);
        if strcmp(info.ColorType,'indexed')==1
             Igray=ind2gray(I,map);
             imwrite(Igray,X);
        end
        [BW,ave(m)]=melt(X);
        imwrite(BW,Y);
end
```

melt.m

```
function [BW,ave]= melt(X)
% X is input, the name of the file.
% BW is output matrix, which is the binary image.
% ave is the average melt fraction in this image.
%%%%%%%%%%%%%%%%%%%%%%%%%%%%%%%%%%%%%%%%%%%%%%%%%%%%%%%%%%%%%%%%%%%%%%%
% Read image X in to a matrix I.
I=imread(X);
% Remove cracks, so that their dark color won't affect the
% adjustment of contrast. The grayscale for cracks varies with
% samples. So this number "50" is only valid for sample PI0891,
% and needs to be checked for each sample before running the code.
for i = 1:1000
    for j = 1:1000
        if I(i,j) <= 50
            I(i,j) = 50;
        end
    end
end
% Automatically adjust the contrast of the original image.
I=imadjust(I);

%%%%%%%%%%%%%%%%%%%%%%%%%%%%%%%%%%%%%%%%%%%%%%%%%%%%%%%%%%%%%%%%%%%%%%%
% Make a binary image BW1 using edge detection method.
% Detect edges.
[junk threshold] = edge(I,'sobel');
fudgeFactor=0.6;
```

```
BWs = edge(I,'sobel',threshold * fudgeFactor);
%Dilate edges so they connect.
se90 = strel('line',2,90);
se0  = strel('line',2,0);
BWsdil = imdilate(BWs, [se90 se0]);
%Fill melt pockets.
BWdfill = imfill(BWsdil, 'holes');
%Smooth and clean.
seD = strel('diamond',1);
BW1 = imerode(BWdfill,seD);
BW1 = imerode(BW1,seD);

%%%%%%%%%%%%%%%%%%%%%%%%%%%%%%%%%%%%%%%%%%%%%%%%%%%%%%%%%%%%%%%%%%%%%%%
% Make another binary image BW2 using a threshold of grayscale.
BW2=im2bw(I,0.4);
BW2=1-BW2;

%%%%%%%%%%%%%%%%%%%%%%%%%%%%%%%%%%%%%%%%%%%%%%%%%%%%%%%%%%%%%%%%%%%%%%%
% Run a logical conjunction for BW1 and BW2.
BW = BW1.*BW2;
ave = sum(sum(BW));
```

An example of the original micrograph and processed binary image is illustrated in Figure A.2. Melt is precisely distinguished from olivine. The shape of melt pockets is also well preserved.

A.2 Stitching into a mosaic image

After running **meltbatch.m**, folder "BW" now contains the processed binary images, which are then stitched together into a black&white, mosaic image. These binary images have no obvious features for Adobe Photoshop to perform an automated stitching. In order to make the mosaic image, the original micrographs are stitched using (Fiji Is Just) ImageJ. The "grid/collection stitching" tool in menu "Plugins/Stitching" provides an accurate stitching of the micrographs and exports a file named "TileConfiguration.registered.txt", which contains the corrected position information for every micrograph. Import this file using MATLAB, with semicolon and comma as the delimiters, which results in three 2209×1 matrices: names of files, X-coordinates, and Y-coordinates. Note that the names are of the original micrographs and not in the order of 1 to 2209. Therefore, the matrices are copied into Excel to be sorted by A-Z order, as in Figure A.3. Save this Excel file as "corr.xlsx", and import its data into MATLAB, with column B named as "X" and column named as "Y". Run MATLAB code **stitch.m** to stich the binary images into the mosaic image.

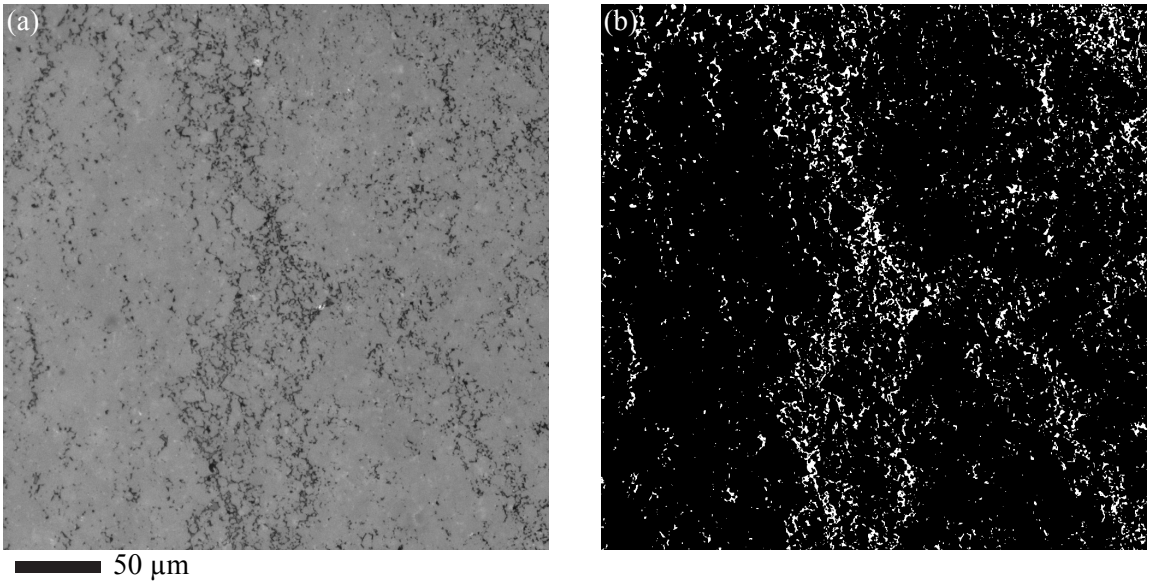

Figure A.2: A comparison between an original micrograph and a binary image after processing.(a) Original micrograph. 0891 transverse HD p_0255.tif. (b) Binary image. 0891 transverse BW 255.tif

	A	B	C	D
1	'0891 transverse 1 HD_p0001.tif'	0	0	
2	'0891 transverse 1 HD_p0002.tif'	-6726.7725	-7525.4814	
3	'0891 transverse 1 HD_p0003.tif'	-8873.233	-10471.85	
4	'0891 transverse 1 HD_p0004.tif'	-8539.939	-10939.165	
5	'0891 transverse 1 HD_p0005.tif'	-7739.713	-10939.181	
6	'0891 transverse 1 HD_p0006.tif'	-6939.615	-10939.188	
7	'0891 transverse 1 HD_p0007.tif'	-6139.537	-10939.195	
8	'0891 transverse 1 HD_p0008.tif'	-5339.463	-10939.202	
9	'0891 transverse 1 HD_p0009.tif'	-4539.386	-10939.21	
10	'0891 transverse 1 HD_p0010.tif'	-3739.304	-10939.219	
11	'0891 transverse 1 HD_p0011.tif'	-2939.214	-10939.23	
12	'0891 transverse 1 HD_p0012.tif'	-2139.1133	-10939.244	
13	'0891 transverse 1 HD_p0013.tif'	-1339.0143	-10939.258	
14	'0891 transverse 1 HD_p0014.tif'	-538.9303	-10939.27	
15	'0891 transverse 1 HD_p0015.tif'	261.1153	-10939.276	
16	'0891 transverse 1 HD_p0016.tif'	1061.1333	-10939.278	
17	'0891 transverse 1 HD_p0017.tif'	1861.1335	-10939.278	
18	'0891 transverse 1 HD_p0018.tif'	2661.1338	-10939.277	
19	'0891 transverse 1 HD_p0019.tif'	3461.1338	-10939.277	
20	'0891 transverse 1 HD_p0020.tif'	4245.691	-10888.909	
21	'0891 transverse 1 HD_p0021.tif'	5038.3545	-10876.3	
22	'0891 transverse 1 HD_p0022.tif'	5837.784	-10873.9	
23	'0891 transverse 1 HD_p0023.tif'	6638.373	-10876.502	

Figure A.3: Screenshot for the sorted position information for every micrographs. Column B is X-coordinates. Column C is Y-coordinates.

stitch.m

```
directory = 'C:\Research\Experiments\2014 HP+Tor 31-1 PI-0891\
0891 transverse 1 HD\BW\';
% X and Y are preloaded matrices.
X=round(X);
Y=round(Y);
S=zeros(40000,40000,'uint8');
for m=1:2209
    name=[directory '0891 transverse BW ' num2str(m) '.tif'];
    I = imread(name);
    my = 11000+Y(m,1);
    mx = 11000+X(m,1);
    if mx > 0 && my > 0
        S(my:my+999,mx:mx+999) = I;
    end
end
imwrite(S,'0891 transverse HD BW.tif');
```

A.3 Calculation of the radial profile of melt distribution

With a black&white, mosaic image created to cover the whole transverse section of sample PI0891, the radial distribution of melt can be calculated. Before starting the calculation, the mosaic image needs to be examined first. As illustrate in Figure A.4, the outer edge of the section is not well segmented, since the micrographs close to the outer is usually out of focus. These regions close to the outer radius needs to be excluded from our calculation. Furthermore, the cracks has to be erased by hand in Adobe Photoshop. Then the mosaic image is edited that medium gray color marks the regions that should not incorporate with the calculation, as illustrated in Figure A.5. This image is saved as "0891 transverse HD work.tif". Finally, run MATLAB code **ring.m** to calculate the radial profile of melt distribution. The results are illustrated in Figure **??**

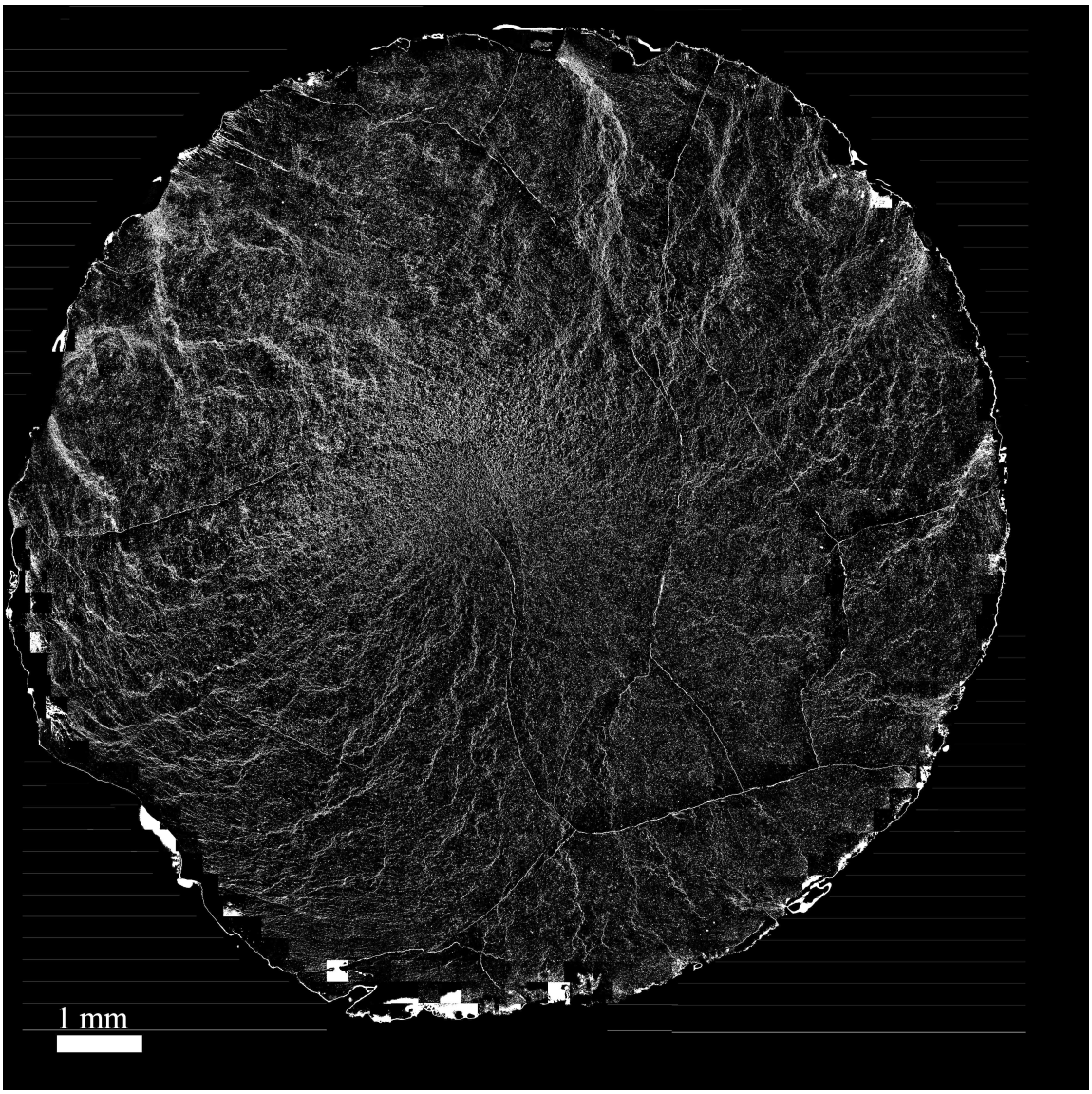

Figure A.4: Stitched black&white, mosaic image for sample PI0891.

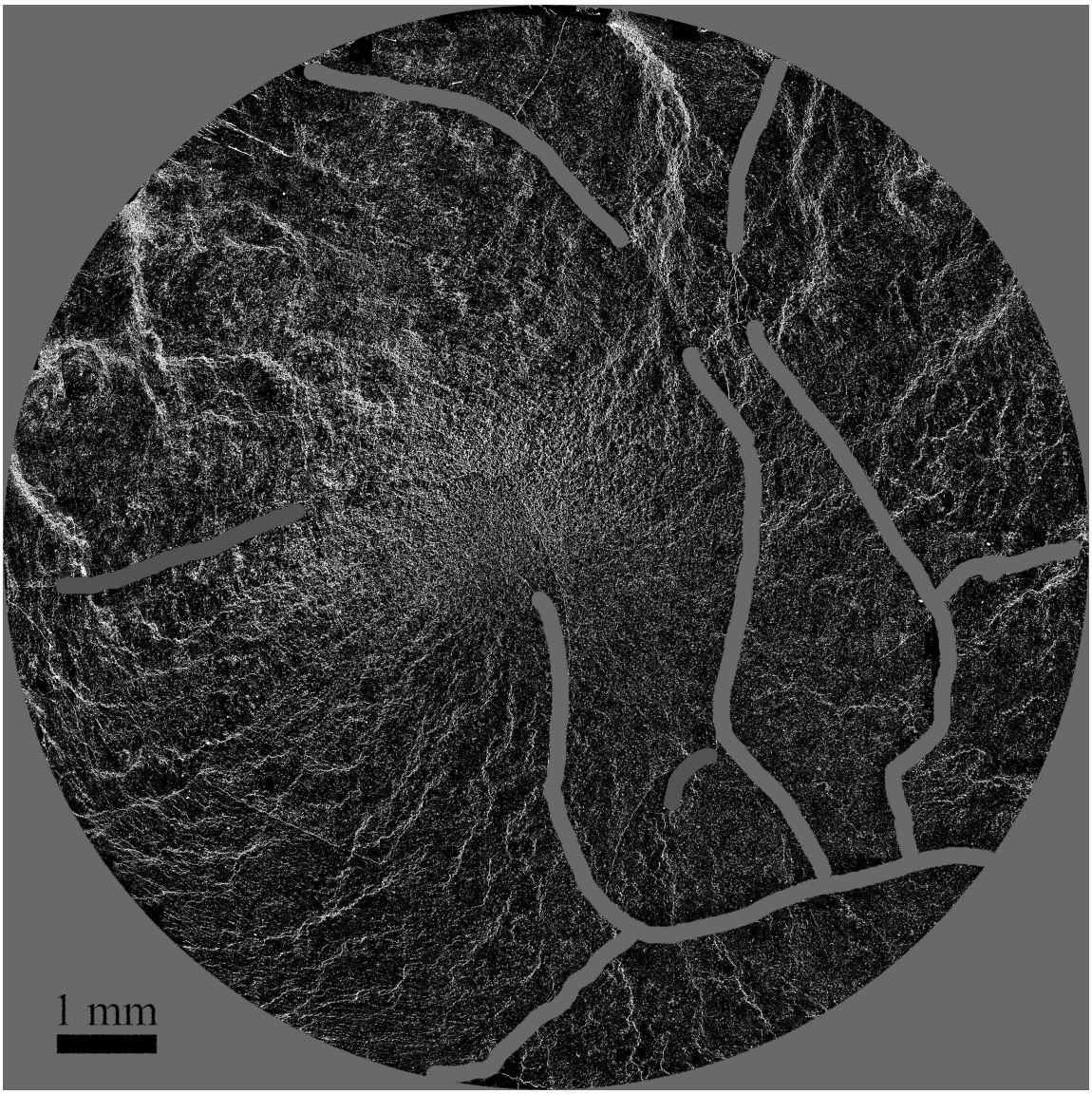

Figure A.5: Edited image ready for processing.

ring.m

```
function frac= ring(X,a)
% X is input, the name of the file.
% a is the thickness of the rings, in pixels (77 pixels = 0.1 mm).
%%%%%%%%%%%%%%%%%%%%%%%%%%%%%%%%%%%%%%%%%%%%%%%%%%%%%%%%%%%%%%%%
I=imread([X ' work.tif']);
s=size(I);
center=fix(0.5*s);
% I2 is used to memorize the position of the medium gray regions.
I2=zeros(s,'uint8');
for i=1:s(1)
    for j=1:s(2)
        if I(i,j)==105   % 105 is the medium gray represents cracks
            I2(i,j)=1;
        end
    end
end
allmelt = 0;
whole = 0 ;

% Make binary again, so that the gray is now black.
BW=im2bw(I,0.5);

% m is the number of rings.
m=fix(max(center)/a);
% Set the initial conditions for each ring.
frac(m).area=0;
```

```
frac(m).melt=0;
frac(m).distance=round(a*0.32)*(m-0.5)/1000;
for i=1:m-1
    frac(i).area=0;
    frac(i).melt=0;
    frac(i).distance=round(a*0.32)*(i-0.5)/1000;
end

% For each pixel, its distance to the axial center is calculated,
% which tells the specific ring, to which this pixel is assigned.
for i=1:s(1)
    for j=1:s(2)
        if I2(i,j) ~=1
            dist=sqrt((i-center(1)).^2+(j-center(2)).^2);
            n=fix(dist/a)+1;
            if n <= m
                frac(n).area=frac(n).area+1;
                frac(n).melt=frac(n).melt+BW(i,j);
            end
        end
    end
end

% With all pixels assigned to specific rings, the melt fraction in
% each ring can be calculated from the number of white pixels divided
% by the total number of pixels.
for i=1:m
```

```
    y(i)=frac(i).melt/frac(i).area;
    x(i)=frac(i).distance;
    allmelt = allmelt + frac(i).melt;
    whole = whole + frac(i).area;
end
ave = allmelt/whole;
yn = y./ave;

% Plot the profile
plot (x,y,'o');
xlabel('distance from center (mm)','FontName','Times New Roman');
ylabel('melt fraction','FontName','Times New Roman');
ylim([0.00 0.15]);
set(gca,'FontName','Times New Roman','FontSize',20);
% Save the result.
save([X ' ring ' int2str(round(a*0.32)) '.mat']) ;
```

Appendix B

Viscosity tensor with viscous anisotropy

This appendix is contributed by Yasuko Takei, as a supplementary material for Chapter 3.

The diffusion-creep viscosity tensor C_{ijkl} of a partially molten rock can be calculated by using a microstructure-based model (*Takei and Holtzman*, 2009a). The grain coordinates (x_g, y_g, z_g) are defined independently of the continuum coordinates (x, y, z). Each grain in the aggregate is assumed to have 14 circular contacts with equal radius. Microstructural anisotropy is represented by a decrease (or increase) in the radius of the two contact faces in the x_g (or y_g) direction. By substituting this contact geometry into equation (42) of *Takei and Holtzman* (2009a), C_{ijkl} $(i, j, k, l = x_g, y_g, z_g)$ is calculated as

$$C_{ijkl} = \zeta\,\delta_{ij}\delta_{kl} + \eta\left(\delta_{ik}\delta_{jl} + \delta_{il}\delta_{jk} - \frac{2}{3}\delta_{ij}\delta_{kl}\right) - \Delta\,\delta_{ix_g}\delta_{jx_g}\delta_{kx_g}\delta_{lx_g} + \Delta'\,\delta_{iy_g}\delta_{jy_g}\delta_{ky_g}\delta_{ly_g}, \tag{B.1}$$

where η and ζ correspond to the shear and bulk viscosity of an isotropic matrix, and Δ (or Δ') represents the decrease (or increase) in viscosity in the x_g (or y_g) direction.

For simplicity, we consider a two dimensional problem, in which the σ_1–σ_3 plane is parallel to the xy–plane. Let Θ be the angle between the x_g and x axes. Then, by a coordinate transformation of expression (B.1) (e.g., *Takei and Katz*, 2013), viscosity tensor in the continuum coordinates, C_{ijkl} $(i, j, k, l = x, y, z)$, is obtained as

$$C_{ijkl} = \eta_0 \mathrm{e}^{-\lambda(\phi-\phi_0)} \times$$

$$\begin{array}{c|cccccc}
ij\downarrow & kl\to xx & yy & zz & yz & zx & xy \\
xx & r_\zeta + \frac{4}{3} - \frac{\alpha+\beta}{2}\cos 2\Theta & r_\zeta - \frac{2}{3} & r_\zeta - \frac{2}{3} & 0 & 0 & -\frac{\alpha+\beta}{4}\sin 2\Theta \\
 & -\frac{\alpha-\beta}{8}(3+\cos 4\Theta) & -\frac{\alpha-\beta}{8}(1-\cos 4\Theta) & & & & -\frac{\alpha-\beta}{8}\sin 4\Theta \\
yy & \cdot & r_\zeta + \frac{4}{3} + \frac{\alpha+\beta}{2}\cos 2\Theta & r_\zeta - \frac{2}{3} & 0 & 0 & -\frac{\alpha+\beta}{4}\sin 2\Theta \\
 & & -\frac{\alpha-\beta}{8}(3+\cos 4\Theta) & & & & +\frac{\alpha-\beta}{8}\sin 4\Theta \\
zz & \cdot & \cdot & r_\zeta + \frac{4}{3} & 0 & 0 & 0 \\
yz & \cdot & \cdot & \cdot & 1 & 0 & 0 \\
zx & \cdot & \cdot & \cdot & \cdot & 1 & 0 \\
xy & \cdot & \cdot & \cdot & \cdot & \cdot & 1 - \frac{\alpha-\beta}{8}(1-\cos 4\Theta)
\end{array} \tag{B.2}$$

where only 21 of the 81 components are shown due to the symmetry of C_{ijkl}. The factor in front of the matrix represents the shear viscosity η, which decreases exponentially with increasing melt fraction ϕ: η_0 represents η at reference melt fraction ϕ_0 and λ is called porosity weakening factor. Parameter $r_\zeta = \zeta/\eta$ represents the bulk to shear viscosity ratio. Parameters $\alpha = \Delta/\eta$ and $\beta = \Delta'/\eta$ represent the magnitude of viscous anisotropy in the reduced and increased directions, respectively. The parameters r_ζ, α, and β are assumed to be independent of melt fraction based on the theoretical result (*Takei and Holtzman*, 2009a; *Takei and Katz*, 2013)

When $\Delta' = 0$ and $\beta = 0$, (B.1) and (B.2) are equal to those used in the previous study (*Takei and Katz*, 2013; *Katz and Takei*, 2013). The present formulation is more general than the previous one in that the effect of contiguity change in the σ_1 direction can be taken into account. In the modeling, Θ is usually taken such that the x_g axis is in the σ_3 direction. However, because Θ is defined by the direction of microstructural anisotropy independently of the resultant stress, it can be used to describe general MPO direction (Figure 3.2).